2017

Mechanical Characterization and Non-Destructive Evaluation of SiCF-SiCM Composite Tubing with the Impulse Excitation Technique

Nathaniel Truesdale
University of South Carolina

Mechanical Characterization and Non-Destructive Evaluation of SiC_F-SiC_M Composite Tubing with the Impulse Excitation Technique

by

Nathaniel Truesdale

Bachelor of Science
University of South Carolina, 2015

Submitted in Partial Fulfillment of the Requirements

For the Degree of Master of Science in

Nuclear Engineering

College of Engineering and Computing

University of South Carolina

2017

Accepted by:

Xinyu Huang, Director of Thesis

Jing Jing Bao, Reader

Cheryl L. Addy, Vice Provost and Dean of the Graduate School

DEDICATION

This work is dedicated to the men and women in the Engineering community that have devoted their lives to the advancement of modern society. To be a part of the Engineering field is to a part in shaping the future. It is both a responsibility and a privilege to ensure the longevity of the human race and to pursue all knowledge of the natural world. This is also dedicated to all the previous members of the scientific community that have in every way influenced my choice to pursue an education in Engineering.

ACKNOWLEDGEMENTS

I would like to acknowledge and express my deepest appreciation to Dr. Xinyu Huang and my coworkers in the lab, who all provided me ample opportunity and support to perform research throughout my Graduate education. In addition, I would like to acknowledge Dr. George Jacobsen and Kirill Shapovalov of General Atomics for providing research material and well needed feedback throughout this work.

This work was performed at the University of South Carolina, Mechanical Engineering Department, in collaboration with General Atomics. Funding was provided by the Department of Energy Office of Nuclear Energy under the Accident Tolerant Fuel Program, DE-NE0000566 and DE-NE0008222. This report was prepared as an account of work partially sponsored by an agency of the United States Government. Neither the United States Government nor any agency thereof nor any of their employees make any warranty, express or implied, or assumes any legal liability or responsibility for the accuracy, completeness, or usefulness of any information, apparatus, product, or process disclosed, or represents that its use would not infringe privately owned rights. Reference herein to any specific commercial product, process, or service by trade name, trade mark, manufacturer, or otherwise does not constitute or imply its endorsement, recommendation, or favoring by the United States Government or any agency thereof. The views and opinions of the authors expressed herein do not necessarily state or reflect those of the United States Government or any agency thereof.

ABSTRACT

With growing interest on ceramic fiber reinforced ceramic matrix composites (CMC) for accident tolerant fuel, the need for mechanical characterization of ceramic composite arises. It has been of particular interest to non-destructively evaluate the mechanical performance of these composites. Impulse excitation (IE) is a well-established method for non-destructive mechanical characterization of homogeneous isotropic material of well-defined shapes. In this thesis, impulse excitation technique was applied for non-destructive characterization of composite tube for the first time as far as we know. CMC, when stressed beyond its damage threshold, will experience various forms of structural damage, such as matrix micro-cracking, fiber-matrix debonding, and fiber breakage. The effects of damage on its vibrational frequency and damping were studied using the impulse excitation technique.

Nuclear fuel cladding can experience both tensile and compressive stress, however, most mechanical testing is conducted by putting it under tensile stress: the examples are uniaxial tensile test and internal pressure burst test. Little experimentation involving compression of CMC tubing via external pressure has been performed previously. In this thesis, the mechanical behavior of CMC under compressive stress up to the point of material failure was studied using an adapted rubber plug compression technique and with strain gauge installed on the internal surface of the composite tube.

The experimentation performed in this thesis focuses on: 1) the utilization of impulse excitation as a non-destructive evaluation method to determine mechanical properties and to monitor the damage of silicon carbide fiber reinforced silicon carbide matrix (SiC_f-SiC_m) composite tubing, and 2) the mechanical characterization of SiC_f-SiC_m composite tubing under external pressure. In the first focus, novel configuration for enabling the impulse excitation measurement of slender tube was developed. The method was first validated on tubes of well-characterized materials under free-free and clamped-free configurations. Validation testing of all IE setups resulted in less than 6% deviation of mechanical properties when compared to published values. Afterwards, IE was performed on undamaged SiC_f-SiC_m composite tubular samples to obtain axial elastic modulus and shear modulus. The measured properties fell within 4.1% of the same properties obtained from conventional tension and torsion tests. The IE techniques were found to be relatively simple, quick, and highly accurate for obtaining elastic properties of composite tubes.

In addition, the effectiveness of IE method for detecting damage in CMC tube was studied experimentally. Progressive damage in the ceramic composite tube were gradually induced by subjecting it to internal pressurization cycles. Incremental pressure was applied in these loading cycles to levels over the proportional limit stress (PLS) of the CMC. The occurrence of damage was confirmed by acoustic emission monitoring. IE was performed after each pressurization cycle to detect the changes to its vibrational response under fixed-free boundary conditions. It was noted the presence of micro-cracking and other form of composite damage decrease natural frequency while increasing its vibrational damping. The study indicates that both the natural frequency and the internal damping are very

sensitive and change monotonically with material damage. As such they can serve as effective damage indicators for CMC.

The second focus was to study the mechanical response of the composite tube under compressive stress. The experiment involved compressing the outer surface of a CMC tube while measuring hoop strain on the internal surface. The compression test is to simulate the pressurized coolant acting on nuclear fuel during typical Light Water Reactor (LWR) operation. A novel external expanding plug method for applying external pressure to the sample tube was developed and validated on known material. SiC_f-SiC_m composite tubing was then tested to failure and mechanical compressive stress-strain responses were observed. It was found compressive behavior of CMC was significantly different than the tensile behavior. There is a lack of pronounced "bending" as shown in typical tensile stress-strain curve of CMC. In the course of the study, delicate techniques were developed to install small foil strain gauge on the internal curved surface of small bore tubing. It was found that both curvature and internal pressure affect the strain reading from gauge installed on curved internal surfaces.

TABLE OF CONTENTS

LIST OF TABLES

LIST OF FIGURES

LIST OF ABBREVIATIONS

AE ..... Acoustic Emission

CFRP ..... Carbon Fiber Reinforced Plastics

CMC ..... Ceramic Matrix Composite

CVD ..... Chemical Vapor Deposited

CVI ..... Chemical Vapor Infiltration

DIC ..... Digital Image Correlation

ER ..... Electrical Resistance

FFT ..... Fast Fourier Transformation

HDT ..... Hit Definition Time

HLT ..... Hit Lockout Time

HP ..... Hot Pressing

ID ..... Inner Diameter

IET ..... Impulse Excitation Technique

LSI ..... Liquid Silicon Infiltration

LOCA.....Loss of Coolant Accident

NITE .....Nano-Infiltration Transient Eutectic

NDT .....Nondestructive Testing

OD.....Outer Diameter

PDT .....Peak Definition Time

PIP..... Polymer Impregnation/ Pyrolysis

PLS.....Proportional Limit Stress

R&D.....Research and Development

RFDA..... Resonant Frequency and Damping Analyzer

SiC.....Silicon Carbide

UTS .....Ultimate Tensile Stress/Strength

UT .....Ultrasonic Testing

CHAPTER 1: INTRODUCTION

1.1 Silicon Carbide Composite Cladding

Silicon Carbide fiber reinforced Silicon Carbide matrix (SiC_f-SiC_m) composite is a ceramic matrix composite (CMC) that is being considered as an innovative material for accident tolerant nuclear fuel cladding in the nuclear industry. SiC_f-SiC_m composites offer exemplary mechanical and chemical properties such as high temperature stability, irradiation tolerance, oxidation resistance, and potentially improved toughness compared to metals. [1,2] Various composite architectures are being studied by research and development (R&D) groups in the nuclear field. Combinations of the following configurations are under development and study: monolithic composite layers, Triplex layers of SiC_f-SiC_m composites, and bi/ tri-axial braiding of SiC_f-SiC_m composites. [3] As a result, great variation in the CMC structure can be obtained with vast differences to material strength and properties which in a nuclear application can be fabricated to surpass the current zirconium alloy cladding typically used in modern light water reactors. [3]

SiC_f-SiC_m composites comprise of three key components. The first are the Silicon carbide fibers that are bundled together to form structural fiber tows for the material. The ceramic fibers can set into complex architectures based on the application of the composite such as woven 2-dimensional fabrics or multidimensional fiber preforms. The fibers provide majority of the composites strength and toughness in the composite and vary based

on the direction of the applied stresses to the material. The earliest sets of SiC fibers included cg-Nicalon and Hi-Nicalon, whose Elastic Modulus in the fiber axial direction ranged between 170 to 270 GPa. [4] Although the braided cladding composed of these fibers held satisfactory mechanical advantages compared to alloy cladding, the percent content of oxygen and carbon in the fibers yielded unwanted crystallization. This then led to densification of the CMC structure when exposed to moderate levels of neutron irradiation. Eventual development of hi-Nicalon type S SiC fibers resulted in a more suitable fiber with greater toughness and irradiation tolerance. An interphase material is then applied to the ceramic fibers through chemical vapor infiltration (CVI) process. The function of interphase coating is to adequately deflect matrix micro-cracking from the structural fibers as composite damage occurs. The ideal interphase coating material should have a low shear strength to effectively route internal cracking. [5] The third component of the SiC_f-SiC_m composite is the SiC matrix which provides rigidity to the composite. The Silicon carbide matrix can be applied by several different methods; all of which result in certain advantages and disadvantages to the production of the SiC_f-SiC_m composite cladding. [6] Deposition of the Silicon carbide matrix has been performed through the processes of chemical vapor infiltration(CVI), polymer impregnation/ pyrolysis(PIP), liquid silicon infiltration(LSI), and slurry infiltration/ hot pressing(HP).

The CVI process involves deposition of SiC by chemical decomposition of gaseous precursors, such as methlytrichlorosilane (CH3SiCl3), into the porous material until a high density and crystallinity SiC matrix forms. Despite the long process time, this process allows for the composite to be performed into a large number of shapes and geometries. [7] The polymer impregnation/ pyrolysis method involves injection of organometallic

polymers into the fiber architecture until curing and pyrolyzed at temperatures above 1000^{o} C. Several iterations of the PIP process are required to achieve the desired composite density considering that the precursor polymer shrinks when exposed to high temperatures. Another method, the liquid silicon infiltration method, involves application of a binding agent mixed with carbon particulates and SiC filler particles to the ceramic SiC fibers. After heating the material, liquid silicon is applied to the coated fibers at high temperatures. A reaction between the carbon and the molten silicon yields the desired Silicon carbide across the composite with relatively high density. The final fabrication process of SiC_f-SiC_m composites is hot pressing in which fine SiC powder, binders, and sintering additives, such as Al2O3 and Y2O3, are infiltrated into the preform and dried. To complete the fabrication, the composite material is hot-pressed at temperatures exceeding 1700^{o}C until densification is achieved. [8] Although mechanical properties of composites produced by this method are desirable for nuclear cladding applications, hot-pressing is limited on the geometry and length of material fabricated. Upon comparison between the above methods for fabrication of SiC_f-SiC_m composite cladding, there is great interest in CVI fabricated composites due to their superior mechanical and thermal properties, irradiation performance, and flexibility in complex component manufacturing. [9] However, a major drawback for the selection in fabricating SiC_f-SiC_m composites via CVI is the production time and cost compared to the rest of the methods. This, coupled with the cost of Hi-Nicalon Type S Silicon carbide fiber, makes fabrication of nuclear grade CMC cladding expensive at the current time. [10] *Figure 1.1*, below, visualizes the microscopic structure of CVI SiC_f-SiC_m composite.

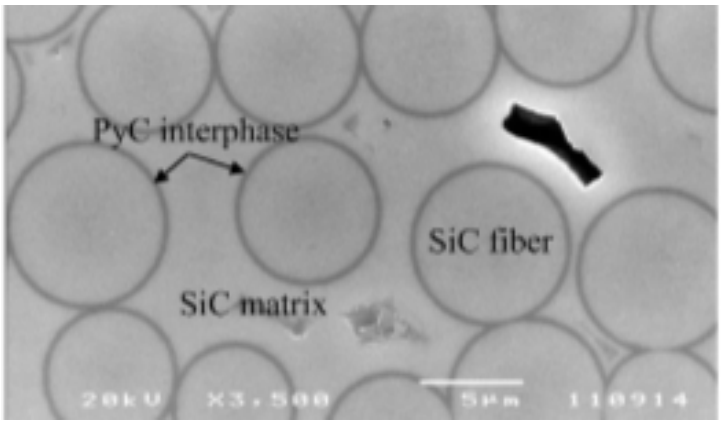

Figure 1.1: Microscopic Image of CVI SiC_f-SiC_m composite with a PyC interphase [10]

In addition, production of CMC material results in random formation of defects along the inter-space of the SiC_f-SiC_m structure during the various fabrication processes and during the composites useful life. As a result, nondestructive testing methods can be utilized to not only characterize composite material properties, but to monitor the structural integrity of the CMC material for internal damage that could not be performed by conventional testing methods.

1.2 Composite Damage

Non-destructive testing methods are excellent tools used to analyze and monitor composites for strength and internal damage. NDT methods can be used throughout the composites life without harming the component and can provide useful information in the future production of composite structures. [11,12] Composites experience damage in three stages of life; production of the structural fibers, assembly of the full composite structure, and service life of the composite after manufacturing. [13] During manufacturing, fibers may experience damage in the form of thinning or fracture. As a result, the interphase coating material on the fibers may become compromised and fail which leads to debonding between the fibers and the matrix in addition to inadequate stress distribution along the

fibers. Further defects can appear when the matrix material is applied to the fiber preform. Gas entrapment occurs when the matrix material does not completely adhere to all sections of the fiber structure. After composite construction, voids in which accumulation of stresses occurs within the material become present. Voids reduce the overall density and ultimately reduce the strength of the composite. In addition, further damage, such as delamination between composite layers, can propagate from void locations. [13] Damage sustained during the in-service stage of a composites life is typically a result of stress or fatigue induced upon the material. Sections with defects and initially damaged fibers from manufacturing are weakened areas of the composite in which mechanical and thermal stresses cause further damage. In *Figure 1.2*, below, Telreja shows the four major categories of composite damage as increasing amounts of stress. These categories are 1) Matrix cracking, 2) Crack coupling/ interfacial debonding, 3) Delamination, and 4) Fiber breakage.

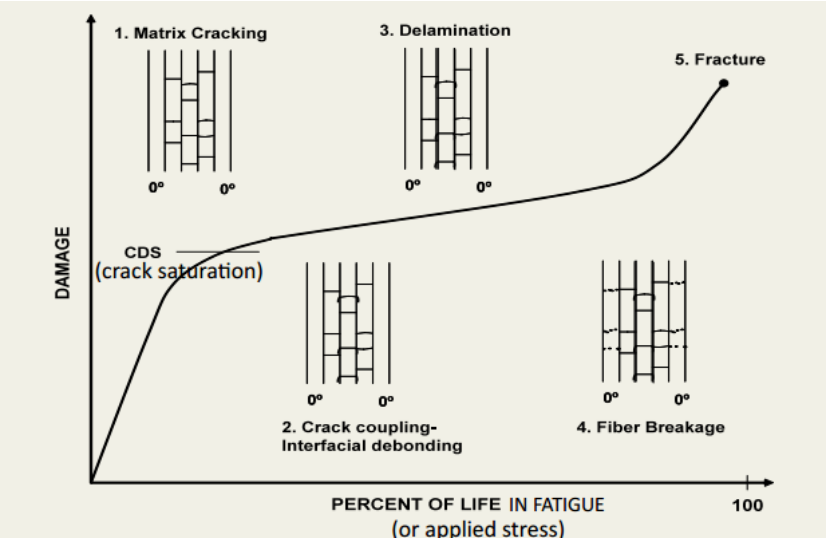

Figure 1.2: Plot of damage progression over applied stress to a composite [14]

Matrix cracking occurs earliest in a composites stress loading. This cracking initiates due to stress concentrations generated along the manufacturing defects and voids

created from the manufacturing process. As levels of stress increase, densification of micro-cracking in the composite matrix then leads to the interfacial debonding between the matrix and the fiber structure. Axial stresses along the fiber directions generate shear forces acting between the matrix and fiber. [15] Debonding initiates along the edge of a matrix crack that has exposed a fiber. With increases to axial stress along the fiber direction, debonded crack fronts continue along the fiber direction until delamination. Delamination occurs when sufficient interfacial debonding and matrix cracking are present in a composite to cause detachment of composites layers. Another key characteristic of delaminate is the large amount of fiber exposure and therefore greatly reduced distribution of stresses along the material. Telreja indicates that the final phase of composite damage is fiber breakage.

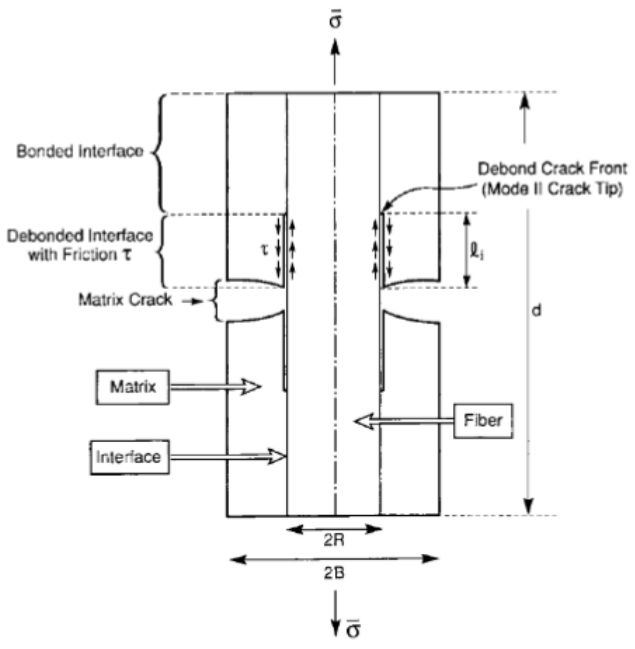

Figure 1. 3 Time dependent micro-crack development. [16]

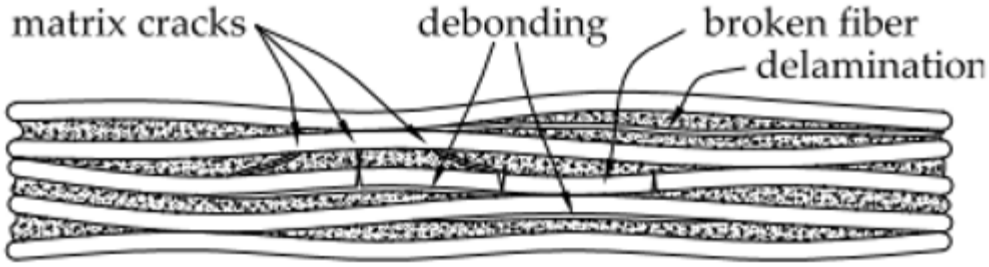

Figure 1.4: Various internal damages of composite material [13]

For the case of 3 dimensional composite tubular braids, the particular damage mechanics are the same as in composite plates, however, macro-cracking of material is dependent on specified loading boundary conditions. Rohmer noted the final material failure mode in SiC_f-SiC_m braided tubing under axial and hoop tensile loading. [3] This study revealed that braided composite tubing under axial tension loading experienced macro-cracking perpendicular to the axial load similarly to isotropic material tensile loading. Hoop tensile loading via piston driven internal elastomer insert expansion resulted in general material fracture along the axial direction of the tubing. In both cases, fiber pull out was prevalent along the exposed fractured edges of the braided composite.

1.3 Characterization of SiC_f-SiC_m Composites Cladding

Much research has recently gone into the characterization of SiC_f-SiC_m composites for the application of nuclear fuel. [3,17,18,19,20] Nozawa tested chemical vapor infiltrated (CVI) and nano-infiltration transienteutectic-phase sintered (NITE) processed SiC_f-SiC_m plain-weave patterned and unidirectional NITE processed SiC_f-SiC_m composites. Elastic Moduli for composites were determined by tensile and compression tests while Iosipescu method was used to find Shear Modulus. Stresses at PLS and failure were recorded and compared based upon fiber angle alignment with acting forces. [19] Nozawa was able to accurately predict failure stresses of materials based upon the Tsai-

Wu criterion. Kim characterized hoop tensile strength and crack propagation of triplex layered SiC composite tubing. The layer configurations of these tubes consisted of a chemical vapor deposited (CVD) SiC monolithic inner layer, a SiC_f-SiC_m braided composite mid layer, followed by a thin CVI SiC monolithic outer layer. The results of internal pressure tests via polyurethane plug expansion indicated enhanced mechanical hoop strength compared to non-layered designs. [20] Due to greater stresses along the inner most diameter of the tubing, cracking of the inner CVD SiC layer occurred before damage propagation continued radially to the other layers. It was noted that micro-cracking of the braided composite layer did not immediately occur after inner monolithic layer fracture. Stress concentrations were arrested temporarily by a thin PyC interphase layer between the composite and inner monolithic layer before higher loading continued radial growth of macro-cracking. Jacobsen compared the ultimate tensile strength (UTS) of nuclear grade SiC_f-SiC_m tubing generated by C Ring testing versus expanding plug testing. The C Ring tests involve cutting a slot axial through one side of the tube and compressing the cut tube sample, mechanical properties can be measured from the sample. This method of testing yielded UTS within 6% of expanding plug tests performed on the same architecture of composite tubing. [18]

1.4 Nondestructive Testing Methods

Considering the vast array of composite architectures for composite fabrication and the high manufacturing cost of CVI composite material, a fast and inexpensive method of material testing would be ideal to characterize CMC's mechanical properties. [20] Non-destructive testing (NDT) methods provide the solution to such an issue in which fabricated material can be accurately tested and monitored for dynamic properties in a controlled

environment without incurring some form of physical damage to the material. In comparison to conventional test methods, i.e. tension testing, impact testing, torsion testing, etc., NDT methods do not harm the integrity of the material under testing and can therefore eliminate the material and component loss during material characterization.[11]

Although the first official use of NDT methods is unknown, people have always performed some form of inspection of their work in some primitive way. With the discovery of X-rays by Wilhelm Conrad Rontgen in 1895, people began to develop methods for inspecting the internal components of a material. [21] It was not until decades later that NDT methods were implemented in an industrial setting. The first practical use of radium for gamma radiography was discovered in the 1930's by Robert F. Mehl, in which electromagnetic radiation is passed through a material to identify crack and abnormalities in a material. Shortly after, propagation of high-frequency sounds waves were monitored by Floyd Firestone and Donald Sproule as one of the earliest defect detection methods involving material vibration.[21] In the early 1950's, German researcher, Joseph Kaiser, discovered the correlation between a materials release of acoustic energy with the stress effects of solid material. This relation would later be developed into the acoustic emission (AE) testing method which would later become a useful tool for dynamic health monitoring of composites in the aerospace and nuclear fields. [22]

Nondestructive testing methods can be categorized into two groups: Contact and Non-contact methods. As the names, suggest, contact methods require some physical apparatus or component to physically touch the material during testing. [23] Some contact methods include magnetic testing, liquid penetrant testing, eddy current testing, ultrasonic testing and acoustic emission (AE) testing. Harding characterized the probability of defect

detention through the use of different liquid penetrant. [24] Harding emphasized the importance of surface crack detection in aircraft and spacecraft prior to and during the prototype development. Lu investigated defect identification via magnetic particle testing and even introduced a new magnetic particle testing intelligent detection device that conducts real time analysis of pressure vessels. [25] After an investigation into the defect detective effectiveness between eddy current, ultrasonic C-scan, and acoustic microscopy testing of carbon fiber reinforced plastics (CFRP), Gros outlined the advantages and disadvantages of each test. Gros found that of the three, eddy current testing, which involves passing an electromagnetic current through a conductive material, proved to hold the most advantages for testing CFRP material. In these tests, the amplitude of the electromagnetic current would change based upon the structure of the conductive material. [26] Ultrasonic testing relies on inducing a high frequency sound wave into a material and analyzing the reflected response by transducers. Based upon its great potential in the aerospace field, study of ultrasonic testing (UT) on polymer and composite material has been heavily investigated over the past decade. Wrobel experimentally found correlation between ultrasonic wave velocities and strength of polyethylene while Djordjevic characterized ultrasonic responses in composite material induced by non-contact laser impulsers. [27,28] The use of laser impulsers is a recent development in UT in which less interference can be observed due to the lack of contract between the material and the frequency generator. In the case of acoustic emission, transient sound waves as a result of mechanical movement and interaction are recorded by high ranged acoustic sensors. Acoustic emission is similar to ultrasonic testing except for the fact that sounds waves are not artificially generated in acoustic emission but are caused by micro-structural movement

and failure such as cracks, debonding, and material breakage. [29] AE testing has proved to be a useful tool in monitoring real time damage to composites. [29,30 ,31] From studies performed by Kim and Cohen, it has been found that sound waves propagate through composite material well and can be observed at low material stresses. It has also been seen that there is a relationship between the signals recorded by AE and the stress-strain behavior of CMC material. [31] Acoustic Emission testing will be performed as an additional study during the mechanical testing of CMC composite tubing in this paper.

In contrast, Non-contact testing can be employed depending on the testing environment. These tests typically require none or less contact between the sample and recording equipment. Many optical test methods are non-contact and utilize sensitive cameras and sensors that can operate a short distance away from the material under observation. [23] Optical testing methods include radiography, thermography, and shearography. Radiography involves the projection of electromagnetic radiation through a material. Depending on the density of particular sections of the material, the electromagnetic radiation will be absorbed by the dense material and thus preventing full penetration through the material. Radiation can then be captured by a detector on the opposite side of the material to develop the contrast between denser regions of the material. [13] Radiography has become a useful method for monitoring structural integrity of composites and has been studied in real time health monitoring. According to Oliveira, concurrent health monitoring of composite pipe seals can be performed during active flow of liquids in the piping. [32] Other methods like thermography, require monitoring thermal response of an object. After heating a material to a temperature above external temperatures, thermal surface gradients can be viewed with infrared cameras generated by

underlying defects. [33] Undamaged material will conduct heat in a uniform fashion, whereas, discontinuities beneath the surface alter the flow of heat to the environment. As a result, temperature gradients above the material defect can be seen by the infrared cameras.

Plotnikov performed thermographic defect visualization on flat composite samples and proved that a defect shape extraction procedure can be improved to generate higher resolution in thermal gradients created by composite defects. [34] Thermographic testing has been implemented in the testing of aerospace material due to its unique method for defect detection in composites and even has potential to be used for in-core nuclear applications. Another non-contact testing method is shearography, which is laser-based optical method that monitors material displacement fields. The method permits the detection of discontinuities through the visualization of defect-induced deformation anomalies. In a paper written by Hung, it was noted that in addition to defect location determination, shearography can also act as a non-contact strain measurement method for complex materials. [35] As a result of this characteristic, surface mounted strain measurements such as strain gauges can be avoided. The decision between utilizing Contact and Non-contact testing methods will play a part in how experimentation will be setup and performed. Care and forethought should be applied before any Nondestructive testing occurs. In this paper, impulse excitation will be the primary focus method for nondestructive testing of material.

Table 1. 1: List of Advantages and Disadvantages of various NDT techniques

Technique	Method type	Advantage	Disadvantage
Impulse Excitation	Contact	Fast, Inexpensive	Limited damage categorization
Acoustic Emission	Contact	Concurrent to material testing, Able to generate large amounts of data	Damage categorization difficult
Magnetic Particle Testing	Contact	Cheap, Fast damage identification	Limited to material use
Liquid Penetrant Testing	Contact	Cheap, Fast damage identification	Difficult to quantify damage
Eddy Current	Contact	Effective/ Accurate defect detection	Requires complex testing setup
Ultrasonic C-Scan	Contact	Effective/ Accurate defect detection	Requires complex testing setup, sample geometry is limited
Thermography	Non-Contact	Effective/ Accurate defect detection	Requires expensive setup, Requires large amount of calibration
Shearography	Non-Contact	Less sensitive to noise from mechanical testing	Sensitive to sample geometry, Requires large amount of calibration
Radiography	Non-Contact	Can generate imaging of internal voids/defects	Requires expensive setup, difficult to quantify damage

1.5 Impulse Excitation

Impulse Excitation testing (IET) is a non-destructive testing method that utilizes a specimen's natural resonant frequency to determine mechanical properties and damping characteristics. A material supported by its nodal points is lightly impacted to induce the vibration motion. A recording apparatus will record the vibration signal depending on the mode of vibration that the material is introduced. The captured signal can then be passed through Fast Fourier Transformation (FFT) algorithm to analyze the signal and to further determine prevalent frequencies and internal friction. [36] For isotropic materials, natural frequencies are directed related to an objects physical dimensions and elastic properties. Key properties of interest include Young's Modulus (E), Shear Modulus (G), and Poisson's ratio (υ) which all can be determined through IET of flexural and torsion modes of vibration. [36] *Figure 1.5* and *Figure 1.6*, below, visualize the flexural and torsion modes of vibration for a rectangular bar supported at nodal points.

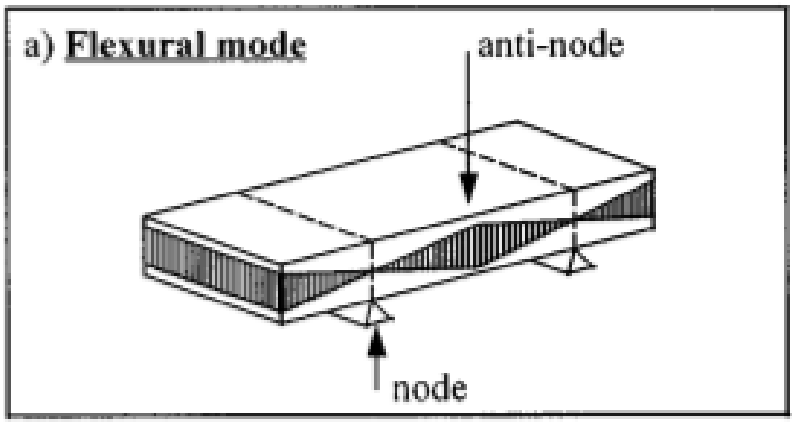

Figure 1.5: Location of Node and Anti-node of Rectangular bar in Flexural vibration

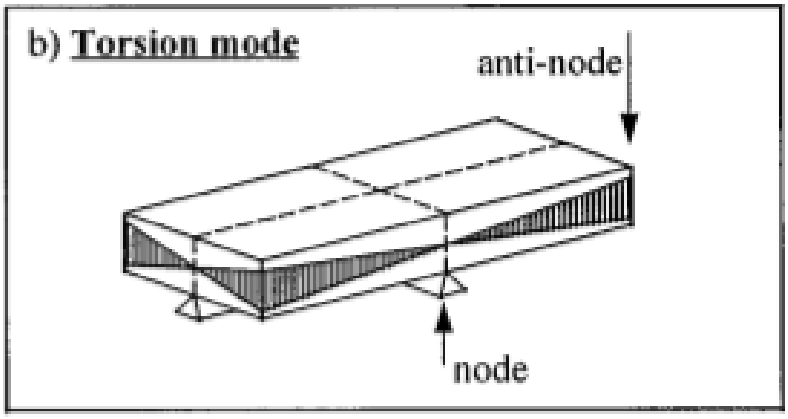

Figure 1.6: Location of Node and Anti-node of a Rectangular bar in Torsion

IET has become a recognizable method for determining dynamic elastic properties and has official standards written for the use of impulse excitation at ambient temperatures. [37] Standard ASTM E1876 specifically indicates the testing method and corresponding equations of dynamic elastic moduli for isotropic rectangular and cylindrical bars in addition to round disks. As an example, for the simplified case of a rectangular bar excited in the flexural mode, the equation for the dynamic Young's Modulus (E) is as follows:

$$E = .9465\frac{m{f_f}^2}{b}\frac{L^3}{t^3}T_1 \qquad \textit{Equation 1}$$

Where:

m- mass (g)
f_f - natural flexural frequency (Hz)
b- bar width (mm)
L- bar length (mm)
t - bar thickness (mm
T_1- Correction factor dependent on bar length to thickness ratio and Poisson's ratio

Due to the more complex geometry of the CMC structures tested in this paper, more general equations relating the material natural frequency to dynamic moduli (Young's and Shear) will be used. These equations will be discussed further in study.

The sample support can significantly impact the frequency and damping collected via IE. The standards indicate that for a simple rectangular or cylindrical bars, low damping supports must be used at the node locations. This is to prevent any parasitical damping of the vibration motion that could otherwise alter the recorded resonant frequency to any other than the natural frequency of the material. Standard E1876 indicates that one of several support options can be used for impulse excitation. The first option is a soft, foam like material, such as polyurethane foam strips. [37] This strip should be wide enough to appropriately support the testing material without interfering with the transverse vibrational motion. The second option is the use of a metal or rigid support material; however, the rigid support must have little contact surface with the testing material. As a result, the standard calls for the rigid support to be a sharp knife edge or cylindrical surface. The final recommended support for impulse excitation of a bar is elastic or metal wiring capable of rigidly suspending the material. As mentioned, test specimens should only be supported along the nodal locations depending on the desired mode of vibration. Vibration nodes are locations where transverse motion is at the lowest as opposed to anti-nodes, where the material experiences the greatest local displacement. *Figure 1.5* and *Figure 1.6*, above, give good visualization of these regions. It is at the anti-node that the recording microphones are to be placed in order to acquire the greatest amplitude of the fundamental frequency.

In addition to frequency, another phenomenon that can be quantified by IET is internal friction, which can be defined as the dissipation of mechanical energy within a solid medium. [38] Considering a time-dependently loaded solid material, energy absorption during a single cycle can be compared to the maximum elastic stored energy in

that cycle. As a result, "specific damping capacity (ψ) can be defined as the ratio between the energy absorbed (ΔW) to the maximum amount of stored energy (W) in that cycle. Lazan observed this characteristic in solid metals and defined the term quality factor (Q) as $2\pi/\psi$. [39] In addition, Lazan further defined the reciprocal of quality factor as internal friction (Q^{-1}), seen in the equation below.

$$Q^{-1} = \frac{\Delta W}{2\pi W} \qquad \textit{Equation 2}$$

For several decades, impulse excitation has been of great interest in the nondestructive testing research community. [36,40,41,42] As a nondestructive testing method, IET has several key characteristics over other methods that make it a reliable and useful method. In addition to the capability of determining elastic moduli through resonant frequency analysis, structural integrity can be monitored for internal defects. Structural integrity can be quantified by a materials internal friction. [41] It can be seen that increases to mechanical or thermal stresses, result in greater material damage. There is a vast array of damage mechanics that can occur in a stresses material based upon the material type, be it metal, composite, ceramic, polymer, etc. As a result, the amount of dissipated energy increases due to this material damage. Using impulse excitation can determine a numerical value that can be associated to a materials structural health and can be monitored over the life of the test specimen as greater fatigue is induced upon the material. Unlike testing methods like UT, LPT, or magnetic testing, IET can quantify specimen health or damage concurrently with applied stress testing. [40]The importance of this is that a test setup will not need to be disrupted to perform NDT and total testing time can be shortened.

The software used to record acquired vibration signals from the test specimen is a Resonant Frequency and Damping Analyzer (RFDA) software. This software is able to analyze a large array of incoming frequencies. The RFDA professional software, produced by IMCE, has the capability to record the waveforms of the total mass of frequencies picked up via the microphone and isolate any frequency. Figure 1.7, below, shows the acquired mass of frequencies taken from a single impulse of the material.

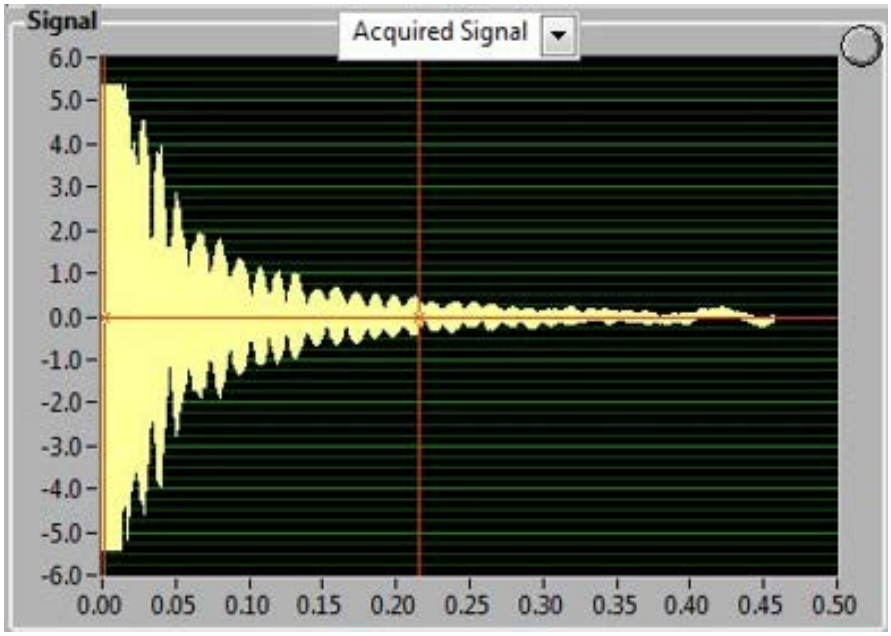

Figure 1.7: Total Acquired Signal from all frequencies recorded by one impulse of the material

The RFDA software is then capable of passing all recorded frequencies through a Fast Fourier Transform (FFT) and plot out the amplitude of the signals based upon the corresponding frequencies. *Figure 1.8*, below, shows the FFT plot of a single recorded impulse. The software can be set to automatically determine moduli of the material based upon the equations defined in the ASTM 1876 standard. Prior to data collection, the physical geometry and properties of the sample can be inputted. In addition, the method of vibration (torsion, in-plane transverse, out-plane transverse) of the sample must be

designated in order for the software to calculate the moduli. This is limited to simple geometry bars of circular or rectangular cross-section and round disks. For more complicated sample geometry, alternative equations must be used, however, are still able to produce accurate results. Several studies were performed for this paper to validate that these alternative equations can be used for geometries different than those mentioned in the ASTM standards

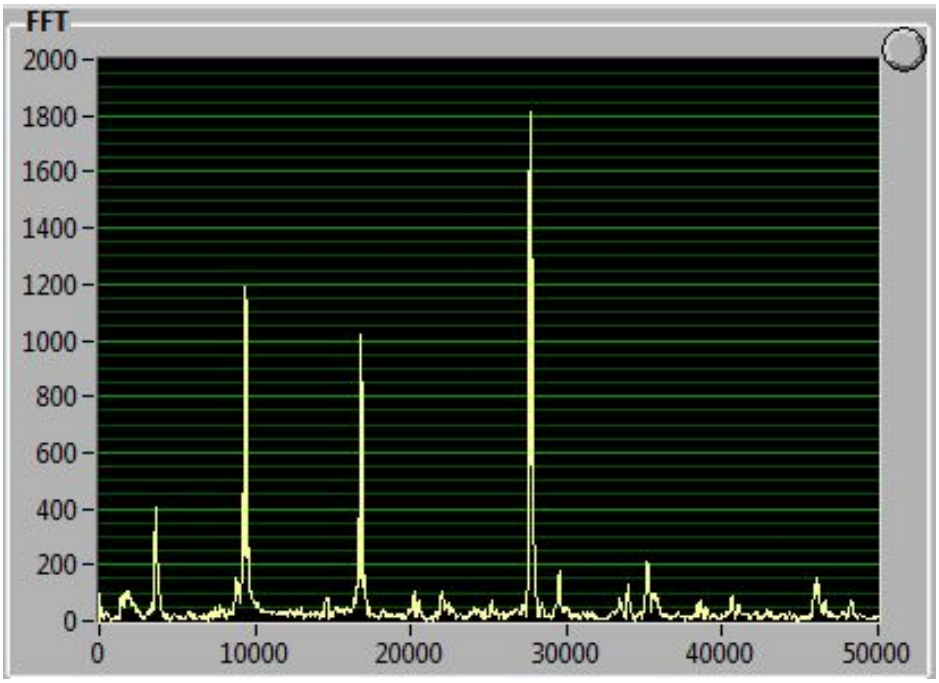

Figure 1.8: Range of Frequencies with corresponding Amplitudes from Fast Fourier Transform

1.6 Application of Impulse Excitation

Much research has been performed on the applications of impulse excitation in regards to the various materials tested and the various material aspects that can be analyzed. [36,40,43,44,45] The conclusions of earliest IE research led to the standardized testing methods such as ASTM 1875 and 1876. These standards were specified for use with isotropic elastic materials at ambient temperatures, however, recent studies have been performed on different materials under alternative conditions.

Computation of theoretical transverse vibration of bars with uniform cross-sections performed by Timoshenko and Pickett led to the experimental determination of flexural and torsional resonant frequencies of isotropic bars. [46,47] Timoshenko was one of the pioneers that investigated the effect of shear deformation and rotational bending on the dynamic motion of beams of uniform cross-section under various boundary conditions (simply supported, free, clamped, etc.). [46] In the late 1950's, Spinner performed rigorous experimental testing of Timoshenko's theories and found good agreement with the results. [48] It is from this research that the ASTM standards for the use of resonant frequency analysis and impulse excitation are based.

With the creation of the steam turbine and other high speed machines, it became apparent that a method for determining fatigue of the rotating components was needed. [49] Metals were the primary material used in the high speed turbine components and were the first types of material that vibration analysis was performed on. In 1939, Rathbone, a plant engineer, made the observation of the displacement of certain rotating shafts at low frequencies and correlated these to the integrity of the shaft. [50] Empirical observations such as this would eventually lead to the experimentation performed by Spinner to validate previous vibration theories.

As technology advanced and more complex computational tools became available, investigation of more than a materials resonant frequency was performed. Impulse Excitation permits the non-destructive testing of material for frequency and internal friction (damping properties) in harsh environments that would otherwise disrupt the use of other NDT methods. In regards to metals, IET is a common method for testing. Heritage investigated the various testing setups for impulse excitation of pure Aluminum specimens

at elevated temperatures. [51] It was concluded that under certain configurations, wave guides can be used to consistently deliver the vibration signal of the sample to the acoustics microphone. These findings correlated well with mechanical testing and piezoelectric ultrasonic composite oscillator technique testing of the pure Aluminum. Radovic performed similar IET on aluminum and steel samples of various geometries and found good correlation between the resulting moduli and those found by resonant ultrasonic spectroscopy and 4 point-bending tests. [52] Swarnakar and Jung performed IET on TiB_2 and structural steel, respectively, and each found damping peaks that correlated to phase changes in the metallic microstructure. [53,54] Another study involving the damping behavior of material structural integrity of metals was performed by Goken. It was determined that an increase to material damping resulted from crack growth during prolonged heat treatment in magnesium alloy. [55]

In addition to metals, polymers are an excellent material to perform IET on due to their viscoelastic nature. [45] A viscoelastic material exhibits the characteristics of both viscous and elastic materials in which a viscoelastic material will dissipate stored energy during unloading in the material's elastic stress range. As a result, polymers have become suitable interface and matrix material for high damping composites. Finegan noted various enhancements to composite materials that would improve damping properties. It was found that various layering configurations of polymer interfaces in a composite yielded reasonably high damping. In addition, it was mentioned that co-curing of embedded layers and hybridization of laminae under various fiber orientations enhanced the loss factors of the material. [56]

Much study has been performed in regards to nondestructive testing of ceramics via resonant frequency analysis and impulse excitation. [36,57] Despite having low damping characteristics, monolithic ceramics are excellent subjects for nondestructive testing due to their primary failure mode of micro-cracking. Ceramics tend to have high thermal resistance and are therefore used for various high temperature applications, such as turbine and engine structural components. As a result, non-destructive testing can be applied to ceramic materials exposed to high temperature testing via IET. Studies performed by Roebben greatly involved exposing ceramics to elevated temperatures and initializing IET on the samples to validate internal defects and phase alterations. The same Resonant Frequency and Damping Analyzer (RFDA) used in these studies was used in experimentation performed for this work. In one of the studies, Roebben investigates the effect of elevated temperatures on the damping characteristics of oxide (Al_2O_3 and ZrO_2) and non-oxide (Si_3N_4) ceramics. The findings indicated that little frequency and damping changes occurred below 1000^o F, however, quickly progressed at higher temperatures due to mobility of grain boundary defects and softening of secondary material phases in Al_2O_3. [36] Damping peaks were found for ZrO_2 that corresponded to the thermally activated displacement of compensating oxygen vacancies that were present throughout the materials thermal loading. In this same paper, damping peaks were observed during the loading and unloading cycles of the Si_3N_4 due to the crystallization of intergranular phase of the non-oxide ceramic. Another study by Roebben on IET of SiC and Si_3N_4 ceramic samples found that variations of the annealed composition affected the damping amplitude of material damping peaks. [58] Bemis performed IE of thermal shocked monolithic SiC rings cut from heat exchanger tubing. The precision cut rings were heated to increased intervals of

temperature and impulse after each heating and quenching cycle for resonant natural frequency and damping collection. [44] After first heat cycling to 250^{o} C, only a damping change of 0.3 % occurred, however, a damping change of nearly 50.0% was found after the ultimate cycle to 800^{o}C. It was observed that visible cracking began after quenching cycle from 400^{o}C to room temperature. Although moduli was not determined from this experimentation, it can be clearly seen that IET provides useful health monitoring for thermally shocked materials prone to material cracking under rapid temperature changes.

Impulse Excitation has been of particular interest in regards to testing composite materials. As mentioned in previous sections, damping characteristics are greatly influenced by a materials micro-structure. [36,58] Considering that composites experience a variety of micro-damage (micro-cracking, delamination, fiber break, etc.), this enables IET to be an excellent method for non-destructive testing as seen from the recent research performed. [41,42,43,59] Experimentation on glass and graphite fiber composite cantilever (fixed-free) beams was performed by Crane, in which changes in loss factor was correlated to changes in beam length. Crane determined that increases in beam length resulted in an increase of loss factor and therefore the damping properties of each of the composites. [41] A significant point behind this study was that it showed how impulse excitation testing could be performed on a sample held in a cantilever mode of vibration and still produce reliable results.

In a study conducted by the National Aeronautics and Space Administration (NASA), IE on various graphite/ epoxy composites for Dynamic modulus determination was compared with conventional mechanical testing and laminate theory. [40] This study validated IET as a quick and accurate method for calculating elastic moduli of laminate

materials and emphasized how the method had potential for concurrent quality control. Atri conducted IET of MMC composites for elastic modulus determination. These samples consisted of discontinuous titanium-monobromide (TiB) whiskers of random orientation imbedded in a Ti matrix with volume fractions ranging from 30 -83% TiB. Calculations for moduli (Young's modulus, Shear modulus, and Poisson's Ratio) followed equations implemented by those in ASTM standard 1876. A trend was found in which as TiB whisker volume fraction increased, Young's and Shear moduli for the composite increases as well. Properties calculated from IET correlated strongly with those of conventional mechanical testing for all samples. Impulse Excitation can effectively be implemented on composite material and can be confidently used in this paper.

1.7 IE Testing of SiC Composites:

For this study, IET will be used to both non-destructively determine elastic moduli and monitor structural integrity via damping properties changes for SiC_f-SiC_m braided composite tubing for nuclear fuel application. As mentioned, the goal is to investigate possible applications for the testing method while conducting accurate material testing that is comparable to the current nuclear industry. Since the 1970's, three generations of SiC fibers have been constructed for potential nuclear fuel use. The first two contained much oxygen and carbon impurities, therefore densification of the fibers occurred and mechanical properties of the SiC-SiC composite structure degraded over time when exposed to neutron irradiation. [1] In the latest generation of SiC_f-SiC_m composites, Hi-Nicalon Type S grade Silicon carbide fibers were implemented which yielded less degradation of mechanical properties when exposed to higher temperatures and neutron dosages. [12]

Although a fair amount of mechanical testing has been performed on SiC_f-SiC_m braided composite tubing, not much non-destructive testing has arisen since the initial development of CMC's for nuclear fuel. [3,17,18,19,20,60] The current state of the art primarily utilizes acoustic emission to monitor the CMC braided tubing for concurrent damage evolution and micro-structural changes. In more recent studies, micro-crack identification has been performed using Electrical Resistance (ER) testing for ceramic matrix composite materials. [61,62] For this procedure, an electrical current is passed through the material and the electrical resistance is recorded. This resistance correlates to the density of fiber and matrix cracking present in the composite material. Although both AE and ER testing have been proven to be excellent structural monitoring methods, impulse excitation has the capability to determine material elastic moduli in addition to numerically quantifying correlated material damage.

Thus far, IET of SiCf-SiC_m composite has been limited. Of the research that has been performed on SiC_f-SiC_m composite material, studies on simple geometry of rectangular cross-sectioned bars has been conducted. Work at Oak Ridge National Laboratory (ORNL) determined that using the equations set in ASTM standard 1876 yielded accurate and repeatable modulus calculations for prismatic bars of SiC_f-SiC_m woven composite. [63] In this study, it was found that of three samples tested, standard deviation of the resulting Young's Modulus in the longitudinal direction of the woven samples came within less than one percent of the average modulus taken. This low deviation in data matches well with those found in other studies involving IET of woven CMC material.

Identification of micro-cracking within CMC cladding under elevated thermal and mechanical loading can play an important part in the design process for future nuclear fuel. Should IET be employed as a commercial method for health monitoring of SiC_f-SiC_m composite cladding, composite structures may be designed to more adequately accommodate vibration analysis before and during use in reactor. Although not available in this paper, fiber orientation of fiber reinforced braided tubing could be tested for improvements to damping properties. In addition, a more in depth investigation of the various metal matrix components could be conducted to improve mechanical failure and damping capabilities. IET would also have some effect on the total fuel cycle in which time for material strength analysis of cladding while in core could potentially reduce. [20] Unlike other NDT methods, IET requires less equipment and is therefore less cumbersome. Cost for IET equipment is also significantly less than other methods that require complex layouts of hardware.

CHAPTER 2: EXPERIMENTAL SETUP

2.1 Tension Setup

Tension testing of the SiC_f-SiC_m composite tubing was performed using an ADMET eXpert 2611 universal material test machine with MTESTQuattro software to determine the Elastic Moduli in the axial direction of the tubing. To grip the hollow, cylindrical specimen, a set of adapters were designed and fabricated to ensure that only axial loading would be applied to the sample during tensile testing. Composite tubes that were meant to be tested for tensile properties had a cylindrical nut adhered to each end of the sample. This nut will be referred to as the sample adapter nut and is compatible with both the tension and torsion adapters that connect the sample to the mechanical rigs. To allow co-axial alignment between the sample tube and the adapter nuts, the sample and adapter nuts was clamped on to supportive V-blocks before adhesive curing. The center v-block supporting the sample tube was then shimmed appropriately for alignment. Figure 2.1a and b, show details for adapter nut attachment.

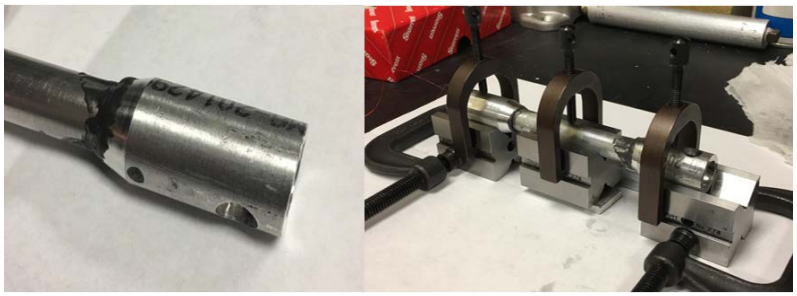

Figure 2. 1 a (left): Sample adapter nut adhered to the end of sample tube. b (right): Supportive V-block setup to allow adapter nut curing.

Figure 2.2, shows the sample adapter nut inserted and pinned with the tension adapter connector. The sample adapter nut is constructed using 3/4" outer diameter (OD) Aluminum rod with an axial through hole that is slightly oversized than the OD of the tubular sample. The axial through hole was cut to be approximately .020" larger than the test sample. The end of the sample adapter nut was machined into the shape of a cone to prevent any unwanted stress concentration development in the sample at the adapter nut end. A 3/8" through hole was milled perpendicular to the adapter nut axis for a connector pin to the adapter connector. The adapter connector, as seen by the design schematic in *Figure 2.3*, is constructed from a high strength tool steel. The purpose of the connector is to eliminate parasitic bending and to allow self-alignment during tension testing. This will ensure that loads applied to the sample are only along the axis of the tubular sample.

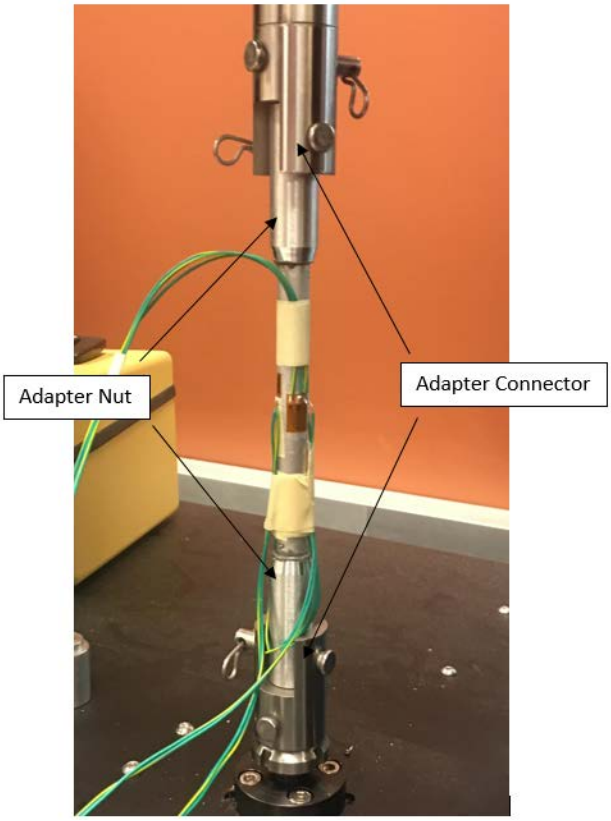

Figure 2.2: Adapters and connectors of a tensile test specimen

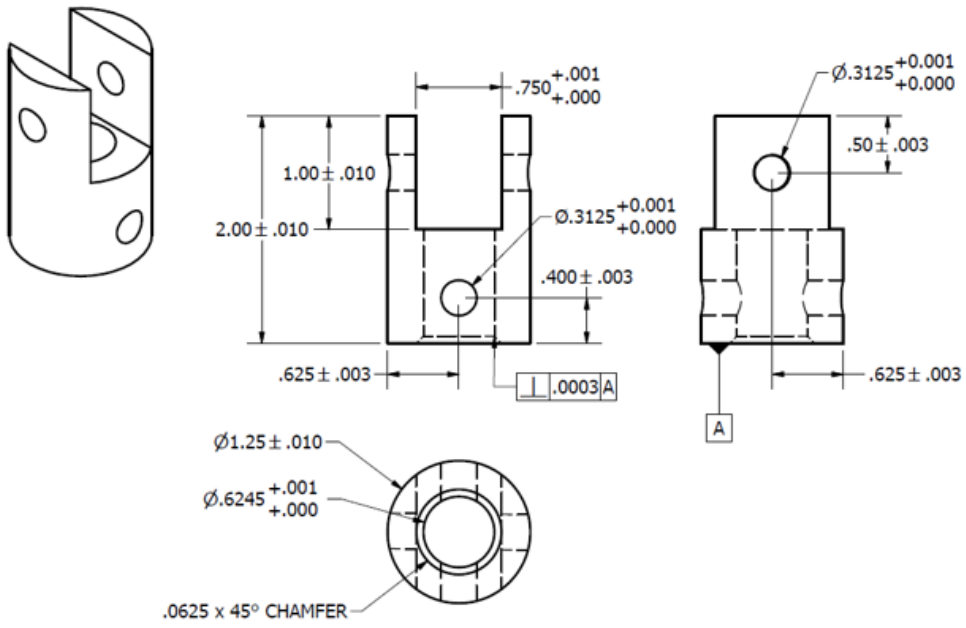

Figure 2.3: Schematic of adapter connector for tension

A similar tension test setup was used by Rohmer in tension testing of hollow SiC_f-SiC_m composite tubing, as seen in *Figure 2. 4.* [3] Rohmer epoxied the composite tubing ends into cylindrical aluminum tabs to adequately hold the sample along the axial direction. Strains were read using Digital Image Correlation (DIC) of the sample and extensometers.

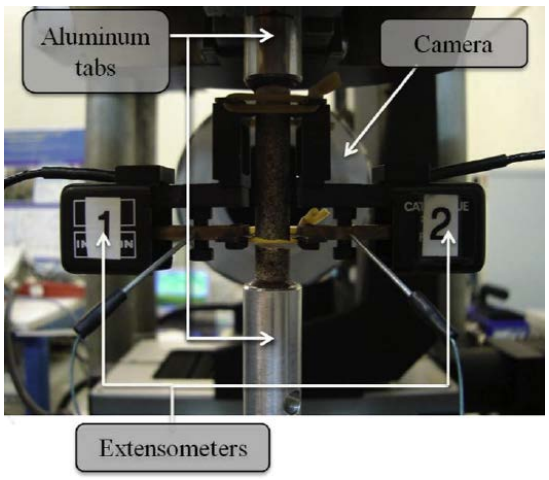

Figure 2. 4: Axial tension testing of SiC_f-SiC_m composite tubing with extensometers [3]

2.2 Torsion Setup

A torsional rig was designed and constructed for the purpose of torsion testing of cladding tubes. As shown in *Figure 2.5*, the rig was built on an aluminum structural rail with high torsional rigidity. Along the railing, two movable aluminum platforms were rigidly bolted to the railing. At the external end of each of these platforms are shallow, cylindrical recesses that fit circular tool steel wrench heads. Slots are cut through the platforms to the center of the recesses to allow sample tubing to be placed between the platforms. The lower wrench has a load cell bolted to the end which will read the force exerted on the system during testing. The upper wrench can be attached to a motorized actuator or operated manually. For torsion testing of material for this study, only a small amount of torsional force is required and therefore the torsion will be delivered manually. To conduct as many mechanical tests as possible with such a few number of tubular samples, all tension and torsion tests will be performed to simply to determine moduli and not ultimate stresses. *Figure 2.5*, below, shows the operating components of the torsion rig.

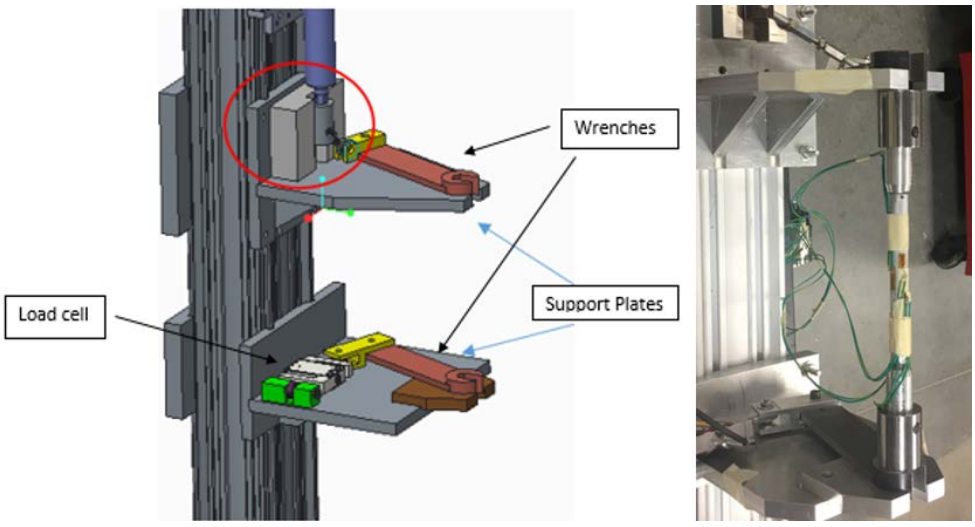

Figure 2.5: a (left): Schematic of the torsion rig. b (right): Image of sample tube in torsion rig

The hex shaped slots in the wrenches accommodate a 9/16” nut. As result, in lab fabricated adaptor nuts must be created and adhered to the ends of the tubular samples to adequately transmit force to the sample for testing. Two adapter connections were made out of high strength steel rod of 1-1/4” diameter. A shallow, inner hole was milled to closely fit the OD of the adapter nuts and a 3/8” pin hole was cut perpendicular to the axis of the adapter connection to hold the adapter nut. On the opposing axial end of the adapter connection, hexagonal studs were milled to closely fit the hex slot of the torsion wrenches. *Figure 2.6* and *Figure 2.7*, shows the schematic of the adapter connector for torsion and total adapter configuration for the torsion rig, respectively.

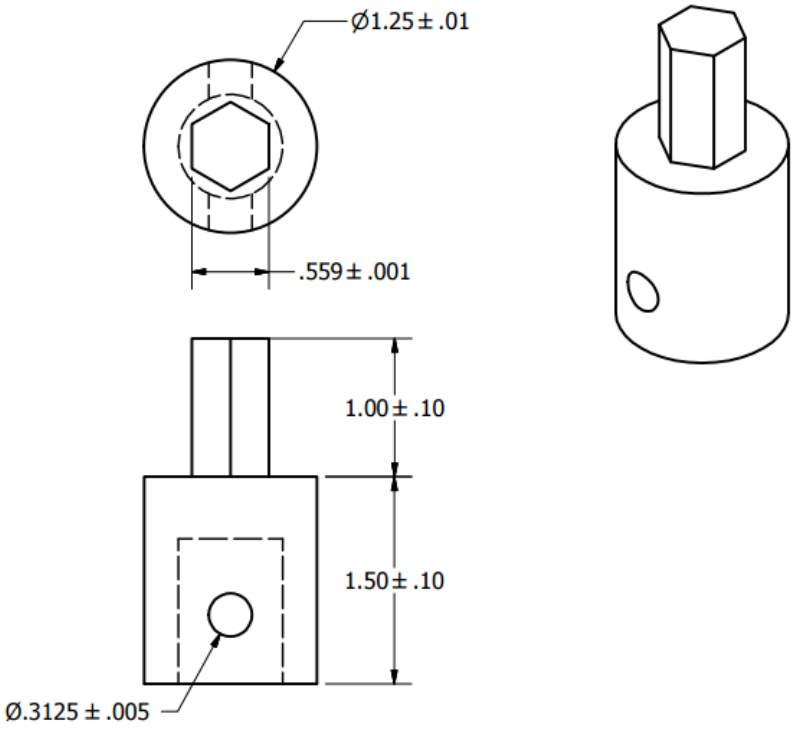

Figure 2.6: Schematic of adapter connector for torsion.

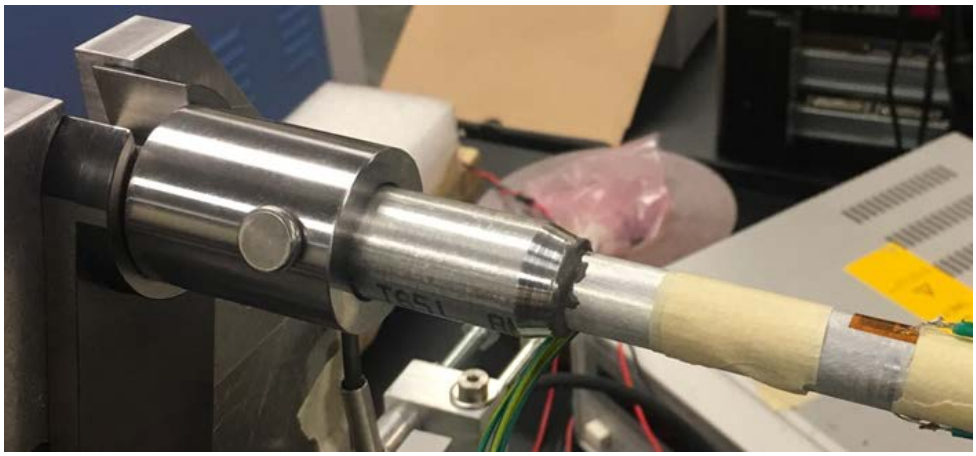

Figure 2.7: Adapter configuration to transmit torsion to the tubular sample

2.3 Internal Pressure Setup

To induce internal pressure of the tubular sample, an updated version of the Internal Burst Rig utilized by Alva and Shapovalov was used for pressure testing. [17,60] The Internal Burst Rig operates by pressurizing a flexible, polymer tube (part # 5006K66 from McMaster) with food grade hydraulic oil to expand it inside the testing sample and exert mechanical stresses primarily in the hoop direction. A manually operated hand pump (Model 37-6-30 from High Pressure Equipment Company) is connected via high pressure tubing to an analog pressure gauge in addition to a digital pressure sensor (Model PX01S1-20KGI Pressure Transducer by Omega Engineering). The analog gauge is used for visual monitoring of the internal pressure by the operator. The high pressure metal tubing system then leads to the polymer bladder which is connected to the sample mount. On the sample mount are a series of brackets and telescopic adapters that hold the tubular sample with the polymer bladder threaded through. To accommodate various sample tubing lengths, the rig end was designed to be adjustable. In addition, a large assortment of sample adapters were created for testing of tubing with different inner diameters. *Figure 2.8* shows how an adapter connects to the test sample.

Figure 2.8: Image of adapter supporting test sample during internal pressure test

All composite samples used in the impulse excitation study were internally pressurized. The first sample was tested to determine mechanical properties while the remaining composite samples were systematically loaded and unloaded. These loadings were to increasing internal pressures while frequency and damping are recorded after every cycle. To maintain consistency between each IE recording, the upper vibration clamp and the lower support clamp will not be removed. Any adjustment of these two components could affect the rigidity of the support for the tubular and thus alter the recorded vibration. After each increase in pressure loading, the upper segment of the pressure rig, including the telescopic and sample adapters, will be raised away from contact with the sample. The polymer bladder will also be stretched upwards to ensure no interference with the tubular sample's vibration motion.

The horizontal brackets serve to maintain proper alignment of the sample and to adequately distribute any axial loading from the sample to the supports of the pressure rig. Steps in the horizontal brackets and sample adapters eliminate these axial loads while

pressure is applied to the system. In addition, the lowest horizontal bracket has through holes near the center of them to allow bolting of the support clamps for the IE tests. Once the composite samples are installed on the pressure rig, the support clamps are then bolted to prepare the samples for rig mounted IE.

2.4 Mechanical Validation

2.4a Tension and Torsion

Tension testing of materials is very accurate for determining elastic moduli using the ADMET tension tester, however, it is important to validate whether the adhering of the adapter nuts to the sample have an impact on this testing. To prove that the desired adapter configuration is adequate, tension testing was performed on Aluminum alloy 6061tubing (McMaster part # 9056K64) before testing of the SiC_f-SiC_m composite. Aluminum 6061 is a common and inexpensive material with accurately known mechanical properties. A 6" aluminum specimen of 1/2" OD and ¼" ID was cut and had sample adapter nuts adhered to each end by high-strength JB Weld epoxy. Prior to installation, the adapter nut had an axially drilled 3/8" through hole to serve as an air way when the adapter nut and sample are adhered. A 1-1/2" deep hole of diameter slightly larger than the sample OD was drilled to accommodate the tubular sample. Tubular specimen and adapter nuts were set in a set of V-blocks for curing. Thin aluminum shim was used to properly align the axis of the nuts and the specimen. This will help reduce and transverse bending that the sample may experience during the axial loading.

After epoxy curing, two linear strain gauges were installed to the outer surface of the aluminum sample in the axial direction. To also account for any transverse bending, these strain gauges will be placed at 180 degrees radially from each other. During post-

analysis of the tension test, the average between the strain gauges will be taken. Strain and load readings will both be recorded via the ADMET software which will be programmed to load to no more than 400 N of axial force at a cross-head displacement rate of .066 in. per minute. Due to the high sensitivity of the strain gauges, low levels of force are need to displace the sample and determine moduli. In addition, low level of axial force will be applied during all mechanical tests to prevent any sample yielding or cracking depending on the material.

After tension testing of the aluminum tubular specimen, validation of the torsion rig must be achieved. Based upon design of the adapter nuts and connections, the adapter nuts used for tension testing are compatible with the torsion rig as well. As such, the only augmentation of the aluminum specimen that must be done is to have a shear strain gauge installed along the axial direction. Each adapter nut can then be pinned into the adapter connectors and then be set into the torsion wrenches. As mentioned before, torsion of the tubular sample will be performed manually to ensure that the torque on the sample will not damage the sample.

2.4b Internal Pressure

Validation of the internal pressure rig was performed previously by Shapovalov. Shapovalov tested aluminum tubing and found accurate results compared to published values. [17] The short tubes of aluminum were tested with four strain gauges attached, two in the hoop and two in the axial directions. Shapovalov also validated uniformity of internal pressure applied throughout the length of the sample. An aluminum tube of 304 mm had strain gauges attached along the hoop direction of the tube at locations 50.8, 152.4, and 254 mm. Strain reading at each of these locations were compared to ensure uniform

pressurization of the tubing along the entire length of the sample. Equations used to calculate inner and outer stresses are the thick-walled cylinder equations as seen below. These same equations will be used in this study for comparison on validation and composite materials.

$$\sigma_i = \frac{(r_o{}^2 + r_i{}^2)P}{(r_o{}^2 - r_i{}^2)} \qquad \textit{Equation 3}$$

$$\sigma_o = \frac{2r_i{}^2 P}{(r_o{}^2 - r_i{}^2)} \qquad \textit{Equation 4}$$

Where σ_o is hoop stress at the outside surface of the sample, σ_i is hoop stress at the inner surface of the sample, P is the internal pressure, r_o is outer radius, and r_i is the inner radius. For simplification, it was assumed that the atmospheric pressure outside of the tube was negligible. For all elastic moduli calculations, the external hoop stresses will be used considering that external strains will be recorded. Tubular sample exposed to internal stresses experience the greatest amount of stress at the inner surface and therefore the internal stresses will be noted to characterize strength of tested composite material. For comparison, a pressure test of an aluminum 6061 tube will be done to ensure that testing setup for internal pressure is similar to validation performed by Shapovalov.

2.5 Table Mounted Impulse Excitation

As mentioned, impulse excitation testing will be carried out using RFDA System 24 hardware, seen in *Figure 2. 9*, and RFDA professional software created by IMCE inc. under two separate setups: table setup for free vibration and pressure rig mounted setup. Most IE is performed by suspending the sample from the nodes through the use of soft polymer, single point metal support, or wire supports. [36,37] For table mounted testing,

all IE test specimens will be supported by elastic wiring set on a testing rig produced by IMCE Inc. By setting the wiring support at the nodal locations, transverse displacement of the material will not be affected and the amplitude of the material's natural frequency can be easily recorded.

Figure 2. 9: RFDA System 24 hardware used for IE testing [64]

For table mounted IE tests, two configurations will be used to determine axial elastic modulus for the composite material. The first, as seen in *Figure 2.10*, is free-free testing in which transverse vibration of the sample is recorded. The recording microphone is set normal to the upper face of the sample end while the impulse will be delivered at the very center of the sample. The greatest displacement can be found at the sample ends and are the vibrational anti-nodes of the material. For convenience, table mounted IE supports will adhere to ASTM standard E1876.

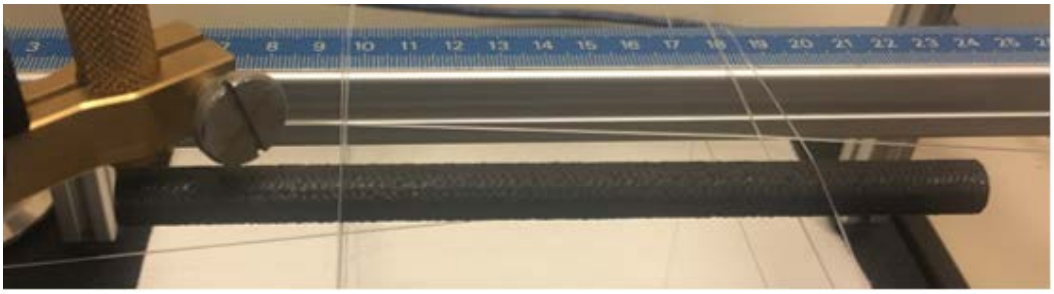

Figure 2.10: Recording setup for free-free vibration via table mounted IE

Similarly, for the longitudinal vibration of the composite sample, the specimen will be supported in the same way as in the free-free vibration; by the nodes. This configuration of support will not have an effect on the longitudinal motion of vibration. In addition, the recording microphone will be placed at the sample end, facing the axial direction of the sample. For this mode of vibration, the impulse will be administered on the opposing face of sample as seen in *Figure 2.11*.

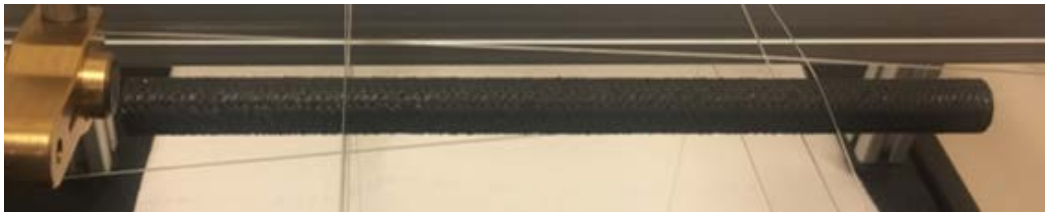

Figure 2.11: Recording setup for longitudinal vibration via table mounted IE

Due to the complex geometry of the tubular sample, the equations designated in ASTM 1876 will not be applicable to this study, however, alternative equations using Euler-Bernoulli classical transverse and longitudinal vibration beam equations were used. [46] For both equations, it will be assumed that the specimen is of uniform cross-section along the beams and that the material is isotropic. For beam vibration derivation, refer to Appendix B.

2.6 Pressure Rig Mounted Impulse Excitation

2.6a Fixed- Free Mode

Nuclear fuel is exposed to many various types of stresses while used in core, however, one of the greatest sources of mechanical stress is due to the internal pressure generated from the generation of fission gases. [12] As such, damage to the CMC tubing samples will be performed on the internal pressure rig to simulate some Loss of Coolant Accident (LOCA) conditions. For structural health monitoring of composite material with increasingly applied internal damage, a testing method was devised that could be integrated into the internal pressure rig. In addition to standard pressure rig setup, the tubular samples will have lab fabricated clamps attached at either end for flexural and torsional impulse excitation testing.

Both clamps were constructed using 1-1/2" shaft collar clamps with a 7/16" hole milled through the center. This hole is intentionally cut oversize to the nominal SiC_f-SiC_m tubing OD considering that tubing of different architectures have varying dimensions. Layers of aluminum foil will be placed between the sample and the inner cut of the clamp to sufficiently distribute clamping forces around the sample. Due to the SiC_f-SiC_m composites brittle structure under compressive loads, it was considered to be best to avoid stress concentrations along the OD of the composite; thus the aluminum foil was used. The lower clamp had two threaded holes cut in order for the clamp to be bolted down to the lower support bracket, as seen in *Figure 2.12*. Both flexural (transverse) and torsional vibration of the tubing assume one end fixed and the other end free boundary conditions.

Figure 2.12: Pressure rig mounted IE setup for flexural and torsional testing

The upper clamp has four identical steel wings adhered 90 degrees from each other. Recording of IE measures will be from one of these wings while the initial impact to induce the vibration will be delivered to another wing. Four wings were used to make the upper clamp symmetrical along all directions. For torsional vibration, it is required to know the upper clamps mass moment of inertia. Due to the clamp's complex geometry, manual computation of the mass moment becomes difficult. As a result, the mass moment of inertia was measured using a trifilar pendulum in which the clamp was set on a thin plastic plate of known moment of inertia that was suspended by three evenly spaced wires. Using classical equations of motion for trifilar pendulums, mass moment of inertia of the upper clamp was determined by subtracting the moment of inertia for the plastic plate from the moment of inertia for the clamp and the plate. For a more detailed description of trifilar pendulum testing of the upper clamp, refer to Appendix A.

For this study, measurement of flexural (transverse) and torsional vibration will be performed. *Figure 2.13* shows the microphone setup and corresponding impact that will be

used in each vibration mode. To ensure minimal interference of the flexural vibration mode on recording for torsional vibration, the chosen impact wing during torsional vibration was a wing that was 90 degrees from the recorded wing.

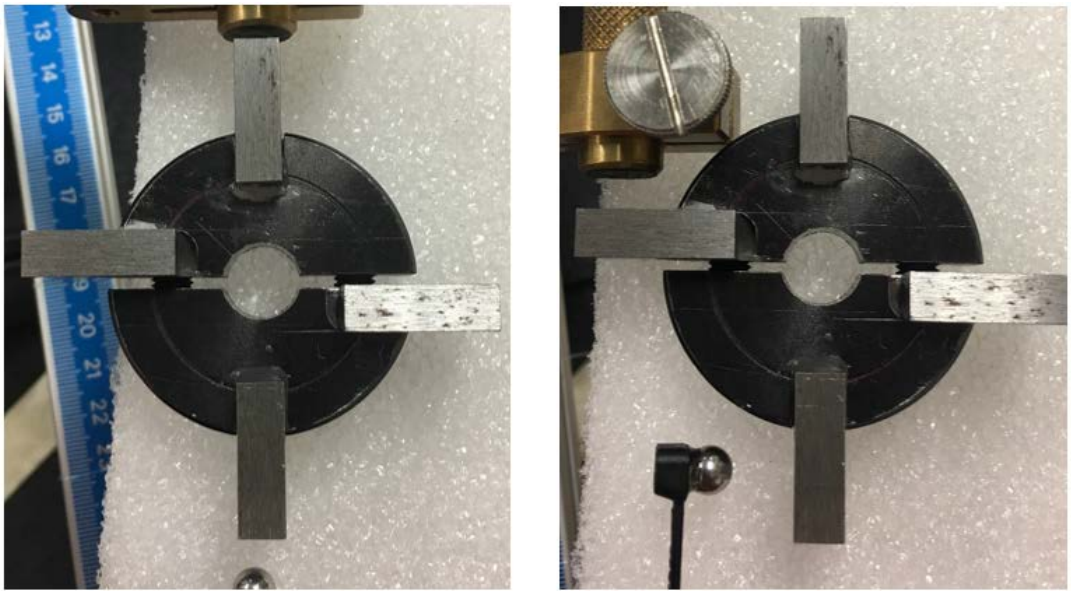

Figure 2.13: a (left): Flexural vibration microphone and impact setup. B (right): Torsional vibration microphone and impact setup

To ensure adequate support for the composite during IE testing, each bolt is tighten to a torque of 15 in-lbs. Once the sample has been set in the pressure rig assemble with the support clamps, removal of the clamps will not occur in order to ensure consistent IE measure throughout the testing. Prior to any internal pressure loading, a control IE test will be performed on the undamaged sample. Internal pressure will then be slowly increased to certain loading and then unloaded for IE testing. While the system is under no pressure, the telescopic adapter that connects to the upper end of the sample will be retracted to allow free vibrational movement of the tubular sample. The polymer bladder will not be in direct contact with the ID of the sample while the system is not pressurized and will, therefore, have no effect on the damping characteristics of the tubular sample.

2.6b Non-Rigid Support

An issue that must be understood is that fundamental beam flexural vibration equations assume supports for a cantilever beam (fixed-free configuration) are perfectly rigid. [46] Some of the earliest work on imperfect support rigidity was performed by Timoshenko. To further expand the fundamental Euler-Bernoulli motion and vibration equations, shear deformation and rotary inertia contributed a non-rigid support structure was included. The resulting computation indicated that a non-rigid elastic support affects the overall natural frequency of the measured beam. [65] MacBain and Genin utilized Timoshenko's work and derived a support flexibility coefficient for support integrated beams of prismatic cross-section. The resulting calculations led to an approximated bound on the support stiffness for non-rigid supports. In a later study, MacBain and Genin analyzed the effect of length to height ratio for similar prismatic beams on the fundamental frequency. Ultimately, MacBain and Genin developed a conservative approximation of the non-dimensional fundamental frequency for beams of flexible supports assuming simple cross-section and embedment to the support.

In a paper written later, Afolabi investigated the natural frequencies of turbine blades under similar conditions. Afolabi expanded on the work of MacBain and Genin calculating the true cantilever frequency from the lumped frequency incorporating the beam and the support, however, requires the computation of the shear deformation and rotary inertia of the non-rigid support. [66] In contrast to these mentioned studies, transitions to natural frequency and damping will be studied more so than accurate determination of material properties during pressure rig mounted impulse excitation. Normalized values of frequency will be investigated in flexural vibration mode to quantify

changes to moduli. This is due to the fact that moduli are functions of only material natural frequency under the same test conditions and sample geometry, as seen by previous equations.

2.7 Validation of Impulse Excitation

2.7a Table Mounted Impulse Excitation

Prior to testing of composite tubing via impulse excitation, it is necessary to validate the method on known material under different vibration modes. Various metallic materials of different cross-sections were tested using table mounted IE under free-free and longitudinal vibration. Equations from ASME standard 1876 in addition to equations from Timoshenko were used to calculate moduli for metal samples of strictly rectangular and rod shaped. Due to complexity, the moduli of all samples with tubular cross-sections will be determined by equations formulated by Timoshenko, mentioned previously. [46] Three test specimens were selected to validation IE. The specimens include a 6061 alloy Aluminum tube of .373” OD and .258” ID, a 6061 ally Aluminum bar of .500” width and .376” thickness, in addition to a .752” width and .250” thickness O1 alloy tool steel bar. All samples were cut to 6” with sharp, lightly rounded edges to avoid alterations to natural frequency. Comparison between equations derived by classical Timoshenko formulas and equations in ASTM standards will be made and tested for accuracy against published elastic moduli for the materials.

2.7b Pressure Rig Mounted Impulse Excitation

The second half of IE validation requires mounting round, tubular specimens onto the internal pressure rig similarly to how a composite sample would be. The same procedures would be followed including clamping torque and excitation configuration. The

tubing sample chosen to validate the pressure mounted system in the same .373" OD Aluminum tube used to validate the table mounted setup. For pressure rig mounted validation, special attention will be taken to the torsional frequency found. Torsional vibration of a tubular material will not be greatly impacted by non-rigid supports compared to flexural vibration of a beam with similar cross-section. [46] For torsional vibration tests, classical torsional vibration equations will be used to determine shear modulus of the metal validation specimen and compared to published data on the material. Beam length will be assumed to be from the exposed edge of the lower sample clamp to the center of the mass end clamp. The length of tube from the center of the mass clamp to the upper end of the tube is assumed to not contribute to the vibrational motion of the beam and as a result be lumped in with the moment of inertia of the mass clamp.

2.8 Instrumentation

Due to the variety of tests performed in this work, instrumentation will be different from test to test in regards to recording equipment. Impulse Excitation will be recorded IMCE companies Resonant Frequency and Damping Analyzing (RFDA) professional software that includes a 10-100k Hz microphone and automatic impulser. Due to lack of convenience, the automatic impulser was not utilized in this study. For all IE tests, the same microphone was used to gather vibration response signals.

As mentioned previously, the ADMET eXpert 2611 load frame with MTESTQuatto software with the default 8000N load cell was used during the tension tests. This tension tester has the capability to provide 10 volt excitation for strain gauge use. Strain gauges used in tension tests were CEA-06-062UW-350 strain gauges that were aligned along the axial axis of the tubular samples. The MTESTQuattro software is able to

record the load from the load cell in addition to the voltages from the strain gauges on the same time scale. Signal voltages from the strain gauges are recorded are non-specified values and require calibration to be accurately converted to strain readings. To do so, a Micro Measurements 1550B Strain Indicator Calibrator was used to simulate various strains on the strain gauge bridge connections. For the torsion tests performed in this study, a LSB302 FUTEK load cell was used that was powered by an Agilent E3611A adjustable DC power supply. Torsion strain gauges used were CEA-06-187UV-350 gauges. Both the strain gauges and the load cell voltages were recorded as parametric voltages on the Micro-II system from Mistras (Physical Acoustics).

Internal pressure tests were performed on an updated rig of the one used by Shapovalov and Alva. Pressure was recorded using an Omega Engineering PX01S0-20KGI pressure sensor while acoustic emission data was recorded using the Micro-II system from Mistras. All internal and external strain readings were recorded by strain gauges connected via the Micro-II system. External strain gauges were CEA-06-062UW-350 while the internal gauges used were CEA-06-062UB-350/P2. The CEA-06-062UB-350/P2 gauges are a unique strain gauge in which the measurement direction of displacement is 90 degrees from the typical axial direction of the gauge. Using this strain gauge to record internal tubing strains reduces the amount of space necessary to install the strain gauge. *Figure 2. 14,* shows an image of the strain gauge type used.

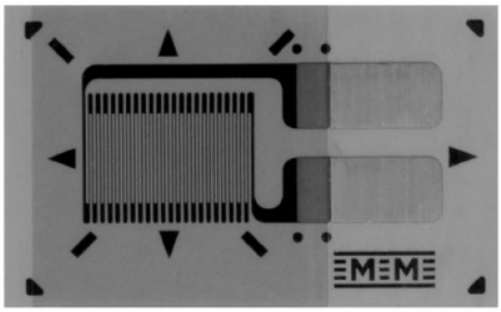

Figure 2. 14: CEA-06-062UB-350/P2 strain gauge used for internal strain measurement

Acoustic Emission data will be collected using the Micro-II system from Physical Acoustics. The sensors used for all AE testing was Nano-30 sensor. The sensor will be connected to a 2/4/6 pre-amplifier set for 20 dB. The sensor was coupled to the test specimen via 3M Scotch Weld 3776LM Hot Melt. This is a versatile hot melt that melts at a low temperature. This is ideal for attaching the sensor to the sample without damaging either. When sample tube ruptures, the sensor can be ejected and fall on hard surface. To protect ejected AE sensor from impact damage, an elastomer cradle was put on the sensor. The recording software was carefully set to record relevant high energy hits while at the same time, filtering out all low energy waveforms that could be identified as noise. The minimum amplitude threshold for relevant hits was set to 55 dB and the reference gain energy was set to 20 dB. As a result, Peak Definition Time (PDT), Hit Definition Time (HDT), and Hit Lockout Time (HLT) were all set to 50, 150, and 350 nanoseconds, respectively.

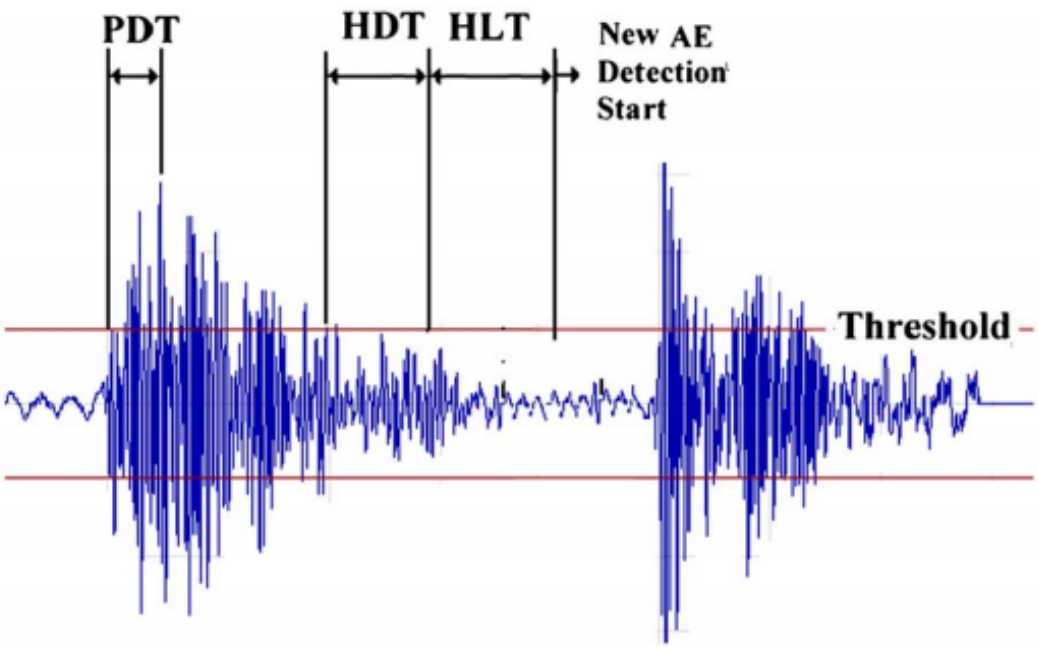

Figure 2. 15: Physical representation of AE timing parameters. [67]

These parameters also ensure that the system will not become oversaturated from the bulk signal collection. If the system becomes oversaturated with recorded AE activity, the system temporarily shuts down until all data has been processed. During that time, the system will not record any new information and will therefore be lost. The AE recording parameters were elected after previous experiments with similar material. The analog filter is set from 1 kHz to 1 MHz. Waveforms are recorded at a rate of 5 million per second with a 100 μs pre-trigger. The system's signal length was set to 3 kilobits. Further screening of signals was performed by setting a hit pre-filter to remove signals of counts 3 or less from the recorded data. All AE parameters were set similarly to those used by Alva and Shapovalov for easier comparison between data sets.

2.9 Internal Strain Gauge Study

2.9a Installation of Internal Strain Gauge

Prior to this study, there has been much investigation of the stress-strain relationship of SiC_f-SiC_m composite material under tensile stress. [3,17,18,19] Studies focusing on CMC tubing for nuclear fuel application primarily perform internal pressure tests for characterizing the composite behavior. This method of testing is of great importance considering that the fuel typically fails due to internal pressures during a Loss-of-Coolant Accident, however, during normal operations there are still external pressures acting on the fuel. Typical operating pressures for a pressurized water reactor are 16 MPa. Localized compressive stress can also result from bending and local contact. With these in mind, it is beneficial to investigate the strength of SiC_f-SiC_m composite tubing under compression via external pressure. To apply external pressure, a new test configuration was designed in which internal tubing strain could still be read. In addition, a second study was performed on tubing to validate accuracy of thick wall cylinder theory for estimating stresses along the inner surface of tubing under internal pressure. In this validation study, effects of various tubing curvature will be observed as well. For both studies, a procedure for installing an adequately small strain gauge along the inner surface of tubing was devised.

As mentioned, strain gauges chosen for internal strain gauge testing were the CEA-06-062UB-350/P2, which measure elongation in the lateral direction of the longer axis of the strain gauge. This characteristic provides ample space while adhering the strain gauge to the inner surface of the specimen tube. Prior to installation, Micro-Measurement 134-AWP single conductor leads were soldered to the gauge while leaving sufficient length to

be connected to recording hardware for testing. For most tests, the 134-AWP wires were soldered to a connector pad that was adhered to a rigid fixture or the outer surface of the specimen tube. Two soft rubber tubes were used to install the strain gauges into the various sized test tubes. The smallest rubber tube, with OD of .25" and ID of .125", was threaded over a 1/8" OD steel rod. The largest rubber tube had an OD of .375” and an ID of .25”. This large rubber tube was threaded over a .25” OD steel rod and was to be used for installing strain gauges into the largest samples for the validation study. Both the rods and the rubber tube were cut to be longer in length than the tubular specimen. A square of double sided tape, approximately 3/8" by 3/8" in size, was then attached to the center of the soft rubber tube with the steel rod pulled through to prevent the rubber tube from bending, *Figure 2 16 a.*

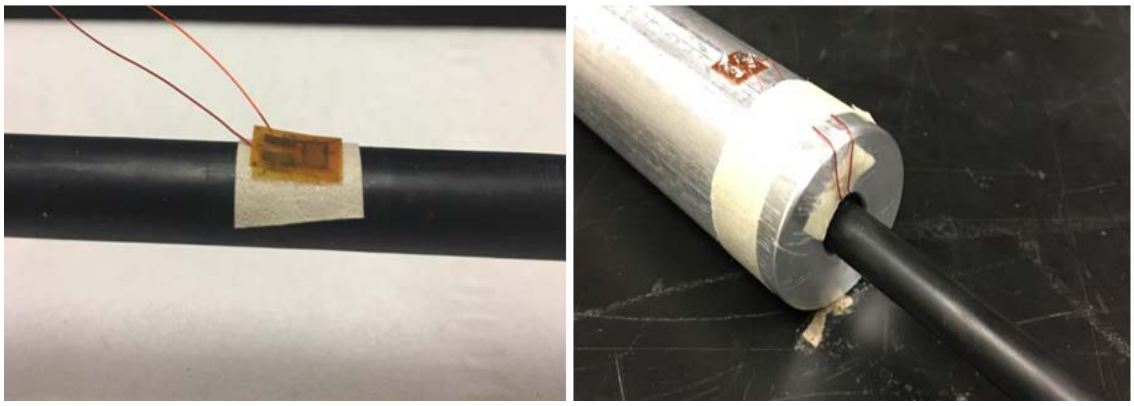

Figure 2 16: a (left): Attachment configuration of strain gauge prior to installation. b (right): Strain gauge lead attachment and support prior to rubber push tube removal

The purpose of the tape is to temporarily adhere the strain gauge to the rubber push tube while being inserted into the specimen tube. The strain gauge, with attached leads, was placed in the center of the tape with the measuring direction aligned in the hoop direction of the rubber tube. It should be noted that the strain gauge was applied to the double sided tape with the leads facing down. This was to permit the proper attachment of

the strain gauge to the inner surface of the tube after installation was complete. After the proper preparation of the inner surface of the specimen tube, M-Bond 200 catalyst solution by Micro-Measurements was applied along the inner surface at the location where the strain gauge was to be attached. The M-Bond 200 Adhesive was then applied to the exposed surface of the strain gauge. The rubber tube, with strain gauge attached, was then gently slid through the tubular specimen until strain gauge was over intended bonding location. With the specimen supported by hand, the steel rod and rubber tube were then manually pressed to allow the strain gauge to be compressed against the inner surface of the specimen tube.

After curing of the adhesive between the gauge and the sample, the rubber push tube can be easily debonded from the strain gauge without damaging the leads to the gauge. It was found that for larger ID specimen tubing, the smaller rubber push tube was inadequate for applying a distributed amount of force on the strain gauge while it cured. As a result, the larger OD rubber (.375") was used.

2.9b Mechanical Testing of Internally Attached Strain Gauges

The testing of internally attached strain gauges was divided into two different setups based on applied pressures. The first setup is for the application of external pressure upon composite tubing. To perform this function, a setup was designed similarly to an expanding polymer plug test. Traditional expanding plug tests have been performed on SiC_f-SiC_m composite tubing to simulate uniform internal pressure. [18] The expanding plug test involves applying axial loading to a polyurethane plug inserted into the sample tube.

The compression of the plug is treated like a hydraulic cylindrical piston and therefore it is assumed that the axial pressure is transmitted radially along the surface of the plug. This simulated internal pressure of the sample tube results in tension of the tubing along the hoop direction. The expanding plug test used in this study is different in the aspect that the simulated external pressure loads the sample under compression. This unique test characteristic has not previously been explored for composite material as greatly as tension.

The expanding plug method for external pressure utilizes a polyurethane cylinder plug with the sample tubing passed through the inside of the plug. A larger diameter containment cylinder then surrounds the polymer plug to restrict radial displacement. *Figure 2. 18*, shows a diagram outlining the test setup. The polymer plug was cut to have a sliding fit with the sample while the containment tube was cut to have a similar fit with the polymer plug. Similarly to expanding plug tests performed by Jacobsen, the polymer plug was cut shorter than the length of the sample tube. [18]

This would ensure that plug buckling would not occur and an even amount of pressure was distributed along the sample to polymer contact area. For SiC_f-SiC_m composite length of roughly 2.5", a plug length of 1.0" (25 mm) was used. The SiC_f-SiC_m composite tubing used for internal strain gauge studies had a different architecture than the tubing used in impulse excitation testing. *Figure 2. 17*, below, shows an image of the architecture used in compression tests. Aluminum support doughnuts were fabricated to the same diameters as the polymer plug and were cut to lengths of 3/8". These supports will help position the plug at the center of the sample tubing.

Figure 2. 17: Surface texture for 13444-13-SG-X SiC_f-SiC_m composite tubing

The upper and lower crossheads shown in *Figure 2. 18*, were designed so that they can be mounted on the ADMET eXpert 2611 load frame for the low load cycle of the composites. The lower crosshead was designed to support all tubing and to ensure only axial loading of the polymer plug was performed. The upper crosshead was designed with an OD and ID equal to the support doughnut. For both, the doughnut and the upper crosshead, the inner diameters were cut larger than the sample OD. During compression, the polymer plug expands radially both outwards against the containment tube and inwards towards the sample tube. This expansion is what simulates the pressure acting on the sample. *Figure 2. 19*, shows an image of the parts required for this test. For load to failure tests, an 810 Material Testing System (MTS) load frame was used since it has a higher load capacity.

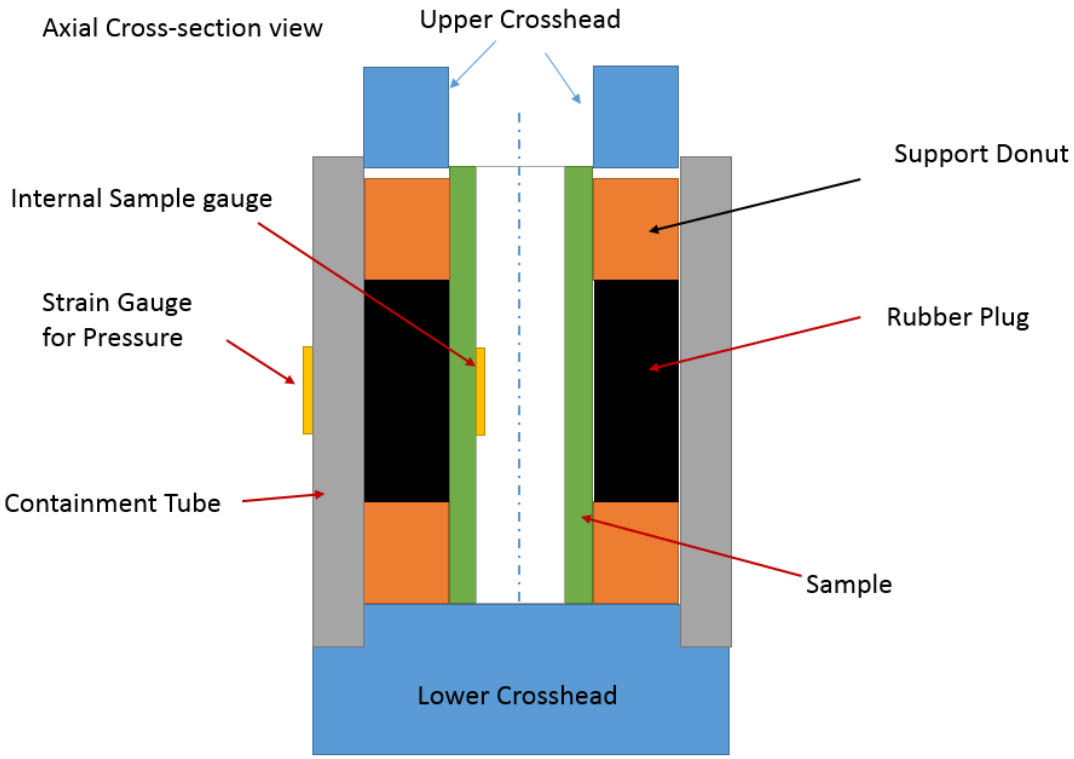

Figure 2. 18: Diagram for Expanding Plug test for external pressure

Two strain gauges will be used during this test, one placed along hoop direction on the inner surface of the sample tube, another placed along the hoop direction on the outer surface of the containment. The strain reading from the two gauges will be used to estimate the elastic moduli of the sample and the internal pressure generated by the polymer plug. The pressure estimated from the containment tube strain will be compared to the pressure estimated using the axial load from the compression test. This method of pressure approximation was used by Jacobsen for the expanding plug test for internal pressure. [18] Assuming the elastomer has a Poisson's ratio close to 0.5, it is expected that the pressure acting on the top surface of the rubber plug is equal to the pressure acting on its side surface

Figure 2. 19: Image of parts required for expanding plug test for external pressure

There were two cycles of external pressure tests performed on the SiC_f-SiC_m composite tubing. All three composite samples were initially loaded to a low axial force that would not deform the material above its elastic range. The purpose of this test is to ensure that the method is applicable to composite tubing. Finally, the second cycle was a loading to failure for each sample tube. The entire compressive stress-strain profile for this material can be observed. Acoustic emission will also be recorded during this load as well. Considering that direct AE sensor attachment to sample would be impossible, the sensor was attached to the lower crosshead of the expanding plug setup. In addition, hot melt adhesive was applied between the lower surface of the sample and the upper surface of the crosshead. This was to permit AE signals to be more easily acquired by the sensor. The first loading cycle was performed on an ADMET eXpert 2611 while for load cycles till sample failure, an 810 MTS load frame was used.

For the second setup testing the effect of internal tube curvature on recorded strain, the internal pressure rig was utilized. These internal pressure trials were performed at various pressure intervals to observe the effect of increased pressure against gauges bonded to concave curved surfaces. Many iterations of installation techniques were performed prior to the data presented in this study. This was to ensure that adequate strain gauge bonding was achieved. These trials were initially performed using aluminum tubes of varies diameters considering that the mechanical properties are well known.

These same installation techniques were used to install gauges into composite tubes, however, issues arose from the condition of the composite internal surface. Inherent limitations of the composite fabrication process cause significant roughness on the inner surface of architecture 13444-13-SG-X. Due to the rough inner surface of this tubing, internal strain reading during pressure tests were scattered and inconsistent. It was believed that as normal pressure directly applied to the foil strain gauges, the gauges would be forced to conform to the rugged composite surface and tend to indicate higher strain value. As a result, internal pressure tests while reading internal surface strains were not performed on composite tubing. Only aluminum samples were investigated for effects of curvature and pressure on internal strain readings.

2.10 Acoustic Emission Analysis

Acoustic Emission signal will be captured during mechanical testing of SiC_f-SiC_m composite tube. As mentioned previously, the use of AE has the capability to identify the damage of the structure and help determine proportional limit stress (PLS) for the material. Acoustic Emission analysis is a suitable method for ceramic composite material due to the unique damage modes of ceramics. Based upon previous work on AE analysis of CMC

materials, similar analysis will be performed during the mechanical testing of the composite fuel cladding, primarily the internal pressure testing. [17,60] Particular interest will be given to amplitude and absolute energy of hits that occur during testing. Changes to these parameters indicate a change to material structure and are indications to material damage.

CHAPTER 3: RESULTS AND DISCUSSION

3.1 Testing Overview

The following overview is to outline the course of testing that was performed for this research. As stated previously, this work was split into two separate studies: impulse excitation of SiC_f-SiC_m composite tubing and internal strain gauge study. For the impulse excitation study, validation tests were performed to ensure that mechanical testing of all samples yield accurate data. All mechanical validation tests were conducted on Aluminum tubing and yielded reasonable data within desired deviations. Afterwards, table mounted and pressure rig mounted impulse excitation tests were performed on various known materials. Moduli determined from these tests proved accurate, therefore, similar IE testing can be conducted on the CMC tubing. Three SiC_f-SiC_m composite tubes were used for this study. All tubular composite samples were initially tested using table mounted IE to determine axial Young's Moduli from the undamaged samples. Afterwards, the first tubular sample was further characterized via mechanical testing. Mechanical properties found for this sample would serve as a reference for the other samples which would each be loaded in increasing cycles of internal pressure. Flexure and torsional impulse excitation were recorded after every cycle to monitor the change of vibrational response.

For the internal strain gauge study, separate testing was performed for internal and external tube testing. Expanding plug testing for external pressure was performed on Steel tubing to validate the accuracy of this test. Afterwards, SiC_f-SiC_m composite tubing

architecture 13444-13-SG-X was tested to determine if thick wall cylinder theory applies to composites under compression. Afterwards, correlations between internal pressure, inner curvature, and percent error in hoop strain along the internal surfaces of Aluminum tubing were studied.

3.2 Tension Validation

Tension testing resulted in calculated values for Young's Modulus within 3% of moduli found in literature for Aluminum 6061. Literature indicated that the modulus was 68.9 GPa and the tension testing found it to be 70.7 GPa. *Figure 3.1*, below, shows the axial load and strain recorded during the validation tension test. Due to the low cross head displacement of the tension test machine, the pneumatic system moves in short steps rather than a smooth gradient over time and therefore produces the loading seen below. The error between the two figures is within an acceptable threshold therefore, it can be argued that the adapter nuts adhered to the ends of a tubular do not impact measurements of the axial Young's Modulus.

The configuration of the adapter nuts ensure that even if the adhesive between the adapter nuts and the sample were to debond or fail, accurate measurement of stresses and strains on the sample would take place. The recorded load produced by the tension test machine is exerted on all parts of the adapter system and the sample. In addition, through use of strain gauges, recorded strains are only of those on the surface that the gauge is bonded to, which is the sample only. Adequate validation of the tension test adapter configuration signifies that application to the tubular composite sample can be performed with guaranteed accuracy of data. Procedures for adapter nut installation onto the SiC_f-SiC_m composites will remain the same as with the Aluminum validation tube.

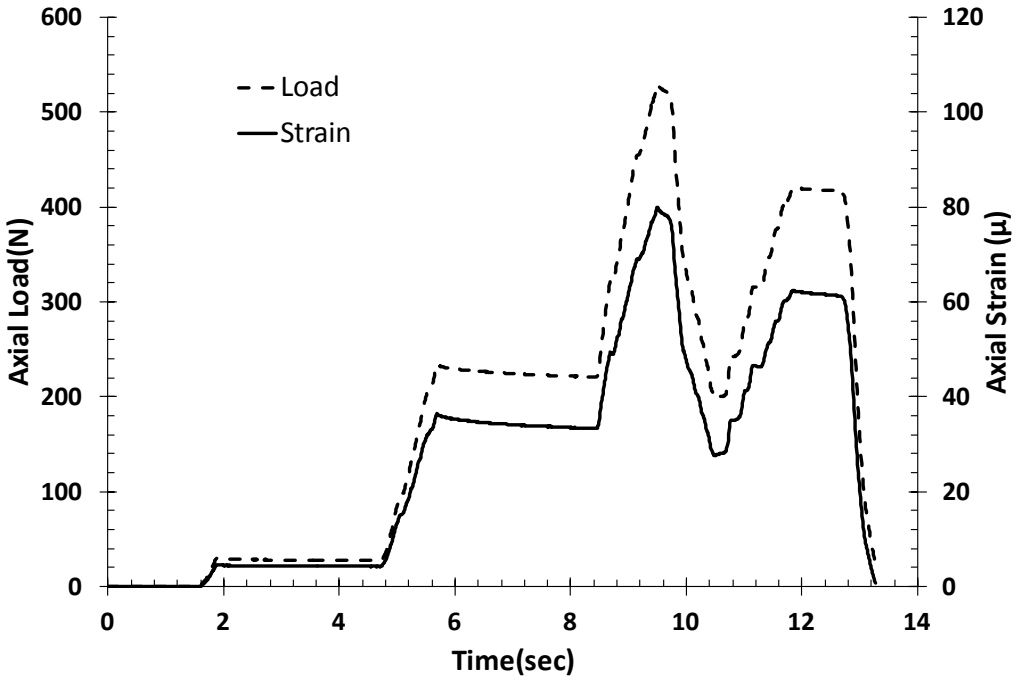

Figure 3. 1: Plot of load and strain during tension test of Aluminum 6061 tube

3.3 Torsion Validation

In a similar fashion, validation of the torsion rig resulted in accurate data compared to published moduli of the same Aluminum 6061 tube used for the tension test validation. Torsion of the sample resulted in Shear modulus of 27.0 GPa while published literature of this material indicate a value of 26.0 GPa. The percent error between the two values is less than 4% and validates the accuracy of the torsion rig for testing. *Figure 3.2*, below, depicts the calculated shear stress and strain recorded from the manually induced torsion test. The test was manually performed in order to produce a constant increase of stress to the sample at low torque. From previous testing involving a linear step motor to generate torque of the sample, desired maximum loads were quickly exceeded. The primary purpose of the tension and torsion tests are not to damage the sample in any way. The tests are to simply determine elastic and shear moduli of the material at low loads.

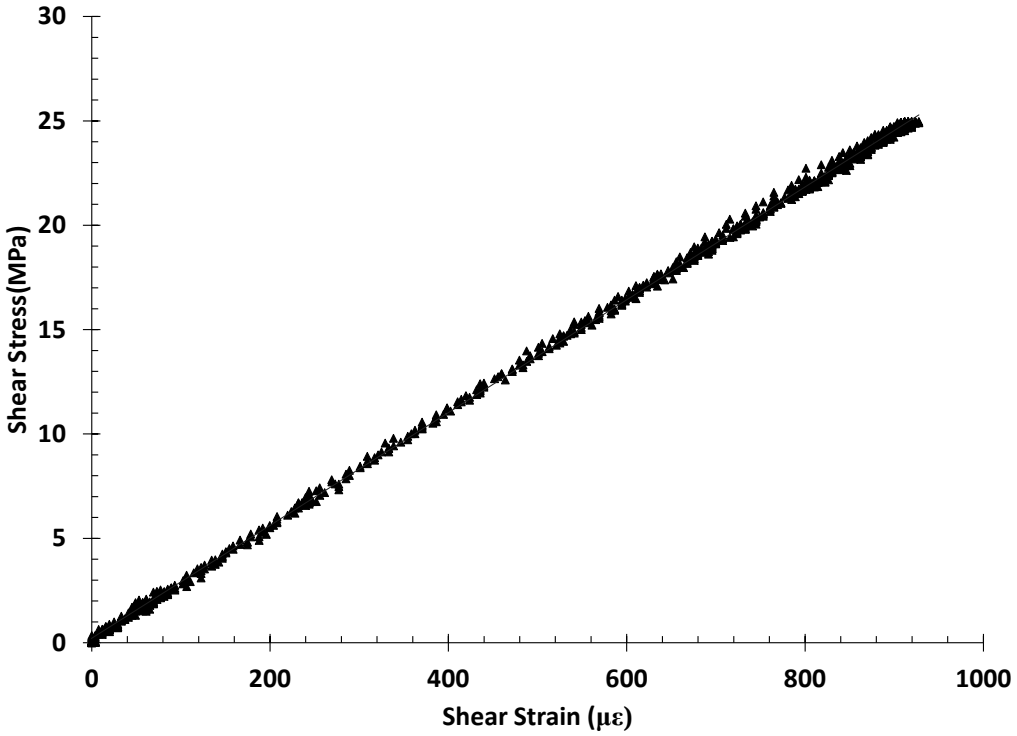

Figure 3.2: Shear stress-strain plot of Aluminum 6061 torsion

3.4 Internal Pressure Validation

Validation of the internal pressure rig was performed previously by Shapovalov in which testing of aluminum tubing yielded accurate results compared to published values. Shapovalov tested a short tube of aluminum with four strain gauges attached, two in the hoop and two in the axial directions. It was found that calculated Young's Modulus and Poisson's Ratio for the sample came within 4% of published values. It was also determined that the differences between circumferential strain gauges was les then 5% at elevated pressures. [17] This indicates uniformity in the internal bladder deformation around the inside of the sample and an even amount of pressure is exerted along the inside of the sample during loading. At lower pressures, Shapovalov observed that percent error in strain readings was higher, however, this was due to the initial expansion of the polymer bladder until contact with the inner surface of the tubing. To ensure proper validation of the internal

pressure rig, a pressure test was performed on a 6061 Aluminum alloy tubular sample of .501" and .306" OD and ID, respectively. It was found that OD hoop strain levels remained within 4% of strains projected by induced pressure. In addition, Young's Modulus for the 6061 Aluminum sample was calculated to be 69.5 GPa came within 3% of published modulus.

Shapovalov also validated uniformity of internal pressure applied throughout the length of the sample. The aluminum tube of 304 mm with strain gauges attached along the hoop direction of the tube at locations 50.8, 152.4, and 254 mm yielded less than 3% strain differences between all three gauges. This finding is significant for this study considering that a generally long, ~150 mm, composite tube will be tested. The pressure uniformity study performed by Shapovalov assures that the damage due to internal pressure to the composite samples will be uniform.

3.5 Table Mounted IE Validation

Validation of table mounted IE was performed on four separate specimens of various material and cross-section. The materials, seen in *Figure 3.3*, was an Aluminum 2024 tube, Zircaloy-4 tube, Aluminum 6061 rectangular bar, and a O1 tool steel bar. Approximately 6" of each material was cut for the IE validation. For this validation, two sets of comparisons were made. The first comparison will be between determined moduli from free-free and longitudinal vibration modes by equations used for general material cross-section and those found using the standard equations from ASTM E1876 for the rectangular cross-sectioned bars. This comparison will determine whether the alternative equations for vibration analysis are accurate for complex material geometry and can therefore be used to properly characterize tubular samples. The second comparison will be

between the alternative equations for all specimens and moduli found from published sources.

Figure 3.3: Materials used to validate table mounted impulse excitation. (Left to right) Al 2024Tube, Zircaloy-4 Tube, Al 6061 Bar, and O1 Tool Steel Bar

Table 3.1, below, indicates the calculated values of Young's Modulus for each of the specimens based upon the method and equations used. It can be seen that all values of Young's Modulus found using the Alternative free-free equations came within 5% of published values. The Alternative longitudinal equations yielded closer values, less than 2%, for the Young's Moduli of the specimens. This is understandable considering that the Alternative longitudinal equations are less sensitive to changes in length measurements than the free-free equation. In general, free-free data showed to be lower than the published data while the longitudinal data tended to be at or slightly above the published moduli values. This is as well is believed to be due to the sensitivity in the accuracy of geometric measurements.

Young's Moduli determined using the ASTM standard equations for the Aluminum and steel bars came within 2% of published values. This clearly indicates that the use of impulse excitation in determining moduli of simple geometric bars is an accurate and powerful tool for non-destructive evaluation. Considering that all percent errors from the Alternative equations are within an acceptable threshold, 5%, the alternative free-free and

longitudinal equations will be used for table mounted IE testing of the SiC_f-SiC_m composite tubing.

Table 3. 1: Results from Table Mounted IE validation testing. Percent errors are in regards to values from published literature.

Specimen	Published Young's Modulus (GPa)	Alternative Free-Free (GPA)	% error	Alternative Longitudinal (GPa)	% error	ASTM Free-Free (GPa)	% error	ASTM Longitudinal (GPa)	% error
Al 2024 Tube	73.1	71.0	2.8	74.1	1.4	-	-	-	-
Al 6061 Bar	68.9	66.1	4.0	68.5	0.6	68.1	1.1	68.5	0.6
O1 Tool Steel Bar	214	214.5	0.2	216.4	1.1	217.2	1.5	216.6	1.2
Zircaloy-4 Tube	99.3	95.0	4.4	99.2	0.1	-	-	-	-

3.6 Pressure Rig Mounted IE Validation

Prior to IE testing of the CMC tubing, flexure and torsional vibration validation was confirmed through the use of four circular cross-sectioned materials mounted on the pressure rig. The validation specimens, shown below in *Figure 3.4*, were a 6061 Aluminum rod, 3003 Aluminum tube, 4140 Steel rod, and 4140 Steel tube. Each specimen was mounted to the pressure rig via the lower support clamp and the upper torsion mass and tested for Young's Modulus by flexure vibration and Shear Modulus by torsional vibration. To provide a more accurate frequency reading, torque applied to the clamps were set to 25 lb-in. as opposed to the 12.5 lb-in designated for the torque set for the composite tubing. The composite tubing is brittle under compressive loading and would become damaged under higher levels of torque. The greater support clamp torque will provide a more rigid

support fixture for the vibration of the validation specimens and will therefore yield more accurate moduli determined by impulse excitation. [66]

Figure 3.4: Materials used to validate rig mounted impulse excitation. (Left to right) Al 6061 Rod, Al 3003 Tube, 4140 Steel Rod, and 4140 Steel Tube.

The result of rig mounted validation testing can be seen in *Table 3.2*. The Young's Moduli determined by flexure vibration (cantilever) seemed to be more accurate for the Aluminum samples than for the Steel samples. Percent error for the Aluminum Young's Moduli came within 4% of published values as opposed to the 8 to 18 % error for the steel specimens. MacBain noted that differences in support elasticity would result in variations in support structure rigidity and therefore the observed frequency of the system vibration. [65] The horizontal support brackets are made of Aluminum and are presumed to affect the rigidity of the support structure. From the differences in error between the Aluminum and Steel samples, this seems to be the case. The greater amount of error in the steel samples is a result of the support structure compliance, including the horizontal brackets, being less rigid than the steel specimens. For the Torsion IE tests, percent errors were much less than those for flexure IE tests. For all torsion IE tests, determined Shear Moduli came within 6% of published values which indicates a lesser sensitivity to support elasticity compared to flexure vibration.

These validation results indicate that using IE testing in flexure and torsional modes can yield accurate Young's and Shear Moduli for material similar in elasticity to the support structure. Unfortunately, for more rigid specimens, flexure and torsional vibration analysis tends to become more inaccurate. As a result, direct monitoring of moduli with increased material damage will not be performed in this study, however, degradation of material natural frequency will be monitored. As seen by Brebels and Bemis decreases in natural frequency and increases to material damping, indicate material damage in composites. [44,66]

Table 3. 2: Results from Rig Mounted IE validation testing. Percent errors are in regards to values from published literature.

Specimen	Published E (GPa)	Published G (GPa)	Flexure E (GPa)	% error	Torsion G (GPa)	% error
3003 Al Tube	68.9	26.2	71.3	3.5	25.8	1.5
6061 Al Rod	68.9	26.0	68.4	0.8	24.4	6.0
4140 Steel Tube	200.0	80.0	182.9	8.6	78.6	1.7
4140 Steel Rod	200.0	80.0	165.7	17.2	75.4	5.8

3.7 Initial Table Mounted Impulse Excitation

Prior to any mechanical testing of the SiC_f-SiC_m composite tubing samples, table mounted impulse excitation was performed to determine initial moduli of the composites. *Table 3.3*, below, shows that resulting Elastic Moduli determined by table mounted IE tests. All tests were conducted identically to those performed on the metallic validation samples in previous study sections.

Resulting Elastic Moduli determined were all calculated using the Alternative equations. Average values for Young's Modulus between both vibration modes was 110.0 GPa with a standard deviation of 3.5 GPa. Values for Elastic Modulus found by both modes of vibration for sample 2 appear to be noticeably lower than the other samples. This is believed to be due to a variation in manufacturing or from a manufacturing defect considering that measured OD and ID of all samples were consistent. This lower value of modulus may also be the result of minute material damage prior to or during shipment from the manufacturer. These values for sample 2 and 3 will later be compared with Young's Moduli found via table mounted IE after the tubing samples had been internal pressurized. The pressure loadings are expected to damage the ceramic composites and will therefore result in a decrease in recorded Young's Modulus.

Table 3. 3: Results from Rig Mounted IE composite testing.

SiC_f-SiC_m Sample	Table Mounted Vibration Mode	Axial Young's Modulus-Alternative Equations(GPa)
13464-17-06-01	Free-Free	110.4
	Longitudinal	113.4
13464-17-06-02	Free-Free	104.5
	Longitudinal	106.1
13464-17-06-03	Free-Free	111.8
	Longitudinal	113.4

3.8 Sample 13464-17-06-1 Mechanical Testing

3.8a Tension

Initial sample mechanical testing is needed to establish an understanding of the mechanical properties of the SiC_f-SiC_m composite architecture. Due to the great variety in architecture design for composite tubing, it is irresponsible to assume set moduli values for

this material solely based upon the material. Any slight change in tubing design or material can result in a massive change in material strengths. After initial table mounted impulse excitation, sample 13464-17-06-01 (or simply sample 1) was prepared for mechanical testing beginning with tension and torsion testing under low loads followed by internal pressure testing until tubing burst.

Adapter nuts were fabricated and adhered to each end of sample 1. Two linear strain gauges and one shear strain gauge were attached prior to tension and torsion testing. Using the ADMET tension system mentioned previously, Sample 1 was loaded to 400 N with axial strains recorded. *Figure 3.5*, below, indicates the stress-strain relationship for the tension test. The Young's Modulus calculated based upon the recorded data was 109.7 GPa along the axial direction of the SiC_f-SiC_m tube. This value comes within 2% of the average Young's Modulus found between the Free-Free and Longitudinal vibration modes using IE for this sample.

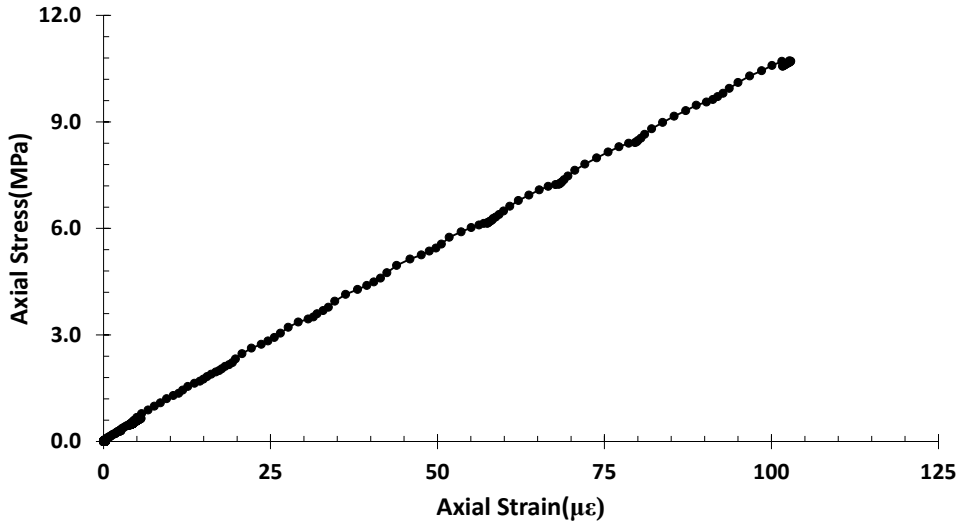

Figure 3.5: Stress-Strain plot of tension test performed on Initial SiC_f-SiC_m composite sample 13464-17-06-01

3.8b Torsion

After sample had been mechanically tested under tension, the sample was placed in the torsion rig to determine its Shear Modulus. To ensure no damage to the composite specimen would the maximum shear stress that the composite tubes will be allowed to experience during torsion tests will be 32.1 MPa. This is well within expected elastic range for this material without causing significant material cracking. To aid in monitoring of structural damage during mechanical tension and torsion testing, acoustic emission was recorded. During all tests for sample 13464-17-06-1 under the previously mentioned parameters, a negligible number of AE hits were recorded per test (less than 100 hits). As mentioned in previous sections, the adapter nuts adhered to the end of the sample are compatible with the torsion rig and therefore make testing more time efficient. Sample 1, was manually loaded on the torsion rig with the load recorded by the load cell, and the strains recorded via the Micro-II system as parametric voltages. A priority during loading was to avoid any drastic changes to load that could potentially damage the sample or the exposed strain gauges. The stress-strain plot for this torsion test, seen in *Figure 3.6*, shows a linear correlation between the shear stress and shear strain of the composite specimen. Shear Modulus of this specimen was 51.6 GPa based upon the data recorded during torsion.

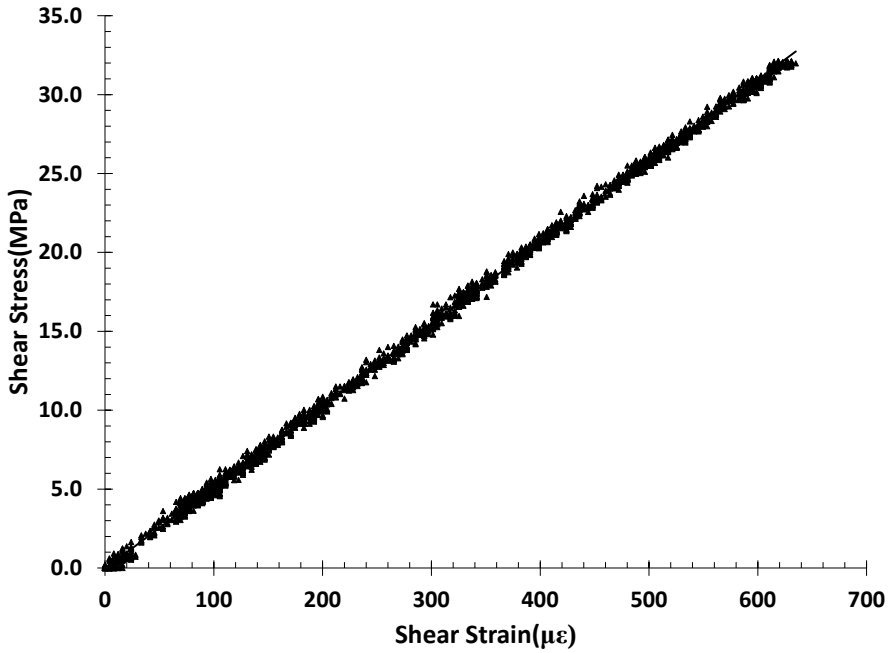

Figure 3.6: Shear Stress-Strain plot of sample 13464-17-06-1 torsion test

3.8c Internal Pressure

Internal pressure testing provides excellent characterization of a tubing sample by determining the material's Modulus of Elasticity along the hoop direction of the tube. Internal pressure testing will be performed on all three composite samples and have recorded stress, strains, and moduli compared to other publications dealing with similar testing. Due to the few number of available samples, it is advantageous to conduct as many tests of a specimen as possible before completely damaging it beyond adequate testing condition. As such, internal burst testing must be conducted last in the line of mechanical testing. In order to perform internal pressure testing on sample 13464-17-06-1, it is required that the adapter nuts and the sample be separated. Since heating the adapter nuts and the sample to sufficient adhesive melting temperatures would potentially damage the integrity of the composite tube, it was elected that the inner most section of the tube be cut away. Sample 1 was cuts using a South Bay Technology Model 650 Low Speed Diamond Wheel

Saw and 4" diamond wheel. *Figure 3.7,* shows the cuts made to the sample in preparation of burst testing. The cuts were made at 90° of the composite tube's axis. The length of the center piece to be used in burst testing was 31.75 mm, which is comparable to lengths of SiC_f-SiC_m composite tubes tested by Shapovalov in similar burst testing. Similarly sized sections will be cut from the remaining two samples for burst testing after all other testing on those samples is completed.

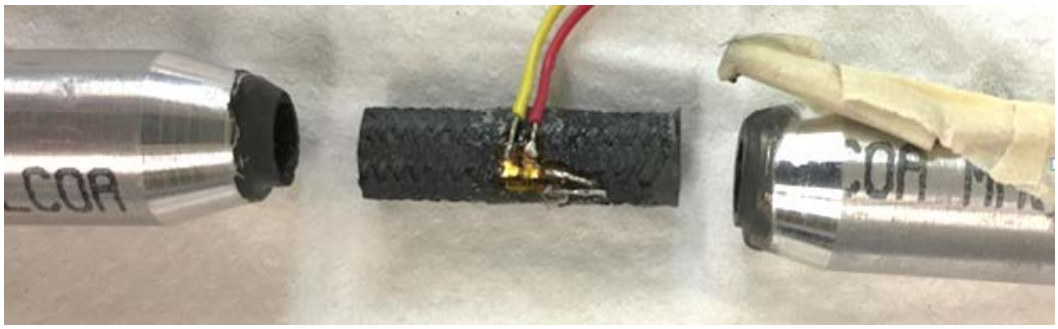

Figure 3.7: Cut section of sample 13464-17-06-1 used for internal burst testing

Sample 13464-17-06-1 was loaded via internal pressure and ruptured at approximately 8.52 ksi with a Proportional Limit Stress (PLS) occurring roughly between 3.5 and 3.7 ksi. Nozawa and Shapovalov indicated that PLS for ceramic composite material could consistently be determined when the highest Absolute Energy in AE events occurred. [17,19] In addition, it was seen that a rapid densification of high amplitude and energy AE events occurred shortly before or at PLS. Based upon these characteristics, PLS for SiC_f-SiC_m composite sample 13464-17-06-1 was predicted. This PLS was confirmed by the stress-strain curve for this sample. .*Figure 3.8,* below, outlines the predicted PLS for the sample. After 3.5ksi, the number of AE events with Absolute Energy of 1.0E6 aJ significantly increases similarly found with Nozawa and Shapovalov. [17,19]

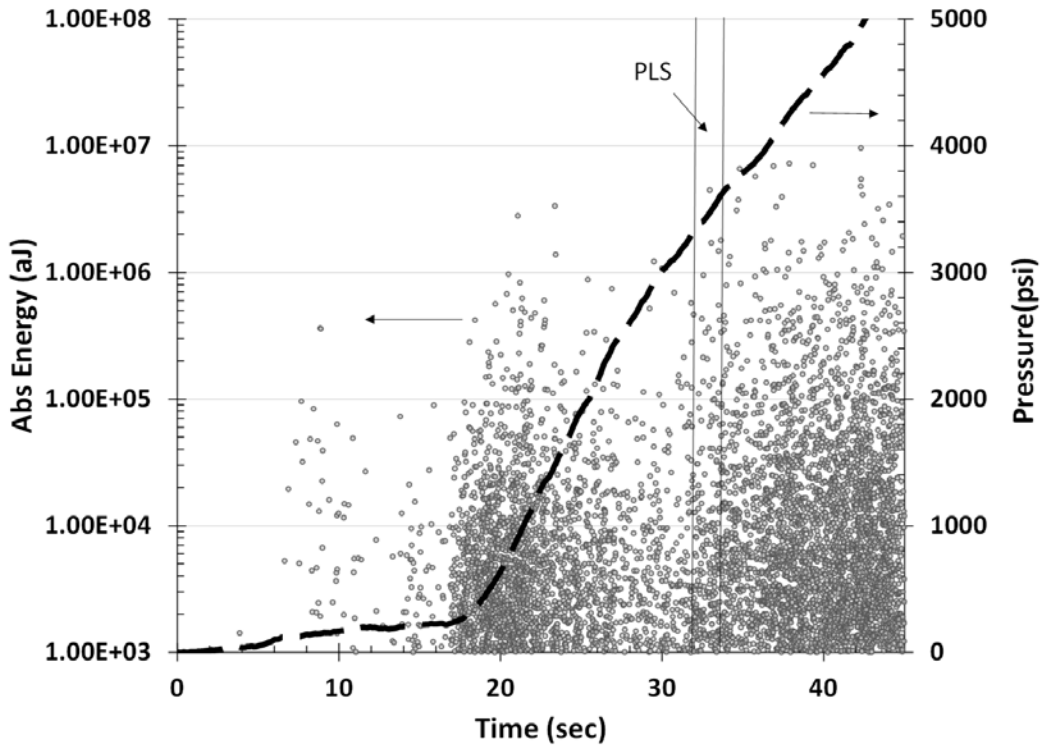

Figure 3.8: AE Absolute Energy and pressure found in burst test of sample 13464-17-06-1

The recorded pressure and hoop strain indicate that the tubular specimen has a Young's Modulus of 120.4 GPa along the hoop direction of the sample. This value, at first, was considered to be particularly low compared to other CVI produced SiC_f-SiC_m composite tubing studies. Maximum UTS calculated for the external face of sample 1 was found to be 58.7 MPa while the UTS for SiC_f-SiC_m composite tubes found by Jacobsen and Shapovalov were approximately 400 and 370 MPa, respectively. [17,18] In addition, the tubing tested using the same internal pressure method by Shapovalov burst at pressures close to 14 ksi. [17] Both points suggest that the 6" composite tubing used in this study are composed of a much weaker architecture. Let it be noted that mechanical properties, such as moduli and strength, are architecture dependent. To clarify, the architectures tested in this work were different than work performed by Shapovalov.

3.9 Samples 13464-17-06-2 and 3 Pressure Loading and IE testing

3.9a Pressure Loading

As mentioned, sample 2 and 3 were to be systematically loaded internally while recording impulse excitation after every pressure loading. A control IE test was conducted prior to internal pressure loading on each sample. The purpose is to monitor the change of specimen frequency and damping with increasing amount of composite damage. In addition, acoustic emission responses were recorded to aid in determination of PLS for each sample. Based upon pressure testing and corresponding AE data recorded for sample 1, PLS for this composite architecture is expected to fall within 3.5 and 3.7 ksi internal pressure. To ensure adequate capture of data, loading of samples 2 and 3 were conducted to beyond this expected range. A total of six loadings were conducted per sample; these loadings were to 1 ksi, 2 ksi, 3 ksi, 3.5 ksi, 4 ksi, and 4.25 ksi of internal pressure. *Figure 3.9 and Figure 3.10* show the pressure loadings and AE data recorded for sample 2 and 3, respectively.

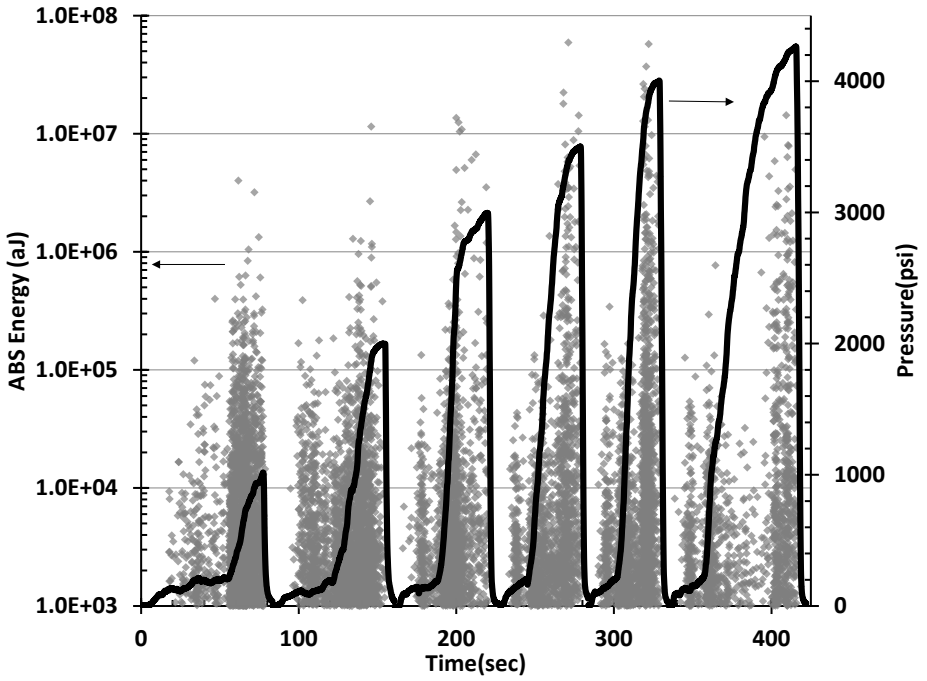

Figure 3.9: Pressure loading for internal damage to sample 13464-17-06-2 with recorded AE events

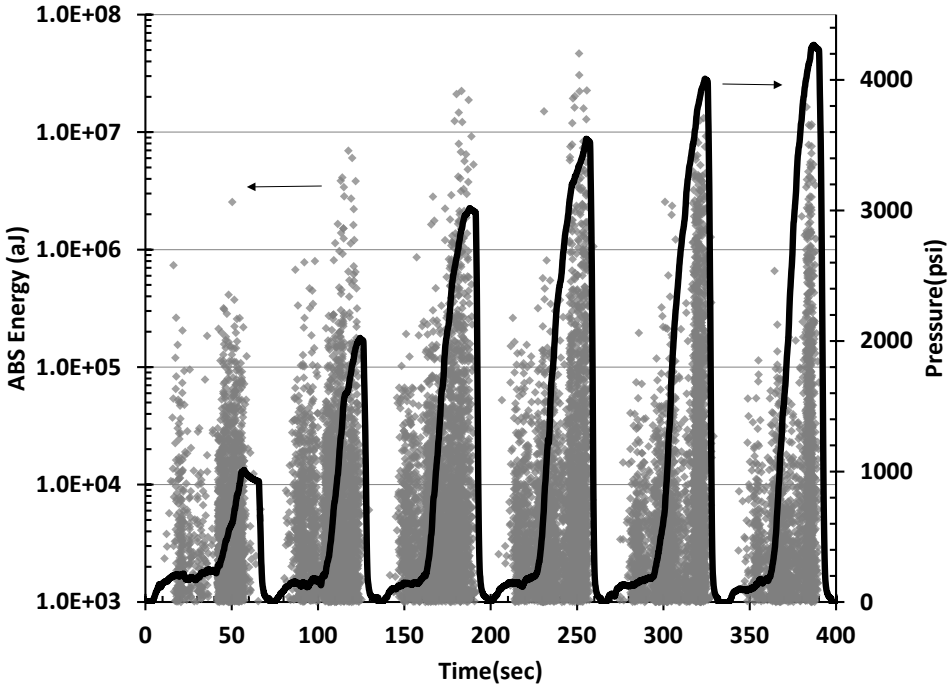

Figure 3.10: Pressure loading for internal damage to sample 13464-17-06-3 with recorded AE events

It can be seen that for both sample 2 and 3, the loading that experienced the event with the greatest absolute energy was the 3.5 ksi loading. For each sample, the greatest energy event occurred at approximately 3.4 ksi which is comparable to the greatest energy event observed in sample 1. This indicates that the initial prediction of PLS range between 3.5 to 3.7 ksi was slightly greater yet still close. In *Figure 3.9*, the loading to 4 ksi for sample 2 shows a large density of events with high absolute energy at 3.7 ksi. A similar AE behavior was noted by Morscher and Shapovalov in which the AE activity rate shortly increased at PLS followed by a significant attenuation of acoustic energy for ceramic composites. [17,31] This signal attenuation can be seen in the last two loadings for both sample 2 and 3. The observations stated provide sufficient evidence to conclude that both SiC_f-SiC_m composite samples have surpassed PLS.

Samples 2 and 3 were then mechanically tested via tension, torsion, and internal burst tests. *Table 3.4*, below, indicates the tabulated results of all mechanical tests performed on the SiC_f-SiC_m composite samples. Hoop Modulus found for all samples seem to be in the same range of variation compared to variation in observed by Shapovalov. For a much larger number of samples tested, Shapovalov observed a range of 65 GPa between the upper and lower Hoop Moduli values recorded. It can be seen by the table that both samples 2 and 3 had lower axial Young's and Shear Moduli compared to sample 1 which had not been internal loaded. In addition, the burst pressures for samples 2 and 3 are noticeably lower than sample 1.

Table 3. 4: Tabulated results of mechanical tests for all composite samples

	Tension Test	Torsion Test	Internal Burst Test	
13464-17-06-X	Axial Young's Mod. (GPa)	Shear Mod. (GPa)	Hoop Young's Mod. (GPa)	Burst Pressure(MPa)
1	109.7	51.6	120.4	58.8
2	98.6	49.3	154	50.9
3	105.7	49.7	175.6	54.8

3.9b IE Testing

Impulse excitation tests were performed after every pressure loading indicate clear changes to recorded natural frequency and damping for each composite sample. As mentioned previously, IE testing was performed via IMCE Inc. Resonant Frequency and Damping Analysis software. The software separates all incoming frequencies using a Fast Fourier Transform and identifies the frequency with the highest amplitude. This high amplitude frequency is the natural frequency for the sample depending on the mode of vibration of the sample. As seen in validation testing for IE, these natural frequencies are highly repeatable between multiple tests. *Figure 3.11* and *Figure 3.12*, show plots of these changes for sample 2 and 3, respectively. For simplicity, each plot shows that normalized values of frequency compared to initial frequency recorded during the control test prior to internal pressure. For both figures, data points marked with squares are data corresponding to torsion IE testing and the data points marked with triangles correspond to flexure IE testing. In addition, solid lines indicate normalized frequency data while dashed lines indicate damping data.

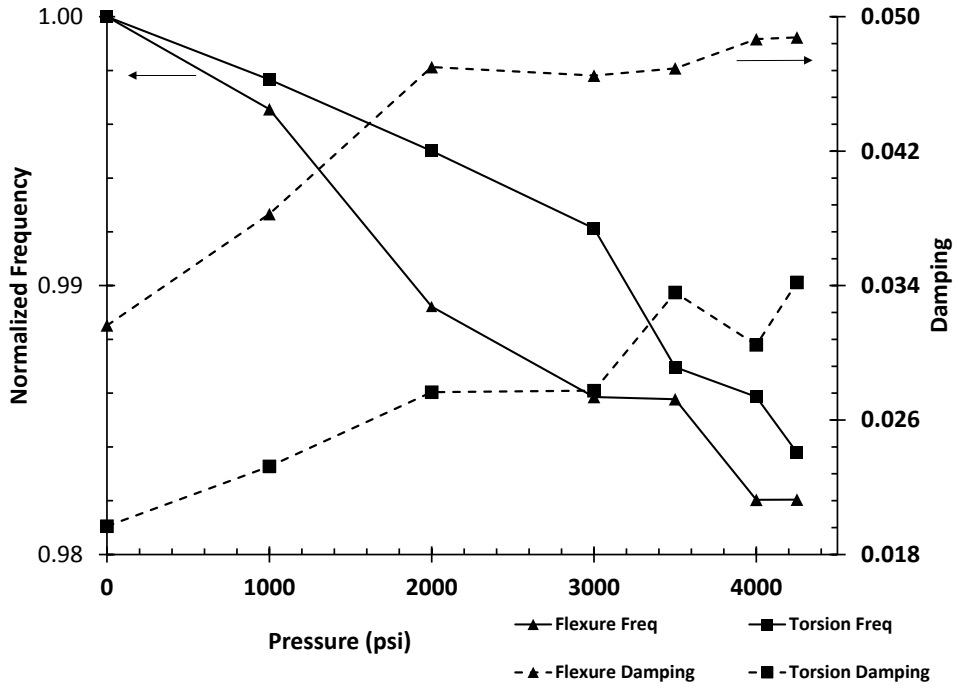

Figure 3.11: Resulting frequency and damping changes of sample 13464-17-06-2 with increases to internal pressure

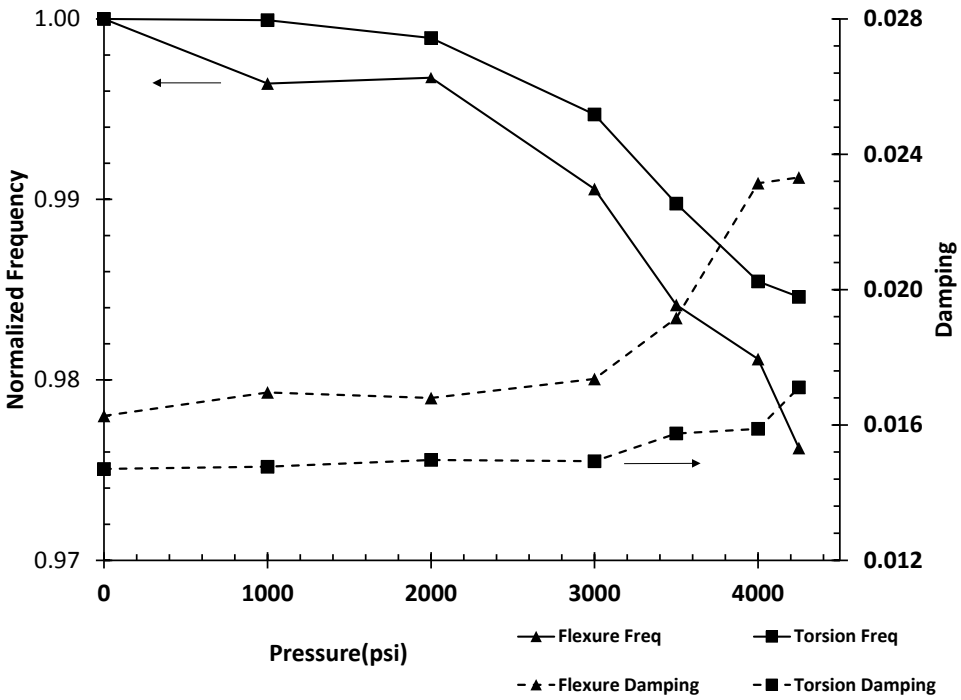

Figure 3.12: Resulting frequency and damping changes of sample 13464-17-06-3 with increases to internal pressure

From both plots, the general trend, for flexure and torsion data, is that the frequency decreases while damping increases with greater application of internal pressure. In addition, it can be seen that flexure frequency changes occur more rapidly than for specimen natural frequency under torsional vibration. Flexure damping also tends to be greater throughout the testing process for both samples. As greater stresses are achieved along the inner surface of the tubing from the increasing pressure, the saturation of matrix-cracking becomes more prevalent in the material. After these tests, it is difficult to identify a clear correlation between fiber architecture and vibrational response. Wang determined that the natural frequency of a composite beam would vary depending on the fiber direction of the composite. [69] It was found that beams with 0^o and 90^o degree fiber orientations from the axial direction showed the greatest degradation of beam frequency while close to 60^o fiber orientation showed the smaller gradient of frequency as material cracking increased. Wang also found the first mode of bending vibration for composite beams was more affected by increases to crack development compared to the first mode of torsional vibration. A similar conclusion cannot be drawn from these few tests considering the complex fiber architecture of these tubes.

The Proportional Limit Stress (PLS) of a composite indicates the significant generation of micro-cracking in the material and therefore affects the material stiffness. [18,19 ,60] Changes to material stiffness ultimately cause a change in material elastic moduli which has been observed in frequency changes. [36,40] Hu suggests that the monitoring of frequency change via impulse excitation can therefore determine PLS for a composite material. [63] From the limited data presented here, it is difficult to draw this conclusion, however, the consistent degradation of recorded frequencies with increases to

material damage shows potential for future work. The greatest percent change in recorded frequency from IE tests on both samples is less than 2%. This is a reasonable figure considering that PLS was only exceeded by a small amount and corresponding stiffness change would be small. Due to the great variation in composite strength from sample to sample, care was taken not to risk bursting the samples during pressure loading and IE testing. Should future investigation be performed, it would be recommended to not only increase the total number of samples tested in this configuration, but to also increase the number of loadings to higher internal pressures.

Table 3.5 shows the resulting moduli determined by impulse excitation for the SiC_f-SiC_m composite cladding. For samples 2 and 3, it can be seen that both free-free and longitudinal IE tests indicate a decrease in axial Young's Modulus after pressure loading. This correlates well with the degradation of flexure and torsional frequency as internal pressure loading increases. The initial Shear Modulus recorded in the table is the modulus found for samples 2 and 3 prior to pressure loading. The average Shear Modulus for samples 2 and 3 post loading is 49.9 GPa and comes within 1% of values found through torsion testing.

Damping, or internal friction, of the samples increase with the increase to internal pressure and resulting matrix cracking. As seen in previous vibration analysis work performed on ceramic material, the micro-cracking of a material generates friction along the crack surface and therefore dissipates the vibrational energy of the specimen. Although the flexure and torsional damping observed in sample 2 increase with internal pressure, the recorded values show a generalized linear trend. The damping seen in sample 3 shows a more exponential increase in damping in which the greatest increases to damping between

loadings is apparent near the predicted PLS occurring around 3.5 ksi internal pressure. Although not many IE studies on mechanically damaged composites have been performed similarly to this work, much study has been conducted in regards to damping change on thermally tested ceramics. Roebben noticed a similar exponential increase in damping during high temperature testing of Si_3N_4 ceramics. Little change in damping and frequency were observed at temperatures lower than 1200^0 K, however, at higher temperatures, damping quickly escalated as ceramic failure temperatures were achieved. Roebben indicated that this was due to an amorphous intergranular phase that softens at high temperatures and ultimately deforms the ceramic micro-structure. [44,58] Bemis noted similar characteristics in impulse excitation of thermally shocked monolithic SiC rings. These ceramic rings would be heated to high temperatures and then quickly quenched. With added cycles of this thermal shock, more microscopic and visible cracking formed which drastically increased recorded internal friction values for the ring specimen. [44]

To conclude, IE testing and analysis of SiC_f-SiC_m composite tubular fuel proves to be a reliable and accurate method for composite structural health monitoring and mechanical characterization. Despite the limited number of testing samples, a clear correlation between material integrity and vibrational motion can be seen. These findings prove to be consistent with other IE work performed in the industry. More confidence in the trends noted in this study can be acquired through the testing of more material with similar characteristics.

Table 3. 5: Resulting Moduli from Impulse Excitation testing

	Table IE (Initial)		Table IE (Post Loading)		Rig Mounted IE (Torsional)	
	Free-Free	Longitudinal	Free-Free	Longitudinal	Initial	Post Loading
Sample	Axial Young's Mod. (GPa)				Shear Mod. (GPa)	
1	110.4	113.4	-	-	-	-
2	104.5	106.1	103.5	105.1	48.0	46.5
3	111.8	113.4	109.4	111.0	54.1	53.3

3.10 Compression and Internal Strain Gauge Study

3.10a Validation of Expanding Plug test for External Pressure

After much experimentation with strain gauge installation procedures, bonding adhesive, and testing pressures, a consistent method was developed to adequately install strain gauges along the internal surface of a specimen tube to monitor internal strains. To validate the expanding plug test for external pressure, repeated tests were performed on a 4130 alloy steel tube of similar length and diameters as CMC architecture 13444-13-SG-X. The length of Steel tube was approximately 2.5” with an OD and ID of .422” and .308”, respectively.

After installation of a strain gauge along the inner surface of the validation tube, the tube was setup in the compression test with expanding plug. The upper crosshead was lowered until there was a noticeable reading of strain from the sample and containment strain gauges. At this point, the load and strain readings were zeroed. This ensures that the polymer plug has been radially displaced enough for initial contact with both the sample

and the containment tubes. Not only will the axial load from the compression test be used to determine pressure generated from the plug, pressure will also be approximated from the containment tube strain reading. The ADMET was set to load at a rate of 2000 N/min to a maximum load of 750 N. The figure below shows the approximated pressure profiles from axial load and containment strain for a typical compression test of 4130 Steel. From *Figure 3. 13*, the predicted plug pressure calculated from both recorded values closely follow the same trend and fall within the same magnitude. It can also be seen that the pressure determined by the axial load on the plug tends to be slightly greater.

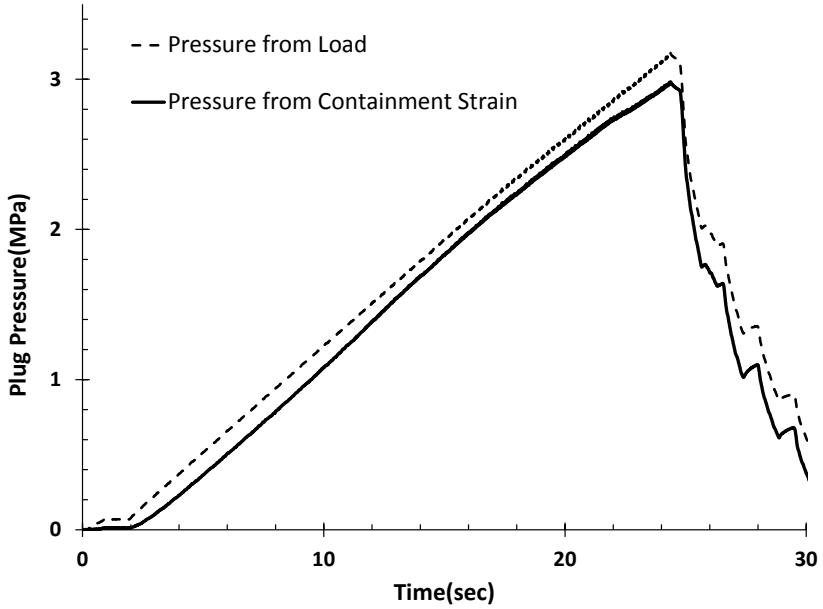

Figure 3. 13: Calculated Plug Pressure using axial load and containment strain during steel test

Both sets of pressures were used to calculate the hoop stress along the internal diameter of the steel sample. Internal hoop stress was found using *Equation 5*, below. This is the general Lame's equation for tangential stress (σ_θ) along the hoop direction of an open ended cylinder exposed at internal (P_i) and external pressure (P_o). Let r_i and r_o represent inner and outer radius, respectively.

$$\sigma_\theta = \frac{P_o {r_o}^2 - P_i {r_i}^2}{{r_o}^2 - {r_i}^2} + \frac{(P_o - P_i){r_i}^2 {r_o}^2}{{r_o}^2 - {r_i}^2}\frac{1}{r^2}$$ *Equation 5*

This equation can be simplified assuming no internal pressure and that the desired radius of stress observation is the inner radius. Therefore, the equation used to calculate inner hoop stress from this test is:

$$\sigma_\theta = \frac{2P_o {r_o}^2}{{r_o}^2 - {r_i}^2}$$ *Equation 6*

The calculated hoop stresses and corresponding recorded hoop strain can be plotted for determination of the elastic modulus for the 4130 alloy Steel. The stress-strain curve below indicates a linear correlation between the recorded data. Of four different loading, the elastic modulus for this steel tubing was averaged to be 212.2 and 203.3 GPa when calculated from axial load and containment strain, respectively. These values fall within 3.5 and 0.8% error of published values of elastic modulus for 4130 alloy steel. This testing confirms that the expanding plug method is an accurate method for simulating external pressure. Testing of CMC architecture 13444-13-SG-X tubing was then performed to determine if thick wall cylinder theory is a good approximation for composite tubing.

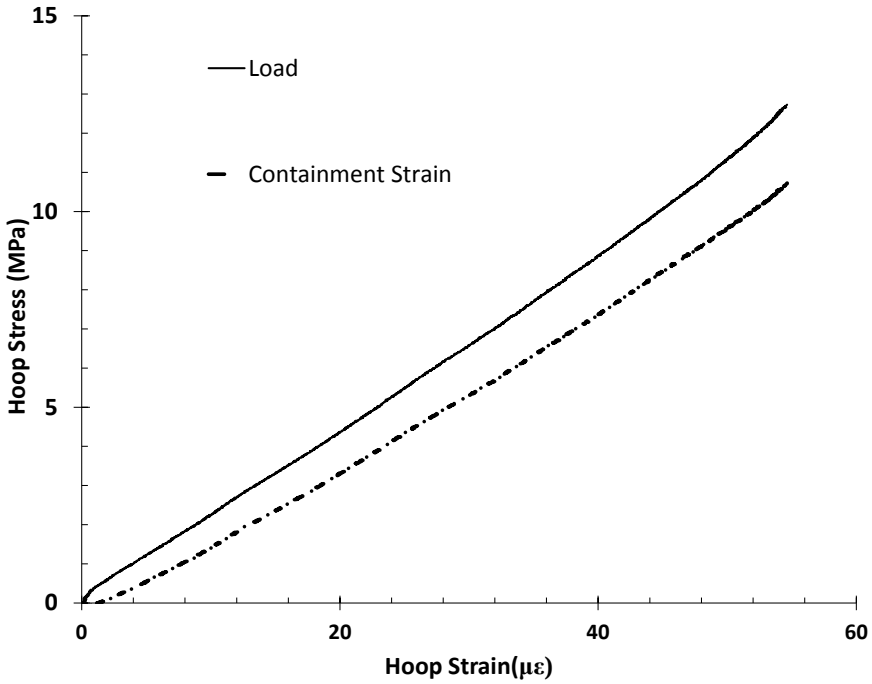

Figure 3. 14: Stress-strain plots determined from validation testing of 4130 alloy steel

3.10b Expanding Plug tests of SiC_f-SiC_m Composite within Elastic Range

After validation, external pressure tests were performed on three sample tubes of CMC architecture 13444-13-SG-X. All samples had nominal OD and ID of .410 inch and .295 inch, respectively, with tube lengths of 2.50 inch. Prior to expanding plug testing, all tubes were internally pressurized to low pressures (1500 psi/10 MPa) using the internal pressure rig. Internal pressure tests indicated that the average Young's Modulus along the hoop direction of the 13444-13-SG-X architecture tubes was 180.3 GPa. Hoop strain recorded from the expanding plug test will be compared to predicted strains calculated using the elastic modulus determined from internal pressure tests. This comparison will indicate whether thick wall cylinder theory can be adequately applied to estimate stress-strain behavior of composite cylinders under pressure.

Following the same test setup and loading rate for the expanding plug test for steel. The SiC_f-SiC_m composite samples 1, 2, and 3 were loaded to a maximum axial load of 750 N. This load was expected to be well within the elastic range for this material. External pressure testing of composite tubing to failure was investigated after elastic testing was performed. *Figure 3. 15* shows a typical calculated inner hoop stress curve for this architecture using axial load and containment strain.

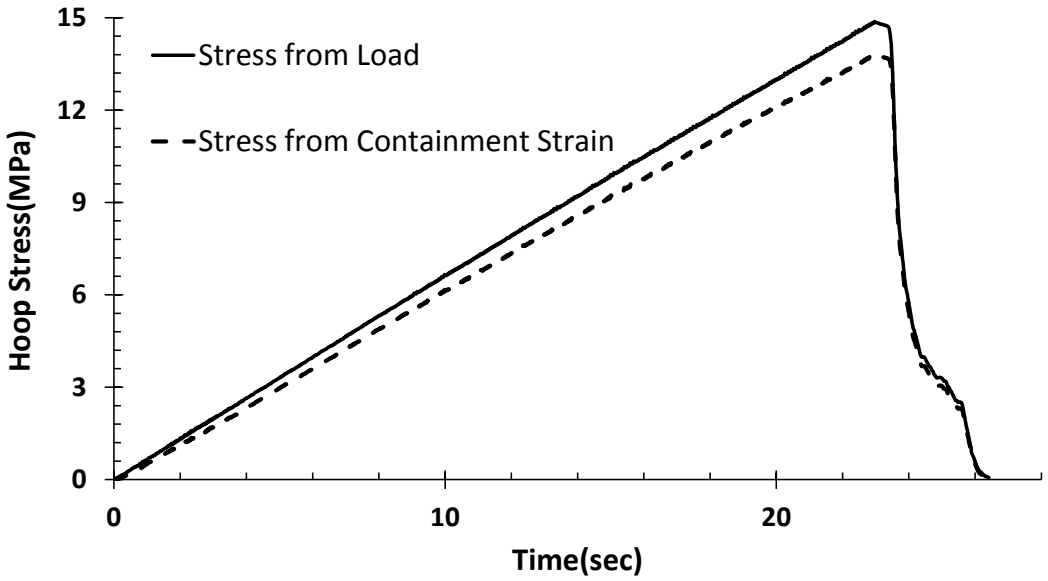

Figure 3. 15: Expected Inner Hoop Stress for sample 13444-13-SG-1

As with the tests performed on steel tubing, the pressure and corresponding hoop stress on the sample is slightly different when calculated from axial load and containment strain. In general, the stress determined by the compressive load on the polymer plug tends to be higher than from the containment strain. Using these hoop stresses and the calculated elastic modulus from internal pressure tests for this architecture, expected hoop strains can be found and compared to recorded strains from these tests. *Figure 3. 16*, below, shows the strain plots from the same expanding plug test.

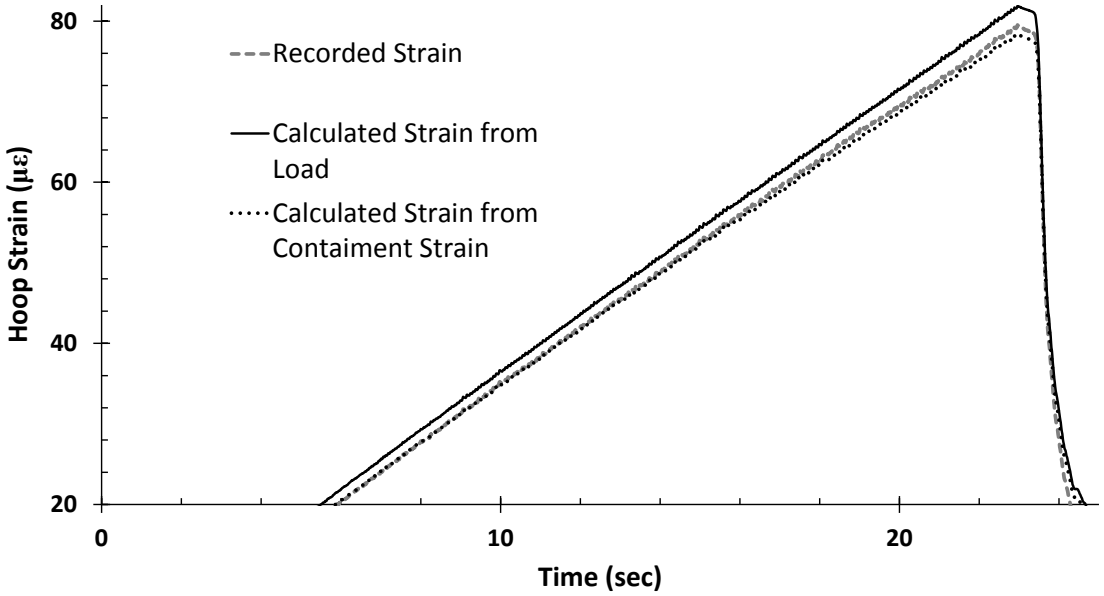

Figure 3. 16: Typical plot of recorded and calculated hoop strains along inner diameter of sample

It can be seen that recorded strain align very well with both sets of expected strains. For all composite samples tested, expected strains calculated from axial load tended to be slightly greater than recorded strains while strains found using the containment method tended to be closer to recorded strains. Expected strains calculated by the axial load method and the containment strain method came within 4.4% and 0.9%, respectively, of recorded strains. This small deviation from recorded data suggests that compression testing of SiC_f-SiC_m composite tubing can be accurately performed using the expanding plug setup devised in this study. This data also suggests that elastic modulus of CMC composites under tension and compression are similar. Unfortunately, the testing performed for this study does not explore the full stress-strain relationship of this material.

3.10c Expanding Plug tests of SiC_f-SiC_m Composite to Failure

As mentioned previously, a second loading cycle of the 13444-14-SG-X samples was performed till failure. It is of interest to identify the full stress-strain relationship of

this composite material under compression. The first loading cycle only determined this relationship within the elastic range. To ensure full composite tube failure, an 810 MTS load frame was used to load the samples at a rate of 20 kN/min until failure. *Figure 3.17*, shows the compression stress-strain plot for this architecture.

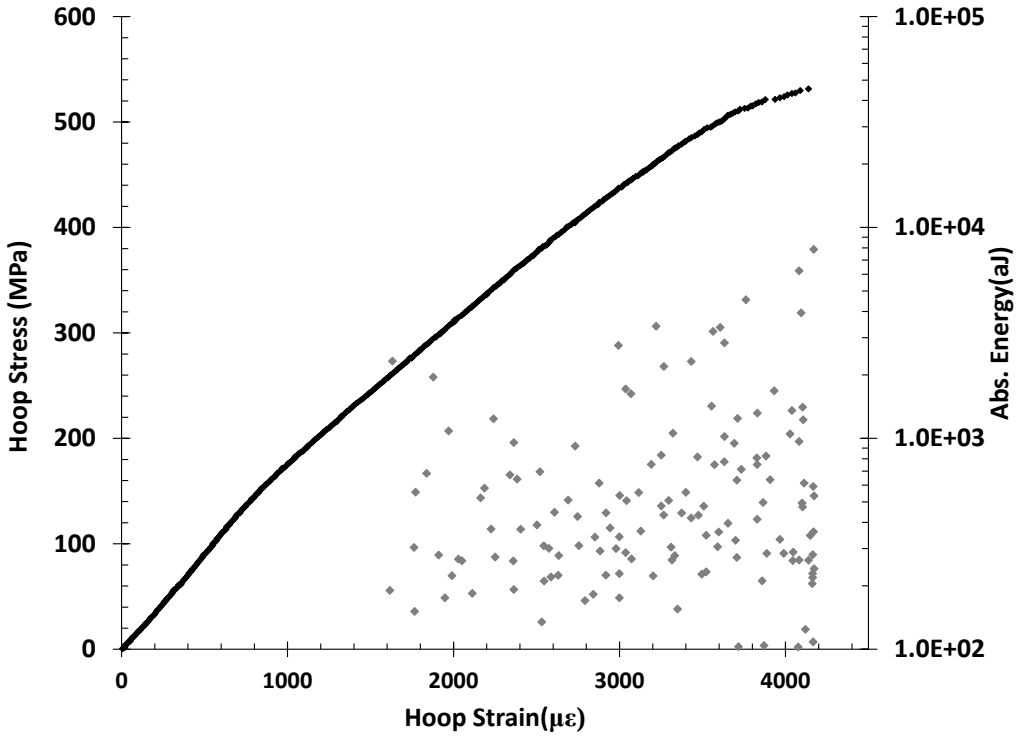

Figure 3. 17: Compressive Stress-Strain plot of sample 13444-13-SG-2 with recorded AE

It is to be noted is that the compression stress-strain curve is much different compared to the curve under tension. Under compression, there is only a slight change to the slope of curve. As seen from earlier tests in this work of SiC_f-SiC_m composite tubing, the composite experiences an apparent change in stress-strain relationship at the proportional limit stress (PLS). It can be argued that under compression this material experiences a subtle PLS. From the figure, the curve is linear until 150 MPa of hoop stress and the slope changes thereafter. At stresses greater than this, the slope of the curve gradually decreases until total sample failure. The maximum hoop stress along the internal

tube surface estimated for samples 1 and 2 were 539 and 532 MPa, respectively. Internal pressure tests of similar SiC_f-SiC_m composite tubing yielded ultimate tensile stresses around 380 MPa which is much smaller than the stresses observed under compression. In addition, PLS for SiC_f-SiC_m composite tubing under tension was also found to be lower than under compression.

Acoustic emission data recorded from these two tests were not ideal, however, show some indication of sample damage. Since it was impossible to directly attach the AE sensor to the sample, it is expected that the recorded signals would be attenuated. The first thing to note is that all AE signals are very weak compared to previously recorded AE data. With this in mind, it can be reasoned that any detected signals stem from high energy events where the signals simply attenuated while travelling to the sensor. As a result, it is likely that recorded signals are not from low energy matrix cracking but rather high energy fiber breaks or delamination. This would explain why there are no recorded AE signals at the end of the proportional limit (150 MPa), where matrix cracking has been prevalently observed. [17,31] Instead, AE signals do not first appear until roughly 280 MPa of hoop stress for both samples. It is believed that at this point, some late stage damage (fiber breakage, delamination) begins to occur.

The expanding plug method for simulating external pressure on a sample tube proves to be an effective method for performing compression tests of CMC composite tubing to failure. Similar to internal pressure tests, there is a rapid release of load as the material completely fails. *Figure 3.* 18, below, shows an image of a crushed composite sample. The ends of the tube are intact while the center portion of the tube has one long crack that spirals along the area in contact with the polymer plug. In addition, the diameter

of the tube section that was in contact with the plug is visibly smaller compared to the unloaded ends of the sample.

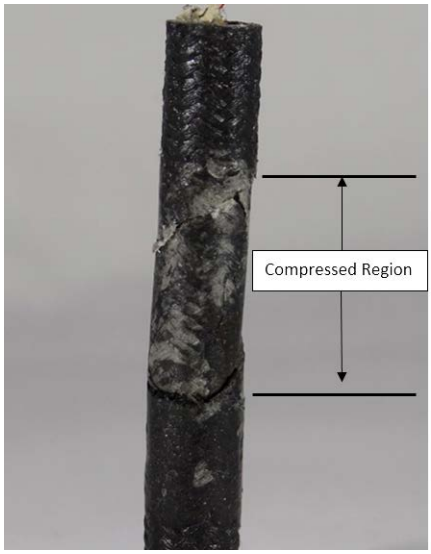

Figure 3. 18: Crushed 13444-13-SG-2 sample after expanding plug test till failure

3.10d Effect of Curvature and Pressure on Strain Reading

After much experimentation with strain gauge installation procedures, bonding adhesive, and testing pressures, a consistent method was developed to install strain gauges along the internal surface of a specimen tube to monitor internal strains. Initial material selected for internal gauge testing of internal pressure was 6061 Aluminum rod with an outer diameter of 1". To internally pressurize the tubing sample, all specimen for this study were tested on the internal pressure rig. The Aluminum tubing was cut to a length of 5" in order to prevent any unwanted stress deviations from the adapter lips. The inner diameters of each Aluminum specimen were lathed and thoroughly cleaned. For simplicity, the Aluminum samples will be called Sample A, B, and C, with ID of .310, .381, and .470 inches, respectively. Testing was performed on the three Aluminum samples to determine if the curvature of the tubing had an effect on the error in recorded strain reading versus the predicted inner strain reading based on thick walled cylinder theory.

With the gauges installed, each Aluminum tube was systematically loaded with gradually increasing pressures. To ensure strain measurement accuracy at each pressure, multiple tests were performed. The specimen was loaded three times to approximately 750 psi, followed by three times to 1500 psi, and then to 2000 psi. After these loading tests, the tube was finally loaded to 750 psi to determine if the strain gauge material may have permanently yielded. *Figure 3.19*, *Figure 3.20*, and *Figure 3.21*, show the measured hoop strains and predicted internal hoop strains for each Aluminum sample during a 2000 psi maximum loading.

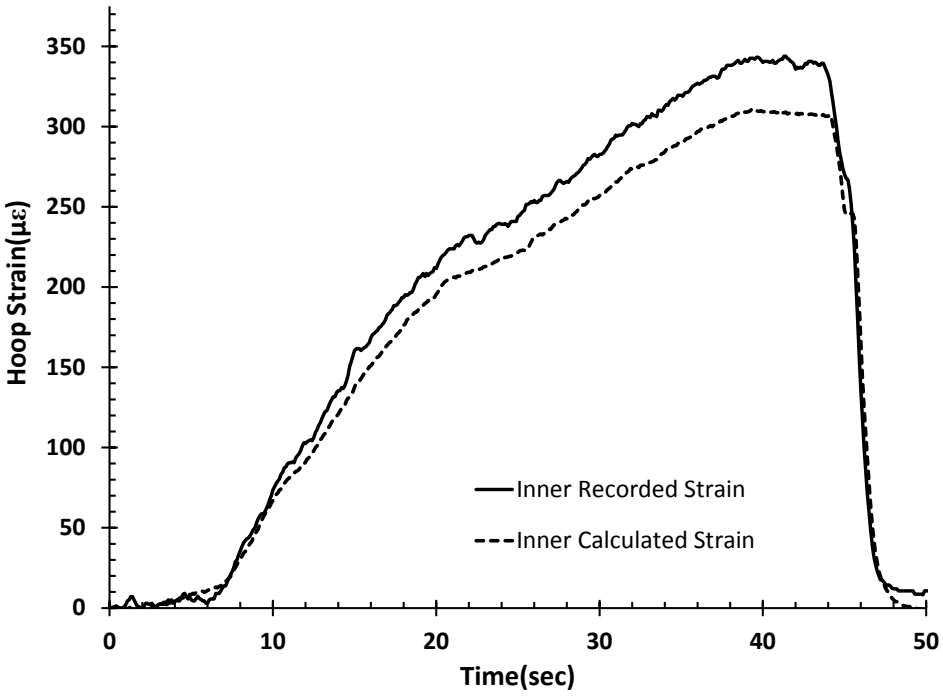

Figure 3.19: Recorded and Calculated Inner strain plot for Sample A during 2000 psi loading

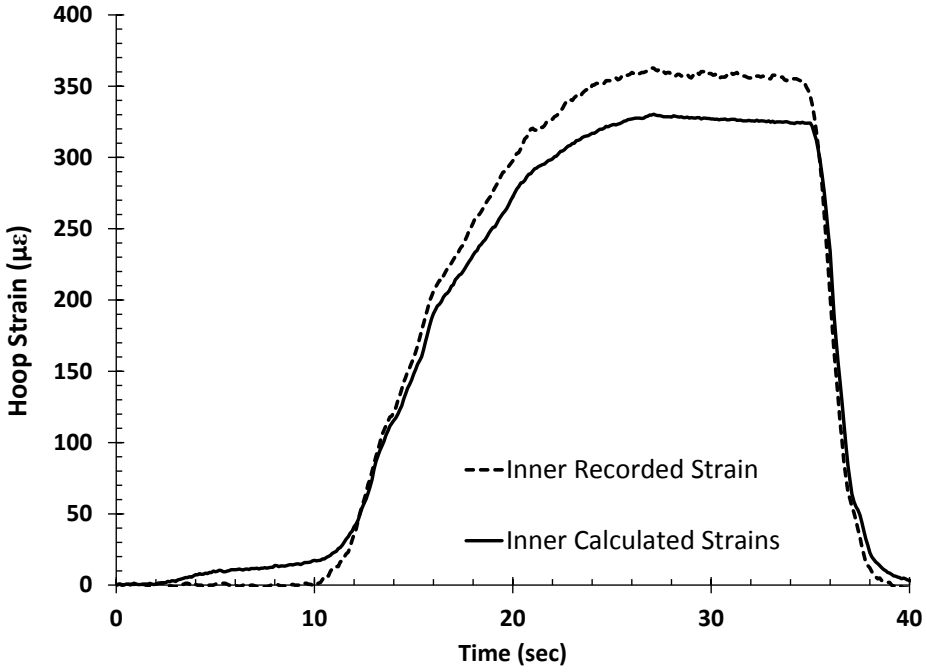

Figure 3.20: Recorded and Calculated Inner strain plot for Sample B during 2000 psi loading

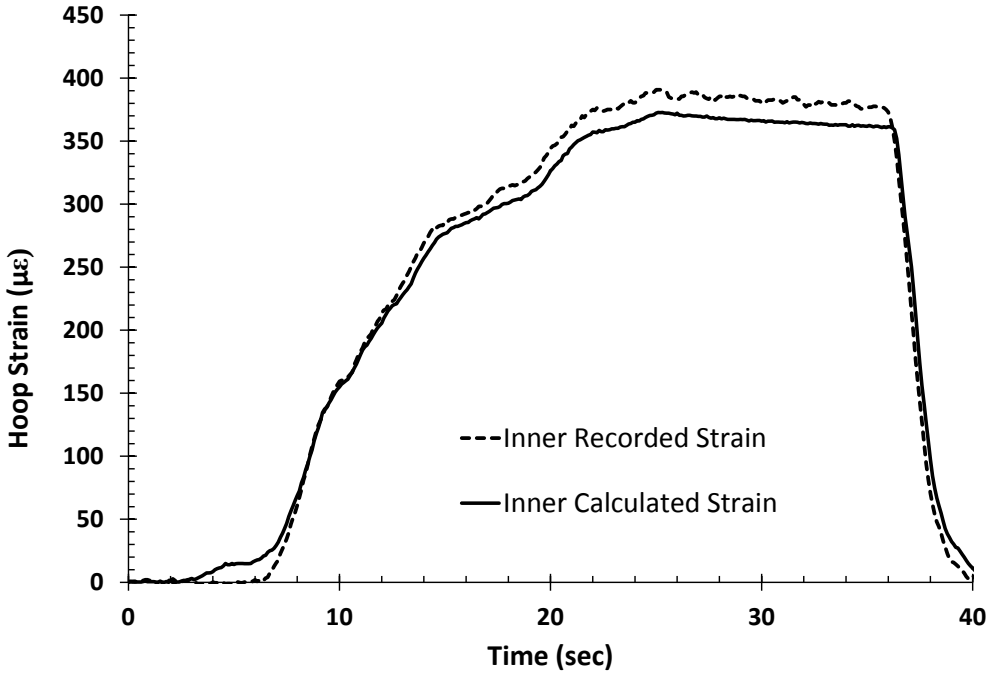

Figure 3.21: Recorded and Calculated Inner strain plot for Sample C during 2000 psi loading

Based upon these graphs, it can be seen that the recorded inner strain for these tubes is slightly higher than the predicted strains using thick walled cylinder theory. In addition,

it can be observed that with increases to adhered curvature, the level of error between these two values increases. *Table 3.6,* below, shows the averaged percent error observed for each Aluminum sample and pressure loading. Let it be noted, that these values were determined along the peak pressure plateau during each loading while pressure is held constant. The first trend in the table is that with a decrease to adhered strain gauge curvature (increase in tube inner diameter) there is a decrease to the percent error in the recorded and predicted strain values. This can be seen at all pressures including the 750 psi loading performed after initially loading to 2000 psi. The second trend is that with increasing internal pressure to the sample for all curvatures, there is an increase in the percent error. This is believed to be due to the substrate material of the strain gauge deforming with increased pressures. In addition, there is a greater strain reading in the second 750 psi loading test compared to the first. This indicates that the strain gauge may have yielded sometime after the initial 750 psi loading and therefore results in a greater recorded strain value.

Previous studies have been performed that investigate the effects of hydrostatic pressure on strain gauges. [70,71,72] It has been found that there is a linear deviation in recorded strain values based upon the pressure that the strain gauge is exposed to. For a gauge attached to a flat surface, the amount of deviation is within 7 micro-strain per 2000 psi. [72**Error! Bookmark not defined.**] Gerdeen investigated the effects of hydrostatic pressure on gauges bonded to both flat and curved surfaces. It was determined that there was a greater amount of strain recorded on the concave curved surface than the flat surface at the same hydrostatic pressure. *Figure 3.22*, shows the trend Gerdeen observed between recorded strain values of flat and curved surfaces. The two lines on the plot are based on differences in pressure gradients taken to achieve targeted pressure of 20 ksi. Although the

pressure and pressure gradient in this study are different than those seen in Gerdeen's investigation, the trend can be seen that with decreases to radius of curvature, there is a greater deviation (percent difference) between the recorded strain values and those predicted. [72**Error! Bookmark not defined.**] Gerdeen defines radius of curvature as radius of concave surface that the strain gauge is adhered to.

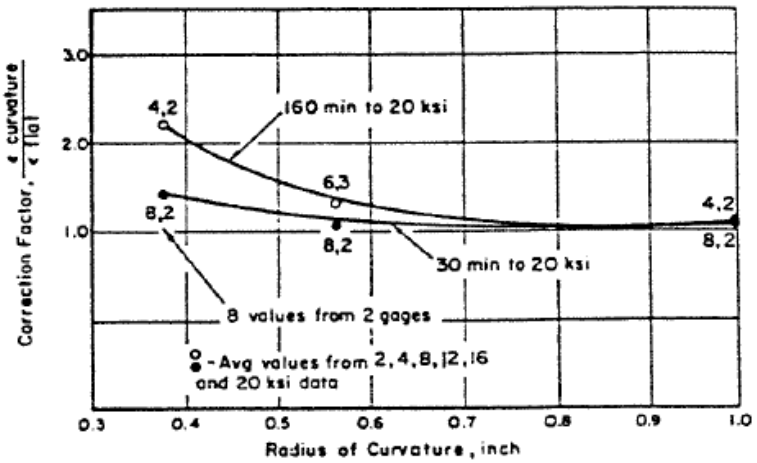

*Figure 3.22: Ratio (Correction Factor) between strains observed by gauges attached to curved and flat surfaces based upon differences curvature. [72**Error! Bookmark not defined.**]*

Table 3. 6: Recorded Percent Error between recorded and predicted inner strains for all Aluminum samples and loading.

Pressure Loading(psi)	A -.310" ID (%)	B -.381" ID (%)	C -.470" ID (%)
750	1.0	1.0	2.7
1500	9.3	7.5	3.0
2000	10.0	8.5	5.8
750(after)	11.1	8.3	4.2
7000	12.0	11.7	10.0

CHAPTER 4: CONCLUSIONS

Prior to investigation into impulse excitation for SiC_f-SiC_m composite nuclear cladding, validation of mechanical testing setup was performed to ensure accuracy and consistent sample characterization. Validation of tension, torsion, and internal pressure test setups resulted in elastic moduli values within 4% of published figures for the tested validation materials. Free vibration impulse excitation was performed on varying geometry of known material and good agreement was found between standardized ASTM vibration equations and alternative vibration equations accounting for complex cross-section. [37] Less than 5% difference was observed moduli between these two sets of equations and therefore validate use of impulse excitation on complex cross-section beams.

Use of fixed-free vibration experiments to determine axial Young's Modulus and Shear Modulus of circular beams indicate an expected error in Young's Modulus but not in Shear Modulus. For hollow and solid circular beams under torsional vibration, values of Shear Moduli were obtained within 6% of published data and therefore validate use of impulse excitation to accurately determine shear modulus for SiC_f-SiC_m composite tubing. It is believed that sample support compliance results in errors for recorded flexure vibration for known material. These flexure vibration errors are greater than desired and therefore axial Young's Modulus was not determined by pressure rig mounted IE. The alternative

solution was to simply normalize recorded flexure vibration and to monitor degradation of flexure frequency and damping over the course of testing.

Table mounted impulse excitation tests of SiC_f-SiC_m composite samples showed good consistency between the three tubes of 13464-17-06-X architecture. Average axial Young's Modulus determined by table mounted IE was 110.0 ± 3.5 GPa. Afterwards, the first sample of the three composite tubes was tested via mechanical tension, torsion, and internal pressure testing. The values of 109.7 GPa, 51.6 GPa, and 120.4 GPa were found for axial Young's Modulus, Shear Modulus, and Hoop Modulus, respectively. Acoustic emission data recorded during burst testing of sample 1 indicated the PLS for this composite architecture to fall between 24.1 MPa (3.5 ksi) and 25.5 MPa (3.7 ksi). As a result, internal pressure loadings for samples 2 and 3 were set to exceed this range in order to purposely induce composite damage without rupturing the tubing. Rig mounted impulse excitation tests were performed for samples 2 and 3 after each pressure loading. IE testing indicates a degradation of tubing flexure and torsional frequency with progression of damage. In addition, a similar increasing trend was noticed in measured damping over this same progression of material damage. It was also noted that flexure vibration values for both samples tended to have a greater change. Subsequent table mounted IE testing of the pressurized specimens indicated a slightly greater Young's Modulus compared to initial table mounted testing. Further testing of SiC_f-SiC_m composite tubes of the same architecture would provide more accurate and consistent data. A better understanding and monitoring of changes to vibrational values could also be achieved with more rigorous impulse excitation testing. The findings of this work indicate the usefulness of impulse

excitation in the mechanical characterization and structural health monitoring of SiC_f-SiC_m composite tubing as nuclear cladding.

Two experimental studies using internally attached strain gauges inside sample tubing were performed. The first study was to test a SiC_f-SiC_m composite tube under compression. This was performed through the development and use of a novel modified expanding plug configuration to simulate external pressure on a sample tubing. After validating that the test method was accurate on known material, the method was employed in testing a SiC_f-SiC_m composite architecture (13444-13-SG-X) to failure. Recorded strains came within 4.4% of expected internal hoop strains using classical thick wall cylinder theory. In addition, ultimate compressive stress observed for this sample was found to be 536 ± 3 MPa which appeared to be higher than the ultimate stresses under tension.

The second internally attached strain gauge study was performed on aluminum tubing with various inner curvatures loaded to multiple pressures. For this study, strain gauges were bonded along the inner surfaces of tubes with diameters of 7.87 mm (.310 in), 9.68 mm (.381 in), and 11.94 mm (.470 in). The general trend observed is that an increase in curvature generates a greater difference in recorded and expected strain readings. It was also seen that greater pressures acting on the attached strain gauge have a similar effect. Results from these tests correlate well with those performed in other literature. [72] When similar methodology and testing were applied to a SiC_f-SiC_m composite tube, a significantly greater error was seen. This is believed to be due to the deformation of the smoothing layer of epoxy placed between the strain gauge and the porous inner surface of the composite tubing along with the roughness of the SiC_f-SiC_m composite surface.

Work performed for this thesis has been exciting and challenging. New knowledge was gained through the impulse excitation testing and compression testing of the SiC_f-SiC_m composite tubing, however, there is still a considerable amount of information that can be explored in future testing. It is recommended that future impulse excitation testing will eventually be able to determine the hoop modulus of tubing material. Achieving this would make IET an even more versatile and common method for non-destructively characterizing composite fuel cladding. In addition, further investigation of the correlation between composite damage and vibrational behavior is highly recommended based upon data found in this work. The impulse excitation response of the SiC_f-SiC_m close to its ultimate failure would be of significant interest to explore in order to fully understand the material.

Future work into the study of CMC composites under compression is highly recommended. As seen in this study, testing of tension is common for this material while testing under compression requires more attention. Potential future experimentation for this topic is to develop a method of directly recording acoustic emission data from the sample material. To do so, a different testing setup would need to be designed. The expanding plug setup is reliable and accurate, however, only tests a small section of tubing. Unfortunately, the availability of composite tubing was limited. Should these experiments be replicated or expanded, it is highly recommended to test a larger number of samples to further quantify statistical variation.

After performing various mechanical tests on SiC_f-SiC_m composite tubing, the usefulness of this material for nuclear fuel cladding can easily be seen. CMC tubing can be designed in many different ways to have desired characteristics ideal for nuclear fuel. In

addition to observing the mechanical strengths of SiC_f-SiC_m composite tubing, this research has observed how easily the tubing can be non-destructively evaluated by impulse excitation. It is hoped that impulse excitation could potentially be employed commercially as a non-destructive testing technique in the nuclear industry.

REFERENCES

[1] Snead L.L., Nozawa T., Ferraris M., Katoh Y., Shinavski R., Sawan M." Silicon Carbide Composites as Fusion Power Reactor Structural Materials". *Journal of Nuclear Materials*. 417 (2011) 330-339.

[2] Riccardi B., Giancarli L., Hasegawa A., Katoh Y., Kohyama A., Jones R.H., Snead L.L."Issues and Advacnes in SiCf-SiCm Composites Development For Fusion Reactors". *Journal of Nuclear Materials.* 329-333 (2004) 56-65.

[3] Rohmer E., Martin E., Lorrette C., "Mechanical properties of SiC/SiC braided tubes for fuel cladding", *Journal of Nuclear Materials*, (2014) 6-21.

[4] Zinkle, S.J., Snead, L.L.,"Materiales Research and Development for Fusion Energy Application". *Oak Ridge National Laboratory*.(1998).

[5] Kerans, R. J., Hay, R. S., Pagano, N. J., and Parthasarathy, T. A.,"The Role of the Fiber–Matrix Interface in Ceramic Composites".*American Ceramic Society Bulletin*, (1989).

[6] Kim Daejong, Lee Hyun-Geun, Park Ji Yeon, Kim Weon-Ju."Fabrication and measurement of hoop strength of SiC triplex tube for nuclear fuel cladding applications". *Journal of Nuclear Materials.* 458 (2015) 29-36.

[7] Besmann, T.M., Sheldon, B.W., Lowden, R.A., Stinton, D.P. "Vapor-Phase Fabrication and Properties of Continuous-Filament Ceramic Composites". *American Association for the Advancement of Science*. (1991).

[8] Kohyama, A., Dong, S. -M., and Katoh, Y., "Development SiC/SiC Composites by Nano-Infiltration and Transient Eutectic (NITE) Process," *Ceramic Engineering Science Proceedings*, (2002) 311.

[9] Sherwood, W. J., "CMCs Come Down to Earth," *American Ceramic Society Bulletin*, (2003) .

[10] Kim Weon-Ju, Kim Daejong, Park Ji Jeon."Fabrication and Material Issues for the Application of SiC Composites to LWR Fuel Cladding". *Nuclear Engineering and Technology*. 45 (2013) 565-573.

[11] Hsu David K."Nondestructive Inspection of Composite Structures: Methods and Practice". *17th World Conference on Nondestructive Testing*. (2008)

[12] Katoh Y., Snead L.L., Henager Jr. C.H., Hasegawa A., Kohyama A., Riccardi B., Hegeman H., “Current status and critical issues for development of SiC composites for fusion applications”, Journal of Nuclear Materials, (2007) 367-370.

[13] Unnthorsson Runar, Jonsson M.T., Runarsson T.P."NDT Methods for Evaluating Carbon Fiber Composites". *University of Iceland*. (2004)

[14] Talreja Ramesh."Damage Mechanics of Composite Materials". *Texas A&M University*. (2012)

[15] Evans Anthony G., He Ming Y."Interface Debonding and Fiber Cracking in Brittle Matrix Composites". *Journal of American Ceramics*. 72 (1989).

[16] Mosley K., “The stressing for test purposes of materials in tubular form using elastomeric inserts – experimental and theoretical development”, *Proceedings of the Institution of Mechanical Engineers*, (1982) 123-139.

[17] Shapovalov Kirill."Mechanical Characterization of SiC-SiC Nuclear Fuel Cladding by a Novel Hydraulic Internal Pressurization Method". *University of South Carolina*. (2014)

[18] Jacobsen G., Stone J.D., Khalifa H.E., Deck C.P., Back C.A., “Investigation of the C-ring test for measuring hoop tensile strength of nuclear grade ceramic composites”, *Journal of Nuclear Material.*, (2014) 125-132.

[19] Nozawa T., Ozawa K., Choib Y., Kohyamac A., Tanigawaa H., “Determination and prediction of axial/off-axial mechanical properties of SiC/SiC composites”, *Fusion Engineering and Design*, (2012) 803-807.

[20] Kim, W. -J., “Development and Application of Continuous Fiber Ceramic Composites,” *Ceramics Korean*. 65 (2007).

[21] Hellier, C. J. "The Handbook of Nondestructive Evaluation". New York, N.Y.: *McGraw-Hill*.(2001).

[22] Tensi Hans Maria."The Kasier-Effect and its Scientific Background". *26th European Conference on Acoustic Emission Testing*. (2004)

[23] Gholizadeh S."A Review of Non-Destructive Testing Methods of Composite Materials". *Procedia Structural Integrity*. 1 (2016) 50-57.

[24] Harding C.A., Hugo G.R."Review of Literature on Probability of Detection for Liquid Penetrant Nondestructive Testing". *Australian Government Department of Defense*. (2011).

[25] Lu, Z. Y., Zhang, Q. L., and Liu, X. "New Magnetic Particle Cassette NDT Intelligent Detection Device". *Fourth International Conference on Intelligent Systems Design and Engineering Applications*, (2013) 403-406.

[26] Groz X.E., Ogi K, Takahashi K."Eddy Current, Ultrasonic C-scan and Scanning Acoustic Microscopy Testing of Delaminated Quasi-isotropic CFRP Materials: A Case Study". *Journal of Reinforced Plastics and Composites*. 17 (1998)

[27] Wrobel G., Wierzbicki L."Ultrasonic Methods in Diagnostics of Polyethylene". *Archives of Materials Science and Engineering*. 28 (2007) 413-416.

[28] Djordjevic B. Boro."Ultrasonic Characterization of Advanced Composite Materials". *10th International Conference of the Slovenian Society for Non-Destructive Testing.* (2009).

[29] Cohen, Y. and A. K. Mal, "Ultrasonic Inspection," *NDE and Quality Control,* ASM International, Metals Park, OH, (1989) 231-277.

[30] Kim Weon-Ju, Kim Daejong, Jung Choong Hwan, Park Ji Yeon, Snead Lance L."Nondestructive Evaluation of Microstructure of SiC/SiC Composites by X-ray Computed Microtomography". *Journal of the Korean Ceramics*. 6 (2013) 378-383.

[31] Morscher, G. N. and Godin, N., "Use of Acoustic Emission for Ceramic Matrix Composites, in Ceramic Matrix Composites: Materials, Modeling and Technology", *John Wiley & Sons*, Inc., Hoboken, NJ, USA. (2014).

[32] Oliveira Davi F., Soares Sergio D., Lopes Ricardo T."Inspection of Composite Pipelines using Computed Radiography". *5th Pan American Conference for NDT*. (2011).

[33] Martin, R. E., Gyekenyesi, A. L., Shepard, S. M., "Interpreting the Results of Pulsed Thermography Data". *Materials Evaluation*, 61 (5), (2003) 611–616.

[34] Plotnikov Yuri A., Winfree William P."Visualization of Subsurface Defects in Composites using a Focal Plane Array Infrared Camera*"*. *NASA Langley Research Association*. (1998).

[35] Hung, Y.Y. and Shang, H.M.“A unified approach for holography and shearography in surface deformation measurement and nondestructive testing”. *Optical Engineering*. 42 (2003) 1197-1207.

[36] Roebben Gert, Bollen B., Van der Biest Omer, Van Humbeeck J."Impulse Excitation Apparatus to Measure Resonant Frequencies, Elastic Modulit, and Internal Friction at Room and High Temperature" *American Institute of Physics*. (1997).

[37] ASTM E1876-01, *ASTM International*, J.W. Lemmens, 2002.

[38] Blanter, Mikhail S., Golovin, Igor S., Neuhauser Hartmut, Sinning Hans-Rainer. "Internal Friction in Metaillic Materials". *Springer*. (2007).

[39] Lazan, B.J. "Damping of Materials and Members in Structural Mechanics". *Pergamon*, Oxford Lebedev, A.B. (1968).

[40] Viens Michael J., Johnson Jeffrey J." Determination of Elastic Moduli of Fiber-Resin Composites Using an Impulse Excitation Technique". *NASA Technical Memorandum*. (1996)

[41] Crane Roger M., Gillespie John W. Jr. "Damping Loss Factor Determination of Glass and Graphite Fiber Composites". *United States Navy*. (1989).

[42] Otani Lucas B., Amico Sandro C., Trindade Rafael S., Pereira Antonio H.A."Characterization of the Elastic Moduli of Composite Materials by the Impulse Excitation Technique". *2nd Brazillian Conference on Composite Materials*. (2014).

[43] Atri R.R., Ravichandran K.S., Jha S.K."Elastic Properties if in-situ Processed Ti-TiB Composites Measured by Impulse Excitation of Vibration". *Materials Science and Engineering*. 271 (1999) 150-159.

[44] Bemis, Richard A., Shiloh Lara, and Ellington William. "Nondestructive Evaluation of Thermally Shocked Silicone Carbide by Impact-Accoustic Resonance". *American Society of Mechanical Engineers*. (1995).

[45] Chung D.D.L. "Review Materials for Vibration Damping". *Journal of Materials Science*. 36(2001) 5733-5737.

[46] Timoshenko S., Young D.H, Weaver W. Jr."Vibration Problems in Engineering". *John Wiley And Sons.* (1974)

[47] Pickett G."Equations for Computing Elastic Constraints from Flexural and Torsional Resonant Frequencies of Vibration of Prisms and Cylinders". *Proceedings American Society for Testing and Materials*. (1945)

[48] Spinner S., Reichard T.W., Tefft W.E."A Comparison of Experimental and Theoretical Relations between Young's Modulus and the Flexural and Longitudinal Resonance Frequencies of Uniform Bars". *Journal of Research of the National Bureau of Standards*. (1960)

[49] Archambault, Rene. "The Past, Present, and Future of Vibration Analysis". ETD. N.p., (2017). Web. 17 Mar. 2017.

[50] Rathbone, T.C. "Vibration Tolerance". *Power Plant Engineering*. New York (1939).

[51] Heritage K, Frisby C, Wolfende A." Impulse Excitation Technique for Dynamic Flexural Measurements at Moderate Temperature". *Review of Scientific Instruments*. (1988).

[52] Radovic Miladin, Lara-Curzio Edgar."Comparsion of Different Experimental Techniques for Determination of Elastic Properties of Solids". *Materials Science and Engineering*. (2004).

[53] Swarnakar A.K., Gimenez S., Salehi S. Vleugels J. Van der Biest O."Recent Advances in Material Characterization using the Impulse Excitation Technique". *Key Engineering Materials*. 333 (2007) 235-238.

[54] Jung Jaehyuk, Kozeschnik E., Han Seong Ho, Cooman Bruno C. "Analysis of the Mechanical Properties of N-added CMn Structural Steel by the Impulse Internal Friction Technique". *Metallurgical and Materials.* (2012).

[55] Goken Jurgen, Riehemann Werner." Damping Behavior of AZ91 Magnesium Alloy with Cracks". *Materials Science and Engineering*. 370 (2004) 417-421.

[56] Finegan Ioana C., Gibson Ronald F. "Recent Research on Enhancement of Damping in Polymer Composites". *Composite Structures*. 44 (1999) 89-98.

[57] Roebben Gert, Duan Ren-Guan, Sciti Diletta, Van der Biest Omer."Assessment of the High Temperature Elastic and Damping Properties of Silicon Nitrides and Carbides with the Impulse Excitation Technique". *Journal of the European Ceramic Society*. 22 (2002) 2501-2509.

[58] Roebben Gert, Basu B., Vleugels J., Van der Biest Omer, Van Humbeeck J."The Innovative Impulse Excitation Technique for High-Tempertaure Mechanical Spectroscopy". *Jounral of Alloys and Compounds*. 310 (2000) 284-287.

[59] Song Wenlei, Zhong Yongteng, Xiang Jiawei."Mechanical Parameters Identification for Laminated Composites Based on the Impulse Excitation Technique". *Composite Structures*. 162 (2017) 255-260.

[60] Alva L.H., Huang X., Jacobsen G.M., Back C.A., "High pressure burst testing of SiCf-SiCm composite nuclear fuel cladding", *Conference Proceedings Of The Society For Experimental Mechanics Series*, (2014) 387-393.

[61] Smith Craig, Gyekenyesi Andrew."Detecting Cracks in Ceramic Composites by Electrical Resistance." *Ohio Aerospace Institute*. (2010).

[62] Smith Craig, Morscher G.N., Xia Z."Electrical Resistance as a NDE Technique to Monitor Processing and Damage Accumulation in SiC/SiC Composites". *National Aeronautics and Space Administration*. (2017).

[63] Hu Xunxiang, Ang Caen K., Singh Gyanender P., Katoh Yutai. "Technique Development for Modulus, Microcracking, Hermeticity, and Coating Evaluation Capability for Characterization of SiC/SiC Tubes". *Oak Ridge National Laboratory*. (2016).

[64] "RFDA Professional". IMCE Inc. http://imce.net/products/rfda-professional. (2017)

[65] MacBain J.C., Genin Joseph."Effect of Support Flexibility on the Fundamental Frequency of Vibrating Beams". *Journal of Franklin Institute*. 296 (1973).

[66] Afolabi D."Natural Frequencies of Cantilever Blades with Resilient Roots". *Journal of Sound and Vibration*. 110 (1986) 429-441.

[67] Wang Chao, Zhang Yamei, Ma Aibin."Investigation into the Fatigue Damage Process of Rubberized Concrete and Plain Concrete by AE Analysis". *Journal of Materials in Civil Engineering*. 7 (2011).

[68] Brebels A., Bollen B. "Non-Destructive Evaluation of Material Properties as Function of Temperature by the Impulse Excitation Technique". *The Journal of Nondestructive Testing*. (2014).

[69] Wang Kaihing."Vibration Analysis of Cracked Composite Bending-Torsion Beams for Damage Diagnosis". *Virginia Polytechnic Institute and State University*. (2004).

[70] Kular Gurnam."Use of Foil Strain Gage at High Hydrostatic Pressure". Experimental Mechanics. (1972).

[71] Schock R.N., Duba A.G."Pressure Effects on the Response of Foil Strain Gages". Experimental Mechanics. (1973).

[72] Gerdeen J.C."Effects of Pressure on Small Foil Strain Gages". Experimental Mechanics. (1963) 73-80.

[73] Ringeni, P.L., Actis M.D., Patanella A.J. "An Experimental Technique for Determining Mass Inertial Properties of Irregular Shape Bodies and Mechanical Assemblies". Measurement. (2001) 63-75.

APPENDIX A – TRIFILAR PENDULUM TEST FOR POLAR MOMENT OF INERTIA

A.1 Purpose

In order to determine the torsional frequency of the tube assembly with an add-on clamp, it is necessary to know the polar moment of inertia of the clamp. The complex geometry of the clamp makes it challenging to determine this by theoretical calculation. Therefore, effort was made to measure it directly by experiments. A Trifilar Pendulum test was employed to accurately determine the polar moment of inertia.

A.2 Derivation

Consider a symmetrical object suspended by three evenly spaced wires. *Figure A.1* shows a schematic of the rotation of a trifilar pendulum. Assume vector R is the central axial vector of the object, P is the point from which the wire hangs, and A is the point at which the wire supports the object at rest. Let α be angle of rotation of the object causing the end wire to move to point B. Let line AC be a projection of arc AB in the plane perpendicular to line AP.

For small object rotation, assume the length of line AC is equivalent to the length of arc AB. Therefore, the follow statements can be assumed:

$$\frac{AC}{L} = \frac{S}{L} = \tan(\theta) \qquad \textit{Equation 7}$$

$$\frac{AC}{R} = \frac{S}{R} = \tan(\alpha) \qquad \textit{Equation 8}$$

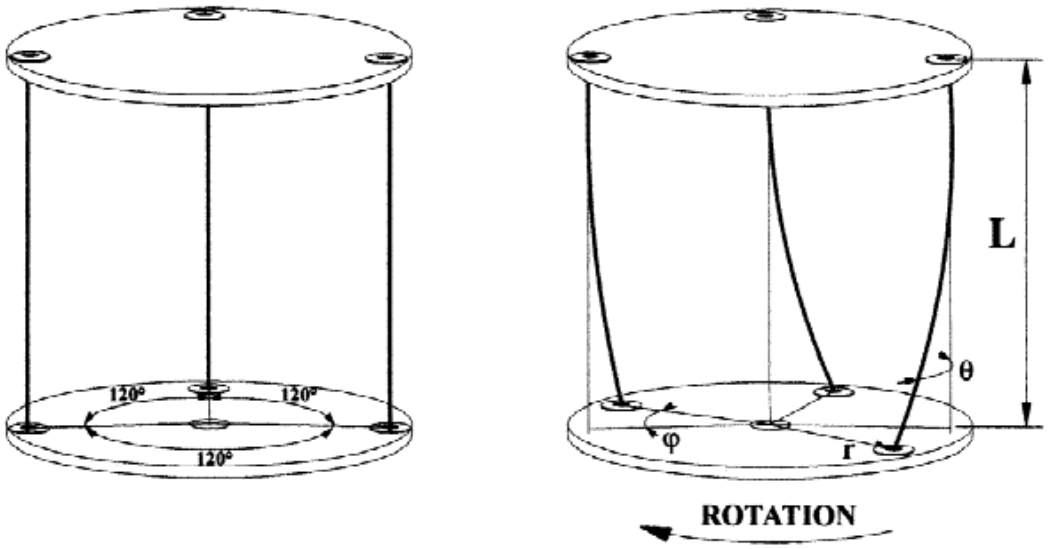

Figure A. 1: Schematic of rotation for a trifilar pendulum [73]

Assuming that the angles are small,

$S = L\theta$ *Equation 9*

$S = R\alpha$ *Equation 10*

Combining *Equations 9* and *10,*

$\theta = \frac{R}{L}\alpha$ *Equation 11*

As seen in *Figure A.1* there is a resultant force when the object is rotated.

$F = -T_1 sin(\theta)$ *Equation 12*

Assuming the angle is small,

$F = -T_1\theta$ *Equation 13*

This force acts along the radial direction and produces a restoring torque for the object

$\tau_1 = -T_1\theta R$ *Equation 14*

Assuming the same length for all three of the support wires, there will be three torques present when the object is rotated. The summation of torque acting upon the object is equivalent to the moment of inertia (I) multiplied by the angular acceleration ($\ddot{\alpha}$) of the object. Therefore:

$$\tau_1 + \tau_2 + \tau_3 = I\ddot{\alpha} \qquad \textit{Equation 15}$$

By substituting *Equation 14* for the torque from all wires, *Equation 16* can be found.

$$-R\theta(T_1 + T_2 + T_3) = I\ddot{\alpha} \qquad \textit{Equation 16}$$

It can be seen that the summation of the wire tension is equal to the total weight (W) of the object. Making this substitution and replacing angle θ by *Equation 11* result in the equation for harmonic motion.

$$I\ddot{\alpha} + \frac{R^2 W\alpha}{L} = 0 \qquad \textit{Equation 17}$$

Solving this second order differential equation leads to the equation for object rotational frequency (f).

$$f = \frac{1}{2\pi}\sqrt{\frac{R^2 W}{IL}} \qquad \textit{Equation 18}$$

From the frequency equation, the period of motion (T) can found.

$$T = 2\pi\sqrt{\frac{IL}{R^2 W}} \qquad \textit{Equation 19}$$

Rearranging results in the Polar Moment of Inertia for the object as a function of the period of motion.

$$I = \frac{mgr^2T^2}{4\pi^2 L} \qquad \textit{Equation 20}$$

A.3 Procedure

The premise behind this test is to experimentally determine the moment of inertia of a rotating system involving the desired object supported on disk. After finding the total moment of inertia for the system, the moment of inertia for the supporting disk can be subtracted from the total. This yields the experimentally determined polar moment of inertia for the desired object.

A pendulum rig was created using two thin, plastic plates of the same measured mass, thickness, and diameter. Three, small holes were cut through the plates within a millimeter of the

edge. The holes were spaced 120^0 degrees from each other around each plate. High strength fishing line was then tied from one hole of a plate to the corresponding hole of the other plate. As a result, there were three equal lines connecting the two plates. The length of each connecting wire between the plates was 2 meters.

One plate was securely clamped parallel to the floor along a support rack in the lab. This allowed the lower plate to freely hang parallel to the floor in midair. Determination of the moment of inertia for the plate simply requires angularly displacing the plate and releasing it. The plate will then enter a cyclic harmonic rotational motion. Using a stopwatch, the period of motion was determined. *Equation 20* can then be used to find the moment of inertia.

After the moment of inertia for the support plate was found, the upper clamp was set on the support plate. The clamp was set so that its axis of symmetry was aligned with the center of the plate as seen in *Figure A.2.*

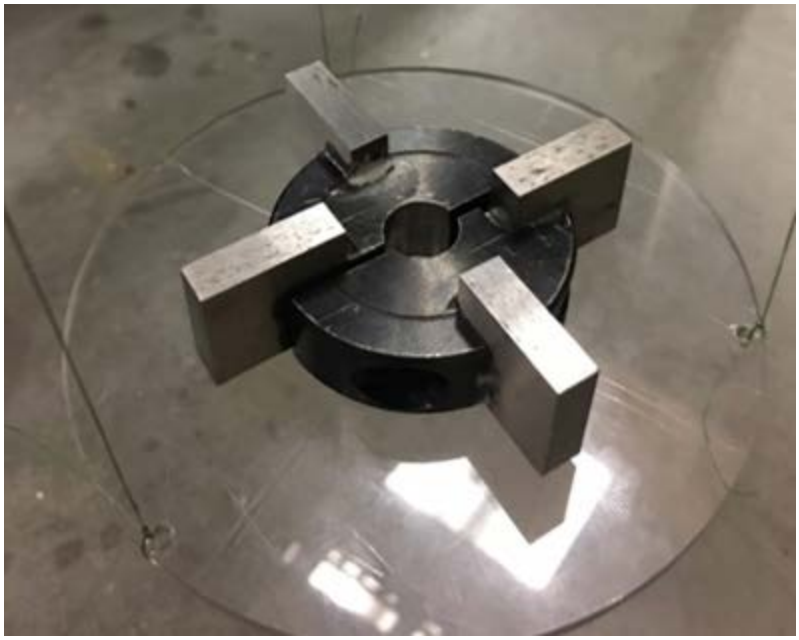

Figure A. 2: Image of upper clamp on support for trifilar pendulum test

The same procedure was performed as with just the support plate. After finding the period of motion for the total system, the total polar moment of inertia can be found. By

subtracting the moment of inertia found for just the support plate, the remaining value is the polar moment of inertia for the upper clamp. The obtained value was used in the torsional vibration calculation performed during pressure rig mounted impulse excitation experiments. Polar moment of inertia used for IE experiments was 7.22E-5 kg m^2 and falls within the range of 7.19 - 7.25E-5 kg m^2 based on accuracy analysis.

APPENDIX B – BEAM VIBRATION DERIVATION

B.1 Transverse Beam vibration

The governing equation based on Euler-Bernoulli beam theory, *Equation 21*, describes transverse displacement of beam under bending. Let y(x,t), f(x,t), m(x), and EI(x) represent transverse displacement, transverse force per unit length, mass per unit length, and flexural rigidity, respectively.

$$\frac{\partial^2}{\partial x^2}\left(EI(x)\frac{\partial^2 y(x,t)}{\partial x^2}\right) + m(x)\frac{\partial^2 y(x,t)}{\partial t^2} = f(x,t) \qquad \textit{Equation 21}$$

For free vibration, it is assumed the external forces, f(x,t), are zero and the governing equation can be simplified to *Equation 22*.

$$c^2\frac{\partial^4 y(x,t)}{\partial x^2} + \frac{\partial^2 y(x,t)}{\partial t^2} = 0 \qquad \textit{Equation 22}$$

Where:

$$c = \sqrt{\frac{EI}{\rho A}} \qquad \textit{Equation 23}$$

Since *Equation 22* contains a second order derivative with respect to time (t) and a fourth order derivation with respect to x, two initial equations and a minimum of four boundary conditions are required to find a solution to the transverse displacement. For any set of boundary conditions it is assumed that initial transverse displacement and velocity at any value of x at t=0 is equal to a known value. Therefore, the initial conditions for the beams are *Equations 24* and *25*, where υ is transverse velocity.

$$y(x,0) = y_o(x)$$ *Equation 24*

$$\frac{\partial y(x,0)}{\partial t} = v_o(x)$$ *Equation 25*

The separation of variables method was employed to separate *Equation 22* into a set of ordinary differential equations. *Equation 26* shows the newly defined variables W and T as functions of x and t separately.

$$\mathrm{y(x,t) = W(x)T(t)}$$ *Equation 26*

Substituting *Equation 26* into *Equation 22* and using the specific initial conditions, yields the following equations, *Equations 27* and *28*, for the transverse displacement as functions of x and t.

$$\frac{d^4W(x)}{dx^4} - \lambda^4 W(x) = 0$$ *Equation 27*

$$\frac{d^2T(t)}{dt^2} + \omega^2 T(t) = 0$$ *Equation 28*

Where:

$$\lambda^4 = \frac{\omega^2}{c^2}$$ *Equation 29*

Simplifying *Equation 29*, yields *Equation 30*. After substituting *Equation 23* into *Equation 30*, a simplified solution for the transverse natural frequency (ω) can be found which a function of beam length (L).

$$\omega = \lambda^2 c$$ *Equation 30*

$$\omega = (\lambda L)^2 \sqrt{\frac{EI}{\rho A L^4}}$$ *Equation 31*

The general solution to *Equation 27* is shown below, in which A, B, C, and D are integration constants to be determined based on the various possible boundary conditions.

$$W(x) = Asin(\lambda x) + Bcos(\lambda x) + Csinh(\lambda x) + Dcosh(\lambda x)$$ *Equation 32*

For the case of a beam with freely supported ends, it is assumed that both bending moment and shear force at beam ends are zero; therefore, the boundary conditions are:

$$W''(0) = W''(L) = 0 \qquad \textit{Equation 33}$$

$$W'''(0) = W'''(L) = 0 \qquad \textit{Equation 34}$$

After solving *Equation 32* with the above boundary conditions, the value of λL in *Equation 31* in the first mode of beam vibration is found to be 4.73. The equation of transverse beam displacement for a fixed-free beam is the same as *Equation 32*, however, the boundary conditions are different. The free end experiences no bending moment or shear force while the fixed end experiences no transverse deflection or rotation. The equations below outline these boundary conditions.

$$W''(L) = W'''(L) = 0 \qquad \textit{Equation 35}$$

$$W(0) = W'(0) = 0 \qquad \textit{Equation 36}$$

After solving *Equation 32* with the above boundary conditions, the value of λL in the first mode of beam vibration is found to be 3.516 for flexure (transverse) vibration. To account for the additional mass of the upper clamp, *Equation 31* is modified to *Equation 37* where M is the mass of the clamp.

$$\omega = (\lambda L)^2 \sqrt{\frac{EI}{\rho AL^4 + ML^3}} \qquad \textit{Equation 37}$$

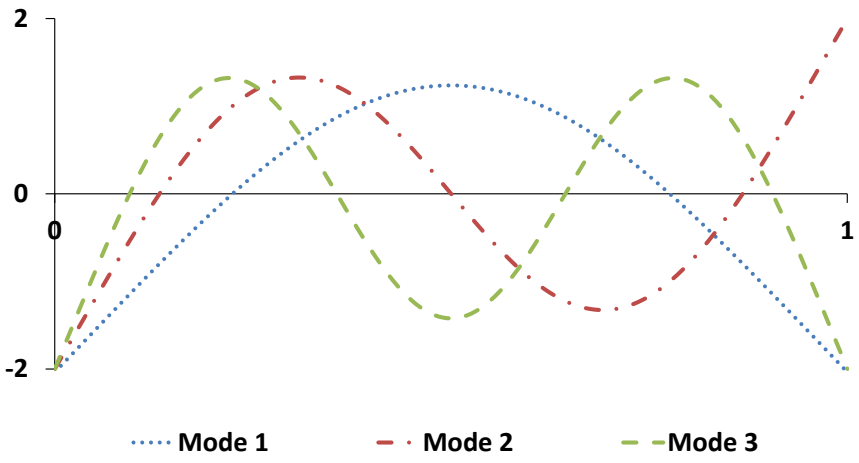

Figure B. 1: First 3 modes of transverse vibration for a freely supported beam

From *Figure B.1*, the nodes and antinodes of each mode can be determined. The x-axis is the normalized length of the beam while the y-axis is the normalized amplitude of the transverse beam displacement. Nodes indicate no beam deflection and are therefore located in the graph where the plots intersect the x-axis. Antinodes are defined as the location of greatest displacement from the x-axis. *Table B.1*, tabulates the node and antinode locations for the first 3 modes of transverse beam vibration with freely supported ends. It is at these nodes that the samples will be supported during impulse excitation. This will ensure that the support wires have minimal effect on the sample displacement during testing.

Table B. 1: Node Locations of freely supported Transverse Beam Vibration

Mode	Number of Nodes	Normalized Node Location
1	2	.224 .776
2	3	.132 .500 .868
3	4	.094 .356 .644 .906

B.2 Axial Vibration

Equation 38 is the governing equation for longitudinal displacement of a bar. A, ρ, E, and u are cross-section area, density, Young's Modulus, and axial displacement, respectively.

$$\rho A \frac{\partial^2 u(t)}{\partial t^2} = AE \frac{\partial^2 u(x)}{\partial x^2} \qquad \textit{Equation 38}$$

The axial displacement is a function of both time and space. Similar to the solution process of beam transverse vibration equation the governing PDE was converted into two ordinary differential equations in which axial displacement can be solved based on beam location (x) only. After separation of variables, the two ordinary differential equations, *Equation 40* and *41*, can be found.

$$u(x,t) = \phi(x)v(t) \qquad \textit{Equation 39}$$

For this case, axial displacement as a function of x is investigated.

$$v''(t) + \omega^2 v(t) = 0 \qquad \textit{Equation 40}$$

$$\phi''(x) + \lambda^2 \phi(x) = 0 \qquad \textit{Equation 41}$$

Where:

$$\lambda = \omega \sqrt{\frac{\rho}{E}} \qquad \textit{Equation 42}$$

The general solution to *Equation 41* is shown below and is the fundamental equation for determining the natural frequency and mode shape for beams with various boundary conditions.

$$\phi(x) = A\cos(\lambda x) + B\sin(\lambda x) \qquad \textit{Equation 43}$$

In the case of a bar with both ends free, the boundary conditions for axial displacement are below.

$$\phi'(0) = \phi'(L) = 0 \qquad \textit{Equation 44}$$

Solving *Equation 43* with the above boundary conditions yields the eigenvalue, λ. This value is only for the first mode of vibration.

$$\lambda = \frac{\pi}{L} \qquad \textit{Equation 45}$$

Equating *Equation 42* and *45* and then rearranging variables result in *Equation 46* which is the natural frequency for a bar in free axial displacement.

$$\omega = \frac{\pi}{L}\sqrt{\frac{E}{\rho}} \qquad \textit{Equation 46}$$

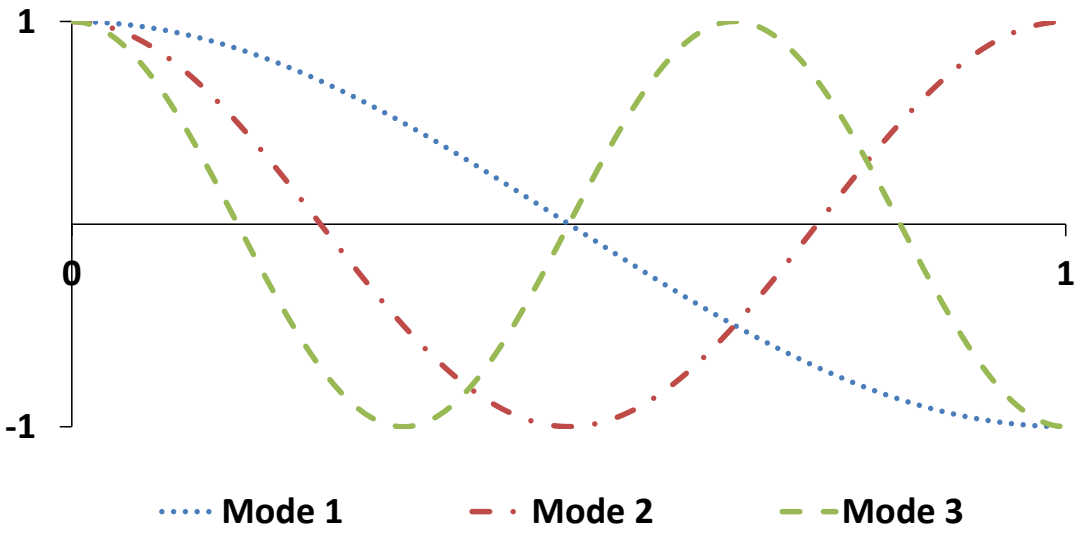

Figure B. 2 : First 3 modes of axial vibration for a freely supported beam

Similarly to *Figure B.1*, the x-axis is normalized beam length while y-axis is the normalized axial displacement in *Figure B.2*. *Table B.2* is the node locations for mode 1, 2, and 3.

Table B. 2: Node Locations of freely supported Axial Beam Vibration

Mode	Number of Nodes	Normalized Node Location
1	1	.500
2	2	.250 .750
3	3	.167 .500 .833

B.3 Torsional Beam Vibration

For the case of the torsional vibration, assume that the torsional stiffness of the beam (K) is expressed as the following equation where G is the Shear Modulus of the beam, J is the polar area moment of inertia for the beam cross-section, and L is the length of the beam.

$$K = \frac{GJ}{L} \qquad \textit{Equation 47}$$

Then assume the external torque acting on the end mass can be summed and rearranged into *Equation 48* where θ is the angular displacement of the mass end and I is polar moment of inertia for the mass end.

$$-K\theta = I(\theta'') \qquad \textit{Equation 48}$$

Equation 48 is the equation of motion for the mass end and must be solved. After assuming that the mass end is under simple harmonic motion, *Equation 49* and *50* can be used to relate torsional natural frequency (ω) to angular displacement of the mass end. The variable A is the amplitude of the torsional vibration and will eventually be cancelled out.

$$\theta(t) = Asin(\omega t) \qquad \textit{Equation 49}$$

$$\theta''(t) = -\omega^2 Asin(\omega t) \qquad \textit{Equation 50}$$

By substituting *Equation 49* and *50* into *Equation 48*, an equation that relates the torsional frequency of the mass end to the Shear Modulus of the beam can be found.

$$\omega = \sqrt{\frac{GJ}{IL}} \qquad \textit{Equation 51}$$